A MAGNETIC RESONANCE IMAGING MULTICOMPARTMENT PERFUSION MODEL: THEORY AND EXPERIMENTAL VERIFICATION

by

Xiangyang Ma

A dissertation submitted to the faculty of
The University of Utah
in partial fulfillment of the requirements for the degree of

Doctor of Philosophy

Department of Medical Informatics

The University of Utah

August 1995

THE UNIVERSITY OF UTAH GRADUATE SCHOOL

SUPERVISORY COMMITTEE APPROVAL

of a dissertation submitted by

Xiangyang Ma

This dissertation has been read by each member of the following supervisory committee and by majority vote has been found to be satisfactory.

Chair: Dennis L. Parker, Ph.D.

Grant T. Gullberg,

Martin P. Schweizer, Ph.D.

James N. Lee, Ph.D.

Homer R. Warner, M.D.

THE UNIVERSITY OF UTAH GRADUATE SCHOOL

FINAL READING APPROVAL

To the Graduate Council of the University of Utah:

I have read the dissertation of [redacted]Ma in its final form and have found that (1) its format, citations, and bibliographic style are consistent and acceptable; (2) its illustrative materials including figures, tables, and charts are in place; and (3) the final manuscript is satisfactory to the supervisory committee and is ready for submission to The Graduate School.

Date

Dennis L. Parker
Chair, Supervisory Committee

Approved for the Major Department

Homer R. Warner
Chair/Dean

Approved for the Graduate Council

Ann W. Hart
Dean of The Graduate School

ABSTRACT

A multicompartment model of MRI signal intensity that is a function of perfusion is developed based upon the assumption that biological tissue can be represented by blood, tissue and immobile water compartments and that excited endogenous protons can be used as a tracer. The principle is analogues to tracer kinetic techniques used in many fields of biological science.

First, the longitudinal magnetization for a two-compartment model, representing blood and tissue, is derived from the modified Bloch equations as a function of the following physiological parameters: blood flow velocity, tissue to blood volume fraction, diffusion, and rate of exchange between the blood and extravascular tissue compartments. Simulations of slice profiles excited by a repetitive sequence of 90° slice-selective pulses show that the signal intensity in the compartments are modulated by these physiological parameters.

Second, the longitudinal and transverse magnetization for both a two-compartment model and a three-compartment model are derived and studied using chromatography column phantoms containing Sephadex gels, which were used to simulate tissue perfusion and the exchange of protons between extravascular and intravascular tissue compartments. Computer simulations were compared in experiments that used two chromatography columns. Slice-selective spin-echo experiments were performed. The results of the experiments agreed with computer simulations, which showed that the MRI signal intensity in the perfused columns is a function of the rate of exchange between extrabead and intrabead compartments. The exchange process modifies the transit time of protons passing through an excited region. Simulations and experiments also showed that both two-compartment and three-compartment models could be used to fit experimental data.

Finally, an experiment was performed on a human brain using arterially tagged endogenous protons as a tracer combined with magnetization transfer techniques to eliminate the immobile water compartment. Our simulations and experimental results show that the accuracy of kinetic parameter estimates will rely on the signal contrast that depends upon the flow velocity of the labeled spins. The arterial spin labeling technique has significant potential to be used for quantitatively measuring tissue perfusion *in vivo* using clinical MRI.

To my parents

whose love and support have made this effort possible

TABLE OF CONTENTS

LIST OF FIGURES

LIST OF TABLES

ACKNOWLEDGEMENTS

I wish to express my sincere appreciation to my advisors, Dr. Grant T. Gullberg and Dr. Dennis L. Parker, for their full support, continuous encouragement, invaluable guidance, and help through the present research. Without their support, encouragement, guidance, and help, it would have been impossible to carry out this work.

My appreciation also goes to the other members of my supervisory committee, Dr. Martin P. Schweizer, for his help in the experiments, Dr. James N. Lee, for his discussion and advice on image programing, and Dr. Homer R. Warner, for his help in providing the necessary knowledge of physiology.

My gratitude is also expressed to Dr. Pengpeng Zhu Tang for valuable discussion and assistance with using the magnetization transfer technique and Dr. Sophia C. Symko for helping with preparation of Sephadex gel phantoms.

To my parents and my daughter, I express my deepest thanks for their love, patience, and constant support during the past years.

CHAPTER 1

INTRODUCTION

Measurement of *in vivo* tissue perfusion is of the greatest clinical interests since it can provide important information about organ viability and function.[1-5] For example, the knowledge of vascular perfusion is useful for cancer therapy[1] and the information about gas exchange[2] can help with the application of respiratory care[3] on regulation of ventilation. To understand how the perfusion relates to release of neuroactive substances is certainly the important step before people are able to predict the way of functioning for human brain.[4] The design and manufacture of artificial organs also require people to understand tissue perfusion in those organs.[5] Unfortunately, assessment of organ tissue perfusion is still an extremely difficult task and its assessment has important health care implications. For example, vascular disease accounts for the highest number of deaths in the Western Hemisphere partly due to inadequate methods to measure vascular perfusion.

A number of techniques have been developed to measure tissue perfusion *in vivo* and *in vitro*. Traditionally, wash-in or wash-out kinetics of exogenously administered tracers have been used to measure flow.[6] With diffusible tracers, this type of measurement yields tissue perfusion rates. In kinetic approaches, serial measurements of tissue tracer levels are made during wash-in or wash-out. With a knowledge of the tracer input function, blood flow or perfusion and kinetic rates can be calculated.[7,8] These least invasive techniques have been adapted to modern imaging modalities by use of the appropriate tracers. For example, ^{18}F and $H_2{}^{15}O$ tracers have been used in conjunction with positron emission tomography (PET),[7] ^{133}Xe washout has been used with SPECT, stable xenon has been used with x-ray CT,[8] and ^{2}H, ^{19}F and gadolinium-DPTA tracers

have been used in conjunction with magnetic resonance to measure regional perfusion in the brain.[9,10] Tissue perfusion may also be measured using a constant tracer inflow to obtain steady state condition. This approach has been used in PET measurements of cerebral perfusion using ^{15}O-CO_2 and $H_2{}^{15}O$.[11,12] However, nuclear medicine methods have a relatively low spatial resolution and require the injection of radioactive material. Even with PET imaging, which presently provides the highest spatial resolution in nuclear medicine perfusion studies, resolution is of the order of 0.5 cm. Since it is the end organ perfusion that determines proper organ perfusion, there is a need for high resolution perfusion imaging, particularly in the brain and heart.

Early on it was recognized that NMR is sensitive to directed and diffusive motion. In MRI, the flow and motion sensitivity can be used to image blood vessels and obviates the need for intravascular contrast agents to delineate the cardiac cavities and vascular structures. It was postulated that MR signal may be reduced by flow in vascular structures with diameters smaller than that the size of a voxel. This postulate was used to explain *in vivo* MR signal intensity variations in the lungs in normal individuals.[13] A theoretical analysis of perfusion and diffusion effects in MR was performed by Taylor and Bushell.[14] Phantom studies of perfusion by Budinger *et al.*[15] and phantom and *in vivo* studies by Le Bihan *et al.*[16] also demonstrated that diffusion and fractional capillary volume might be measured by MRI because of their effect on signal intensity changes within voxels.

In biological tissues, the motions of protons due to molecular diffusion of water and blood flowing through the capillary microcirculation are quite complex since the nature of motions is incoherent which distinguishes it from the coherent motion of flow in large vessels. Diffusion due to pure random motion of molecules will cause attenuation in amplitude of the MRI signal only and the study of diffusion is much simpler than that for perfusion. However, the study of perfusion using MRI is much more difficult because perfusion depends on the geometry of the capillary structure, blood velocity in the

capillary, and the exchange between blood in the capillaries and surrounding tissues. These parameters usually vary not only voxel by voxel, but also within the voxel.

The capillaries, which allow for exchange of water and solutes between the blood and the tissues, are different in many respects from the larger vessels. Their diameters are approximately 7 μ, well below the likely resolution of any conventional MR imager. Their lengths are on the order of a millimeter and the velocity less than a millimeter per second, implying a transit time of a second or more. However, diffusional exchange across the capillary walls can be of the order of 10 times the flow through the capillary, thus some spins entering one end of the capillary are likely not to exit promptly at the other end. Whereas the flow of blood within a large vessel has a well-defined direction, the flow in tissue containing capillaries is quite random. The capillaries typically make up only a few percent of the tissue volume, resulting in a large background of stationary water. Thus, capillary flow may be difficult to distinguish from diffusion of water within tissues. Finally, flow within tissues is typically patchy and phasic, with significant local time-dependent variations. The net result of all this makes measurement of perfusion a very difficult task.

Due to the significant need for methods to measure perfusion and the potential of MRI to do so, the following is the outline of the objectives of this study: (1) to develop a multicompartment MRI tissue perfusion model that is based on an excitation of endogenous protons, (2) to study and understand the effect of the properties of tissue perfusion upon the MRI signal using computer simulations of our model, (3) to verify our perfusion model experimentally using gel phantoms, and (4) to investigate the arterial spin labeling technique that has significant potential to be used for quantitatively measuring tissue perfusion *in vivo* using clinical MRI.

As mentioned before, because biological tissue is complex, it becomes a difficult task to estimate all potential kinetic parameters. Multicompartment models work well to demonstrate the modulation of the MRI signal due to proton exchange between

compartments. However, the exchange rate constants and volume ratios are embedded in a milieu of several other parameters that affect the NMR signal of biological tissue. Although it is possible in principle to fit the measured signal intensity to these parameters using nonlinear estimation techniques, this still remains a challenging task. To estimate model parameters in practice, it would be useful to utilize methods that isolate parametric effects. For example, magnetization transfer techniques may be useful to obtain the mobile and immobile water exchange. Also, it would be useful when estimating compartment model parameters to remove the coupling between the compartments, which prevents solving the system of differential equations analytically. This might be done by designing a specific pulse sequence.

This dissertation consists of six chapters including this introductory chapter. Chapter 2 gives a concise discussion of the NMR physics and the principles of magnetic resonance imaging. It is shown how to include flow and diffusion into the Bloch equations. Aspects of diffusion imaging are reviewed. In particular, a discussion is given of Le Bihan's IVIM perfusion model that uses pseudodiffusion to describe the incoherent flow in capillary and measures the volume fraction of capillary using a diffusion weighted imaging technique. Finally, kinetic exchange methods are used to model tissue perfusion and a way is proposed for modifying Bloch equations taking into account flow, diffusion, and exchange between compartments.

In Chapter 3 a model of MRI signal intensity that is a function of perfusion is developed based upon the assumption that biological tissue can be represented by a blood and tissue compartment. The longitudinal magnetization is derived from the Bloch equations which are modified to model the magnetization in both the blood and tissue as a function of the following physiological parameters: blood flow velocity, perfusion fraction, diffusion, and rate of exchange between the blood and extravascular tissue compartments. Simulations show that the signal intensity in the blood and tissue compartments are modulated by the physiological parameters. A key factor in the

modulation of the MRI signal by perfusion or exchange is a time-of-flight effect whereby unexcited spins perfuse the excited region and exchange with blood and tissue compartments, thus immediately increasing the slice signal intensity but also delaying the spin exits from the slice, thereby decreasing their contribution to slice signal intensity in future repetitive pulse measurements.

In Chapter 4, based upon the tissue perfusion model developed in Chapter 3, this model was further adapted for chromatography column phantoms containing Sephadex gels, which were used to simulate tissue perfusion and the exchange of protons between extravascular and intravascular tissue compartments. A three-compartment model was constructed including an immobile water compartment. Computer simulations of two-compartment and three-compartment models (which extended the model of Chapter 3 to include transverse magnetization) were compared with experiments that used two chromatography columns. One column contained a Sephadex G-25 gel that had a smaller pore size and a slower rate of exchange between extrabead and intrabead compartments than did a second column, which contained a G-50 gel with a larger pore size. In both columns the beads were of approximately the same size in order to simulate the same ratio of intrabead volume to extrabead volume. Slice-selective spin-echo experiments were performed with the columns oriented parallel to each other in a 1.5 T imager and parallel to the magnetic field, with water flowing through each column perpendicular to the slice at varied mean flow velocities. The results of the experiments showed that the MRI signal intensity in the perfused columns is a function of the rate of exchange between extrabead and intrabead compartments. The simulations also showed that both two-compartment and three-compartment models could be used to fit the experimental data.

In Chapter 5, we present studies of the magnetization transfer effect, a mechanism that causes coupling of differential equations between mobile and immobile water compartments. The effect of magnetization transfer between free water and immobile water in tissue on MRI contrast was studied experimentally using dog kidney tissue. In

experiments the saturation transfer method was applied to saturate spins in the immobile water compartment such that it isolates parameters such as exchange rate constant and apparent relaxation times associated only with the free water not with immobile water and it simplified the model in which only one differential equation corresponding to tissue compartment is considered. We also investigated the potential possibility of using MRI to measure the exchange between extravascular and intravascular compartments of endogenous protons during blood perfusion of biological tissue.

Chapter 6 summarizes the work accomplished in this dissertation and discusses potential future work.

CHAPTER 2

PRINCIPLES OF NMR AND MR IMAGING

2.1 Physics of NMR

2.1.1 Nuclear Magnetic Resonance

Nuclear magnetic resonance (NMR) is a phenomenon found in magnetic systems that possess both magnetic moments and angular momentum. In particular, a system such as a nucleus consists of many particles coupled together so that in any given state, the nucleus possesses a total magnetic moment μ and a total angular momentum J or spin. If the nucleus is placed in a magnetic field, through interactions with the magnetic field, both the total magnetic moment and the total angular momentum eventually will line up their axis with the applied field, so that we can write

$$\mu = \gamma J \tag{2.1}$$

where γ is the gyromagnetic ratio. For different types of nuclei we should find that the value of γ would vary, for example, $\gamma = 42.58$ for H^1 and $\gamma = 10.71$ MHz/Tesla for ^{13}C.

From quantum mechanics it is known that

$$\mu_z = \gamma J_z = \gamma \frac{h}{2\pi} I_z, \tag{2.2}$$

where I_z is the component of spin operator along the z-direction that can have values of $-1/2$ and $1/2$ for proton, and h is Plank's constant.

The application of a magnetic field B_0 produces an interaction energy of the nucleus of amount

$$E = -\mu \cdot B_0 . \tag{2.3}$$

Taking the field to be along the z-direction, thus

$$E = -\gamma \frac{h}{2\pi} B_0 I_z . \tag{2.4}$$

Since proton only have two energy states corresponding to when $I_z = -\frac{1}{2}$, or $\frac{1}{2}$, the energy difference between these two states is

$$\Delta E = \frac{\gamma h B_0}{2\pi} . \tag{2.5}$$

Usually spins tend to stay at the lower energy state. If an alternating field is applied and spins transit from the lower to the higher energy state, the energy absorbed by each spin has to be equal to the value at right side of Eq. (2.5). This condition is called resonance condition. When resonance condition is met spins will be excited and one should be able to detect the presence of such a set of energy levels by some form of spectral absorption when spins transit from the higher back to the lower energy level. The energy of the electromagnetic radiation resulting from the transition between different energy levels is dependent of such an angular frequency ω that

$$\Delta E = \frac{h}{2\pi} \omega . \tag{2.6}$$

Considering Eqs. (2.5) and (2.6) are equal to each other under resonance condition, we find

$$\omega_0 = \gamma B_0 , \tag{2.7}$$

where ω_0 is called Larmor frequency. It is interesting to see that Plank's constant disappeared in Eq. (2.7), which gives us a hint that we might be able to use the classical

picture to observe the dynamical behavior of magnetic resonance. As we know now, the above hypothesis is valid. Therefore, we will use the classical treatment from now on to describe NMR.

2.1.2 Bloch Equations

2.1.2.1 Equation of Motion

We begin our study with a classical description of the motion of a spin in an external magnetic field B, assuming the B may vary with time. A torque on the magnetic moment μ will be produced by B as $\mu \times B$. The equation of motion of a spin can be established by equating the rate of change of angular momentum J with the torque (in vector form) as

$$\frac{dJ}{dt} = \mu \times B. \tag{2.8}$$

Since $\mu = \gamma J$, we yield

$$\frac{d\mu}{dt} = \gamma\mu \times B. \tag{2.9}$$

Summing the spins over an unit volume,

$$\sum \frac{d\mu}{dt} = \sum \gamma\mu \times B, \tag{2.10}$$

we obtain

$$\frac{dM}{dt} = \gamma M \times B, \tag{2.11}$$

where M is the nuclear magnetization.

2.1.2.2 Magnetization Relaxation Times

When resonance condition is satisfied the absorption of the energy by the samples of protons is completed almost instantaneously. Whereas the loss of the energy or relaxation, as it is named, is not spontaneous. It occurs only when it is stimulated by local magnetic fields that have Larmor frequency components. Local magnetic fields produce these fields with Larmor frequency components within the molecules themselves, and they are modulated by molecular motion and structure. There are two types of nuclear relaxation that must be considered in NMR; both relaxations are thought of as first-order or exponential decay processes.

Spin-Lattice Relaxation (T_1): The first relaxation process is the loss of the excess energy resulting from the pulse to the surroundings (lattice) as thermal energy. This relaxation is called spin-spin relaxation and the time constant is called T_1. If a 90° pulse was applied to a system of spins at their equilibrium state M_0, all spins will be flipped into transverse plane such that the longitudinal magnetization is zero. After the pulse the longitudinal magnetization will increase until it reach to M_0. The time constant T_1 describes the rate of return of M_z magnetization, which as a function of time is $M_z = M_0\left(1 - e^{-t/T_1}\right)$.

Spin-Spin Relaxation (T_2): The second relaxation process is called the spin-spin relaxation or T_2 relaxation, which can also be used to produce NMR signal contrast. Assuming that all the protons are in phase following a 90° pulse, i.e., their spin vectors are parallel with each other in transverse plane. As time goes by, they interact with each other in such a way that they gradually get out of phase. In the process of protons getting out of phase, the net magnetization in the transverse plane decays by $\exp(-t/T_2)$. This process differs from the T_1 relaxation, where the return to equilibrium of the longitudinal magnetization is an energy effect. On the other hand, T_2 describes the loss of phase coherence of the transverse components of spins induced by the excitation pulse. Since only the phase-coherent part of the transverse magnetization can produce a signal, the

value of T_2 actually determines the decay of the detectable signal following a pulse. For water protons it is always true that $T_2 < T_1$.

Adding the relaxation terms into Eq. (2.11) the Bloch equation (in vector form) becomes

$$\frac{dM}{dt} = \gamma M \times B - \frac{M_x i + M_y j}{T_2} - \frac{(M_z - M_0)\, k}{T_1}. \tag{2.12}$$

2.1.2.3 Rotating Reference Frame

In the derivation of Eq. (2.12) we have used a stationary (laboratory) coordinate system to describe the motion of magnetization. It is actually more convenient to use a rotational coordinate system to view the behavior of spins. It can be easy to show that the relationship between the first-order derivative of magnetization $M(t)$ with respect to time in the laboratory frame and that in a frame, rotating about the z-axis with an angular velocity $\vec{\omega} = \omega k$, is

$$\left(\frac{dM}{dt}\right)_{\text{lab}} = \left(\frac{\partial M}{\partial t}\right)_{\text{rot}} + \omega \times M. \tag{2.13}$$

Substituting Eq. (2.12) into Eq. (2.13), we have

$$\frac{\partial M}{\partial t} = \gamma M \times B_{\text{eff}} - \frac{M_x i' + M_y j'}{T_2} - \frac{(M_z - M_0)\, k'}{T_1}, \tag{2.14}$$

where $B_{\text{eff}} = B + \frac{\vec{\omega}}{\gamma}$ is the effective magnetic field viewed from the rotating frame. Also, the primes over the unit vectors indicate the unit vectors for rotating frame. As expected, if the $B = B_0 k$ in laboratory frame, and the angular velocity of the rotating frame is chosen as $\vec{\omega} = -\gamma B_0 k = \omega_0 k$ the magnetization $M(r, t)$ will no longer rotates about z-axis. From now on Bloch equations used through entire studies will always be in the rotating frame with the angular velocity equals to Larmor frequency. Also, for simplicity, ordinary

derivative of magnetization will be used instead of partial derivative of it.

2.1.3 The RF Excitation

In order to receive the NMR signals an alternating field has to be employed. This is accomplished by the radiofrequency (RF) field H_1, which usually is chosen to be along the x axis in the rotating frame. It would be helpful to understand the effect of the alternating field used in Eq. (2.14). Assuming the time duration for applying the alternating field is very short we can reasonably neglect relaxations. Since H_1 is pointing to x axis the motion of the magnetization would be a rotation about x axis at angular frequency γH_1. If the magnetization initially is in equilibrium along z axis it will remain as a constant rotating in yz plane. The angle for magnetization rotating during the time of applying H_1 is called flip angle. It equals $\gamma H_1 T$ when H_1 is a constant and the duration of an RF pulse is T. When H_1 varied with time the flip angle is

$$\theta = \int_0^T \gamma H_1(t)\, dt. \tag{2.15}$$

Suppose the flip angle is $90°$, we expect to see magnetization relaxing after the RF pulse. The relaxation of magnetization in transverse plane produces NMR signal as a function of time

$$S \propto M_0 e^{-t/T_2^*}, \tag{2.16}$$

where T_2^* is effective transverse relaxation time. T_2^* usually is smaller than T_2 due to the field inhomogeneity. This NMR signal is called free induction decay or FID signal.

2.2 Principles of Magnetic Resonance Imaging

2.2.1 Magnetic Field Gradients

The MR image is reconstructed from MRI signals that carry spatial information of the imaged object. For encoding spatial information a static magnetic field has to be made

to vary in space. The uniform magnetic field gradients are commonly used to achieve this goal. In this case, the main magnetic field consists of two parts as

$$B = (B_0 + G \cdot r)\, k, \tag{2.17}$$

where G is a linear field gradient vector, and r is a spatial position vector. The components of G: G_x, G_y, and G_z are constants. At any position, field gradients will produce a Larmor frequency difference by $\Delta\omega(r) = -\gamma(G \cdot r)$. Therefore, the spatial position of a spin determines the precessing frequency. The frequency distribution falls symmetrically about the Larmor frequency $\omega_0 = \gamma B_0$ that corresponds to the precession frequency of the spin at the origin of the spatial coordinate frame.

2.2.2 Two-Dimensional Fourier Transform (2DFT) Imaging

There are several ways for MR imaging reconstruction depending upon how the signal was generated. The most commonly used one for two-dimensional (2D) imaging is called 2D Fourier Transform or spin warp technique. Fig. 2.1 shows a typical pulse sequence for 2D imaging using Fourier transformation for image reconstruction. Without showing the detail of derivation the imaging equation is given by

$$S(k_x, k_y) = \int M_0^+(x, y, z_0, \mathrm{TE})\, e^{-2\pi i (xk_x + yk_y)}\, dxdy, \tag{2.18}$$

in which we have defined $M^+ = M_x i + M_y j$ to denote the transverse magnetization, and

$$k_x = \frac{\gamma}{\pi}\int_0^{T_x} G_x(t')\, dt', \tag{2.19}$$

$$k_y = \frac{\gamma}{\pi}\int_0^{Ty} G_y(t')\, dt'. \tag{2.20}$$

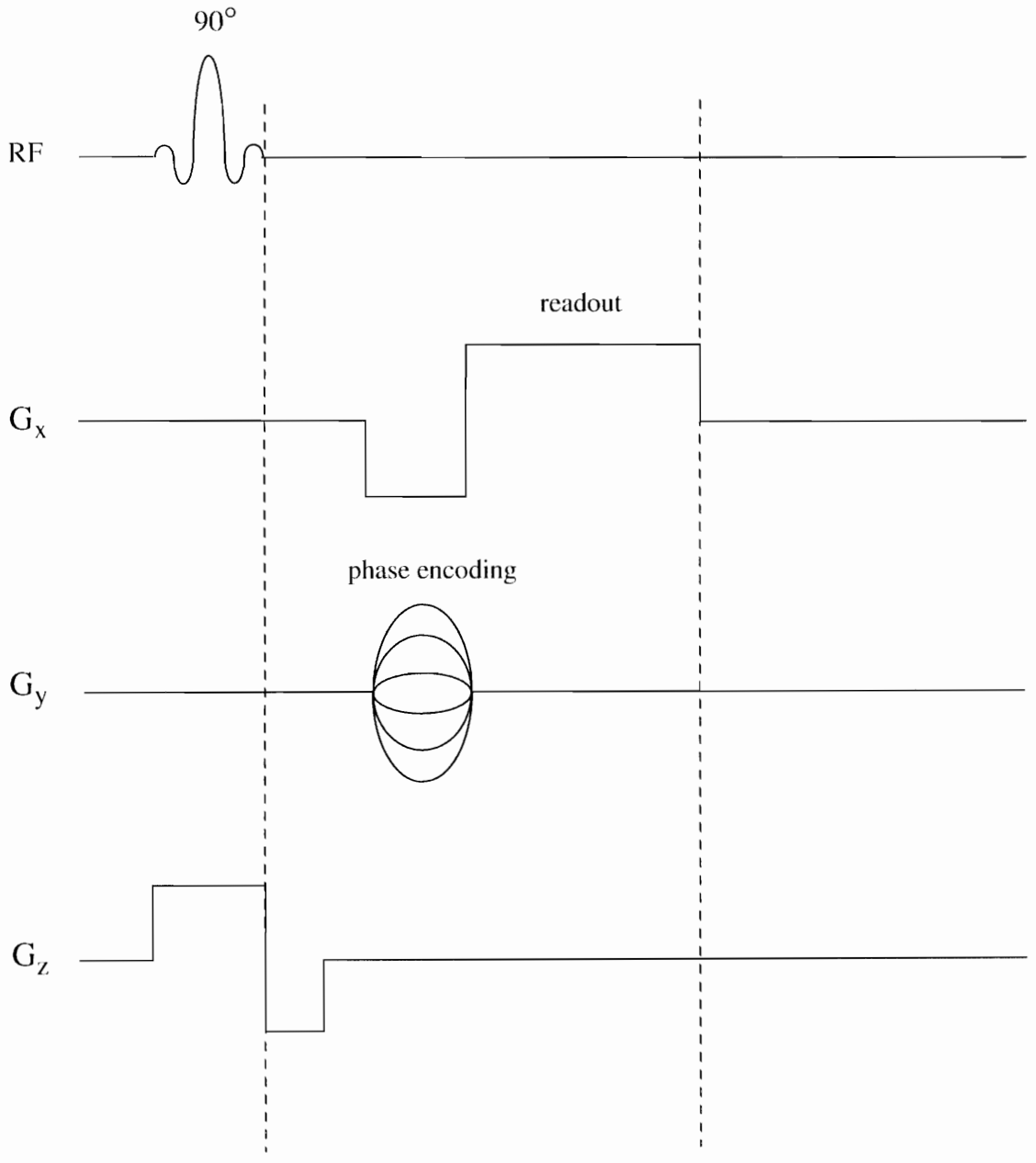

Fig. 2.1 A 2DFT pulse sequence.

It is quite obvious that the image in spatial space can be obtained as the inverse Fourier transform of the measured signal in k-space.

$$M_0^+(x, y, z_0, \mathrm{TE}) = \int S(k_x, k_y)\, e^{-2\pi i (xk_x + yk_y)}\, dk_x dk_y . \qquad (2.21)$$

2.2.2.1 The Slice Selection

A 2D MR image reflects the properties (M_0, T_1, and T_2) of object from a slice. RF pulse is then designed in away such that only the spins within the slice are excited. This is accomplished by applying a RF pulse in combination with a gradient pulse along the direction perpendicular to the imaging slicexy. The most commonly used RF pulse has a sinc function shape to achieve a rectangular spectrum in the frequency domain. During the time when a sinc RF pulse is on, a gradient pulse with an amplitude of G_z is also turned on that causes a precession frequency distribution symmetrically about the isocenter of the slice. The narrow bandwidth of the RF pulse makes sure that only those spins with the precession frequency within the bandwidth region satisfy the resonance condition and then can be excited. The slice thickness are determined by the bandwidth of the RF pulse as well as the amplitude of the slice selection gradient. Since the slice selection gradient can cause spins dephasing across the slice a rephasing gradient is required to avoid a signal loss.

2.2.2.2 Gradients Encoding and k-space Mapping

The spatial encoding of the image plane is achieved by frequency encoding and phase encoding. The frequency encoding is usually defined as the x direction, and a readout gradient G_x is turned on during the signal acquisition. The phase encoding provides the spatial information along the other (y) direction. Before the signal acquisition, a gradient G_y is turned on for a period of time T_y. For an image with a size of $N_x \times N_y$, the pulse sequence should be performed repeatedly for N_y times. Every time the amplitude of G_y will change by an equal increment.

k-space is a useful tool that is established as a 2D plane with the axies, k_x and k_y, normal to each other. Based upon the image equation showed in Eq. (2.18) and the pulse waveform in Fig. 2.1, the signals for each scan with a given phase encoding drawing one line in k-space. A complete scans map an area in k-space.

2.2.2.3 A Spin Echo Pulse Sequence

It has been known that spin dephasing arises from the interactions of magnetic moments with the magnetic fields produced by a variety of sources. However, besides the dipole-dipole interaction that causes T_1, T_2 relaxations, the others including the inhomogeneity of the field and chemical shift are reversible. Considering a situation when transverse magnetization dephases for a period of τ, spin inversion occurs. After the second period of τ spins should be in phase again. This phenomenon is referred to as a "spin echo."

Fig. 2.2 shows a 2DFT spin echo imaging pulse sequence. It consists of a 90° pulse followed by a 180° pulse. The 180° pulse is applied at a time τ after the initial 90° pulse. This 180° pulse is responsible for spin inversion in the transverse plane. At a time of 2τ, also called echo time TE, signal is acquired. The advantage of the spin echo pulse sequence is that transverse signal at echo time is determined by T_2 decay, instead of T_2^* decay.

2.3 Flow Imaging and Time-of-Flight Effect (TOF)

In most cases, the object to be imaged, such as the biological tissue, is considered as stationary. However, it is not always true, especially when we deal with the blood flow. The effect of flow or motion was actually observed early in studies of MRI. It was explained as being due to either the effects of washout of saturated or excited spins from the region being studied or phase shifts acquired due to motion of excited spins along magnetic field gradients. It was soon proposed to use these effects to measure flow. In this section we will introduce the Bloch equations in consideration of flow and describe one of

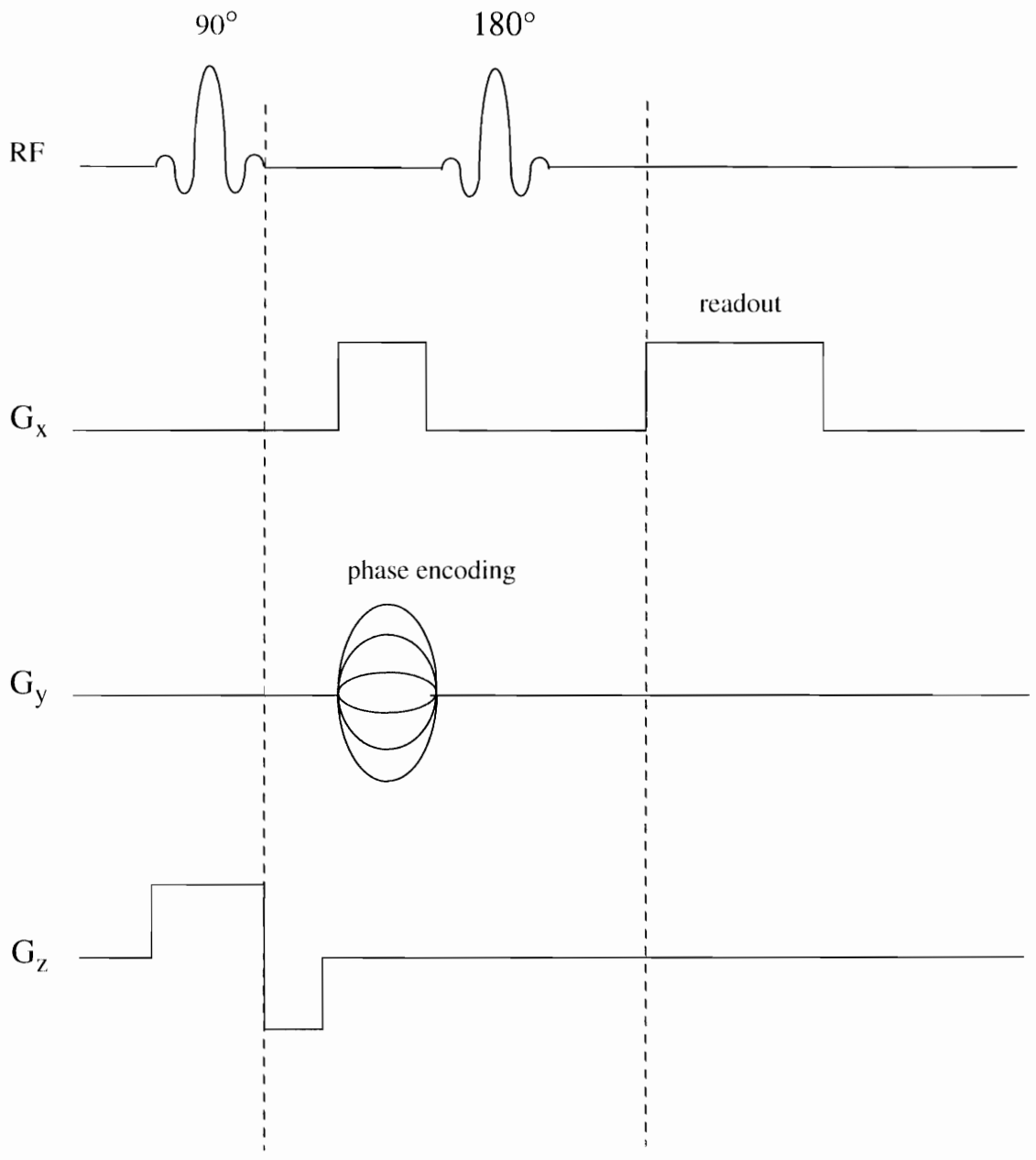

Fig. 2.2 A 2DFT spin echo imaging pulse sequence.

the basic flow effects, i.e., time-of-flight effect (TOF). Although the phase shift effect is also a very important property used in flow imaging techniques we will not discuss it in detail due to its lack of connection with the current study.

When flowing spins are moving with a constant velocity V, the derivative of magnetization M with respect to time t is

$$\frac{dM}{dt} = \frac{\partial M}{\partial t} + \frac{\partial M}{\partial x}\frac{\partial x}{\partial t} + \frac{\partial M}{\partial y}\frac{\partial y}{\partial t} + \frac{\partial M}{\partial z}\frac{\partial z}{\partial t} = \frac{\partial M}{\partial t} + (V \cdot \nabla) M . \tag{2.22}$$

For simplicity, we assume that the flow velocity is along the z-direction. The Bloch equations in a case of no rf field can be rewritten as

$$\frac{\partial M^+}{\partial t} = -i\gamma (G \cdot r) M^+ - \frac{M^+}{T_2} - V\frac{\partial M^+}{\partial z} , \tag{2.23}$$

$$\frac{\partial M_z}{\partial t} = -\frac{M_z - M_0}{T_1} - V\frac{\partial M_z}{\partial z} . \tag{2.24}$$

Solving the Bloch equations one can obtain the solution for the transverse plane:

$$M^+ = M_0^+ e^{-t/T_2} \cdot e^{-i\gamma \int G \cdot (r + Vt)\, dt} . \tag{2.25}$$

It is quite clear that the motion of spins under magnetic field gradients can produce a phase shift that further causes a phase dispersion of spins in the imaging plane such that the MR signal is modulated by flow velocity.

Another factor that can modulate MRI signal in amplitude is called the time-of-flight effect, which is caused by the physical displacement of the spins during successive excitations. When spins are stationary, after several repetitive rf pulses, the magnetization will reach steady-state value depending upon the values of T_1 and TR used for pulse

sequence. If the spins are moving along the slice selective direction some of those saturated spins will move out of the imaging slice during the time between the two adjacent excitations; and at the same time, some unexcited or fresh spins will flow into the imaging slice. This process can enhance the MRI signal in the slice. This phenomenon can be observed in spin echo images.

The TOF method can also be used to modulate a image contrast by using an inversion pulse before the image plane. In this way, the spins flowing into the slice cause a loss of signal in the slice. The MRI signal becomes more saturated compared with that for the stationary spins.

2.4 Diffusion Imaging

Progress in MRI introduced a mapping capability of flow, both macroscopically and microscopically. The former, known as bulk coherent flow, is relatively well known now and has been widely used for various types of flow imaging, such as the angiography by MOTSA.[17] The microscopic incoherent molecular motion, the later type of the flow, has also been studied at the early stages of NMR development by Carr and Purcell.[18] Stejskal and Tanner later developed a spin echo pulse sequence in combination with the incoherent motion sensitive gradients to measure molecular diffusion coefficients.[19]

Diffusional motion of the molecules may be described by the probability $P(r_0|r,t)$ that a particle initially at position r_0 will have moved to position r after a time interval t. In a system a particle freely diffusing, according to Fick's law, may be described by

$$P(r_0|r,t) = (4\pi Dt)^{-3/2}\exp\left(-(r-r_0)^2/4Dt\right), \tag{2.26}$$

where D is the diffusion coefficient. Note that spatially this corresponds to a Gaussain distribution of squared standard deviation $\sigma^2 = 2Dt$, which happens to equal the mean square displacement along any single direction of a particle from its starting point. Using

this distribution one can further obtain the diffusion coefficient as a function of the mean free path length of particles $\bar{l}$, and the mean velocity of a particles $\bar{v}$

$$D = \bar{l} \cdot \bar{v}/6 . \tag{2.27}$$

Now let us consider the equation of motion for magnetization of water protons. Assume that we take a cubic volume of water sample, hence the net change of magnetization with respect to time is

$$\frac{dM}{dt} = -\nabla \cdot F , \tag{2.28}$$

where F is the flux vector which equals to $F = -D\nabla M$. Thus we have

$$\frac{dM}{dt} = D\Delta M . \tag{2.29}$$

Substituting the right side of Eq. (2.29) into the Bloch equations we have a form modified to account for diffusion

$$\frac{\partial M^+}{\partial t} = D\Delta M^+ - \frac{M^+}{T_2} - i\gamma (G \cdot r) M^+ , \tag{2.30}$$

$$\frac{\partial M_z}{\partial t} = D\Delta M_z - \frac{M_z - M_0}{T_1} . \tag{2.31}$$

Apparently, if the concentration of the water protons is the same at any point when gradient is zero, such as the case for bulk water, the diffusion will have no influence on the magnetization. However, if the gradient is not zero, diffusion will result in a signal attenuation in amplitude by a factor R. To solve the above modified Block equations one can find the solution for transverse magnetization is

$$M^{+} = M_0^{+} e^{-t/T_2} \cdot e^{-i\gamma(G \cdot r)t} \cdot R, \tag{2.32}$$

where

$$R = \exp\left(-D\gamma^2 G^2 \frac{t^3}{3}\right). \tag{2.33}$$

It is interesting to see that diffusion affects only the amplitude of the signal, but not the net phase. This is simply because the phase change of any individual proton due to the concentration difference caused by gradient has a symmetrical distribution. Therefore, the phase changes should cancel each other within an entire sample. This makes it much easier for us to measure the diffusion coefficient by designing a pulse sequence with time dependent gradient pulses.

The pulse sequence typically used for diffusion measurement consists of two rf pulses. A 90° pulse begins the experiment; after a time interval τ it is followed by a 180° pulse. A gradient pulse with amplitude g and of duration δ is applied between the two rf pulses. A second identical gradient pulse follows the 180° pulse. The time interval from the end of the first gradient pulse to the beginning of the second gradient pulse is Δ. It has been shown that the signal attenuation due to diffusion for this pulse sequence is[19]

$$R = \exp(-bD), \tag{2.34}$$

where $b = \gamma^2 g^2 \delta^2 (\Delta + 2\delta/3)$.

In a simple diffusion measurement, we acquire the first signal S_0 with $b = b_0 = 0$. The second signal S_1 is obtained with $b = b_1 > 0$. The diffusion coefficient can then be calculated by

$$D = (\ln(S_0/S_1)) / (b_1 - b_0). \tag{2.35}$$

The diffusion we have discussed above is a simple case in which we actually assumed that particles diffuse isotropically. However, a few studies in biological tissue such as in brain have demonstrated that the water molecules are not free to diffuse in all directions. For example, in human brain, the D value of water in myelinated white matter is clearly direction dependent.[16] The origin of the direction-dependent diffusion may be related to the tissue structure in the myelinated white matter, which is characterized by microscopic tracts. In this situation, the water molecules are free to diffuse along the long axial direction of the tracts, but the motion perpendicular to the long axis of the tracts is restricted to some extent for diffusion times relatively greater. Restricted diffusion is very complicated and sometimes needs both special designed pulse sequence and hardware improvements in order to investigate it, and it is beyond the goals of this study. So, in whole studies we will treat the diffusion as isotropic.

2.5 IVIM Model for Perfusion Imaging

In biological tissues, the motions including molecular diffusion of water and microcirculation of blood in the capillary network (perfusion) are quite complex. Unlike the coherent motion of blood flow in big vessels, the nature of motions in tissue is incoherent. In the last section we have shown that diffusion due to pure random motion of molecules will cause attenuation only in the amplitude of the MRI signal. However, to study perfusion using MRI is much more difficult because perfusion will depend on the geometry of the capillary structure, blood velocity in the capillary, and the exchange between blood in the capillaries and tissues surround. Those parameters usually are different not only voxel by voxel, but also within the voxel. Le Bihan developed a simple model to study intravoxel incoherent motion (IVIM) that occurs in each image voxel in MRI.[16] In this IVIM model it was assumed that perfusion has a behavior similar to diffusion such that perfusion can be viewed as a pseudodiffusion.

2.5.1 Pseudodiffusion Model of Microcirculation

Since a voxel consists of a large number of capillaries (5,700 per cubic millimeter in the brain cortex[20]) we can assume blood flow changes capillary segments several times during a given time. Movement of water then can be described by a random walk process, or diffusion. If we can further assume that the capillary network is random arranged, using a statistical approach for Brownian motion, microcirculation modeled by diffusion can then be ascribed by a pseudodiffusion coefficient

$$D^* = \bar{l} \cdot \bar{v}/6, \tag{2.36}$$

where $\bar{l}$ is the mean capillary segment length, $\bar{v}$ is the mean blood velocity in the capillaries. The literature indicates that $\bar{l}$ and $\bar{v}$ are 57 μm and 2.1 mm/sec respectively, in the case of cat brain.[21] It is then expected that a value for D^* can be as high as 2.0×10^{-4} cm^2/sec, which is about 10 times greater than the diffusion coefficient D of water (2.5×10^{-5} cm^2/sec).

In the presence of magnetic field gradients, if a given voxel contains spins moving randomly during the echo time of TE for a spin-echo (SE) sequence, a distribution of phase shifts will be generated symmetrically about the in-phase direction. This loss of phase coherence in the transverse magnetization results only in an attenuation in amplitude F, in addition to that caused by the T_2 relaxation, such that the signal at the time of TE in the voxel is

$$S(TE) = S(0) F \cdot e^{-TE/T_2}. \tag{2.37}$$

If the biologic tissue consists a volume fraction f of water in blood flowing in capillaries the attenuation term F should have two parts: one caused by water diffusion in tissue and the other caused by both water diffusion in blood and the pseudodiffusion because of water moving in capillaries:

$$F = e^{-bD} \cdot \left[(1-f) - fe^{-bD^*} \right], \tag{2.38}$$

where b is the gradient factor that depends only on the set of diffusion gradient pulses used particularly. Substituting Eq. (2.38) into Eq. (2.37), we obtain

$$S(TE) = S(0)\, e^{-TE/T_2} \cdot e^{-bD} \cdot \left[(1-f) - fe^{-bD^*} \right]. \tag{2.39}$$

According to the method described in section 2.4 it is clear that the diffusion coefficient measured using Eq. (2.35) should be the apparent diffusion coefficient that contains the contributions from the diffusion coefficient of water D, the pseudodiffusion coefficient of water moving in capillaries D^*, and the volume fraction f.

Notice that Eq. (2.39) is derived without the consideration of exchanges between blood and tissue. That means the assumption that exchanges between water inside capillaries and outside capillaries can be neglected has to be made.

2.5.2 Separation of Diffusion and Perfusion Using MRI

Three pulse sequences are used to generate diffusion/perfusion imaging. The first one is a standard spin-echo (SE) pulse sequence in which the effect of diffusion/perfusion on signal is negligeable. The second one is a SE pulse sequence, in addition to the regular readout gradients, with a pair of diffusion gradients in the readout direction which is symmetrical about the 180° pulse. The third one is identical to the second one except that the amplitude of the diffusion gradient is greater. The signals from these experiments are denoted as S_0, S_1, and S_2, respectively.

From the last section we know that the apparent diffusion coefficient (ADC) can be measured by MRI signals S_0 and S_1 from two experiments for two different diffusion gradients

$$\text{ADC} = \ln(S_0/S_1) / (b_1 - b_0), \tag{2.40}$$

where b_0 and b_1 are the gradient factors defined in last section corresponding to the first and the second pulse sequence, respectively.

For the first pulse sequence, we usually can neglect standard gradients in the slice selection, phase, and readout directions since their durations are very short such that the signal can be written as

$$S(TE)_0 = S(0)\,e^{-TE/T_2} \quad . \tag{2.41}$$

For the second pulse sequence, suppose the additional pair of diffusion sensitive gradients added along the readout direction are long or strong enough so that $fe^{-bD^*} \ll (1-f)$, we hence neglect the term caused by pseudodiffusion. The signal from the second pulse sequence is then

$$S(TE)_1 = S(0)\,e^{-TE/T_2} \cdot e^{-b_1 D} \cdot (1-f) \; . \tag{2.42}$$

From Eqs. (2.40)-(2.42) ADC can be further expressed as

$$\mathrm{ADC} = D + \ln\left(\frac{1}{1-f}\right)/b_1 \, . \tag{2.43}$$

considering that in most cases $f \ll 1$, we finally obtain

$$\mathrm{ADC} \cong (D + f/b_1) \; . \tag{2.44}$$

Notice that the attenuating term due to pseudodiffusion does not appear in Eq. (2.44), which implies that the capillary geometry is not needed. If the pseudodiffusion treatment on the capillary network is applicable it certainly simplifies the problem in hand.

The signal for the third pulse sequence is similar to Eq. (2.42) except that the b_1 value should be replaced by b_2. Take a logarithm of the ratio of S_1 to S_2 and divided by $b_2 - b_1$, thus obtaining

$$D = \ln (S_1/S_2) / (b_2 - b_1) . \tag{2.45}$$

Substituting Eqs. (2.44) and (2.45) back into Eq. (2.43), we are able to calculate the volume fraction of the capillary blood to tissue by

$$f = 1 - \exp\left[-b_1 \cdot \left(\frac{\ln (S_0/S_1)}{b_1 - b_0} - \frac{\ln (S_1/S_2)}{b_2 - b_1} \right)\right] . \tag{2.46}$$

2.5.3 Phantom Studies and Results

Experiments were performed with a 1.5T GE Signa imager. The slice thickness was 1 cm with Image size of 256x256. The FOV was 24 cm^2. The acquisitions used an SE pulse sequence in combination with a pair of diffusion sensitive gradients symmetrically about the 180° pulse. TR was 1,000 ms and TE was 140 ms. The diffusion gradients were applied on the readout direction. The pulse duration $\delta = 40$ ms with a $\Delta = 28$ ms gap.

Bulk water and bottled acetone were chosen as phantoms. Phantom diffusion weighted images were obtained and the diffusion coefficients computed from the images are listed in Table 2.1. Comparing them with the values from published literatures it was found that diffusion coefficient measurements agree with the results from literature.

2.5.4 Human Studies and Results

The same pulse sequences were used to obtain human brain images. The ADC, D, and f were calculated (Table 2.2). In normal brain, the ADC of grey matter was significantly higher than that of white matter. Comparing the results for ADC with that from Le Bihan's results, ours are 5-10 times smaller. We also calculated the values for D and f whereas Le Bihan did not calculate them. It has been noticed that f has a negative value for both grey matter and white matter and it cannot be right since the capillary volume fraction in biological tissue has to be a positive number.

Table 2.1 Phantom study results. The measurements of diffusion coefficient and flow volume fraction.

Fluid	D ($\times 10^{-9}$ m^2/sec)	D (Literature) ($\times 10^{-9}$ m^2/sec)
Acetone	4.24	4.5-4.8
Water	2.18	2.25-2.51

Table 2.2 Human study results. The measurements of diffusion coefficient, flow volume fraction, and apparent diffusion coefficient (ADC).

Tissue type	D ($\times 10^{-9}$ m^2/sec)	f (%)	ADC
Grey matter	1.7	-8.6	5.4
White matter	0.99	-8.4	1.6

2.5.5 Discussion

The IVIM model is a useful tool for diffusion measurement *in vivo*. However, a high field scanner with higher gradients might be needed to enhance the sensitivity of diffusion and pseudodiffusion for correctly estimating capillary volume fraction. As Le Bihan pointed out[16] the model fails to take into account the exchange of protons between vascular and extravascular compartments. Therefore, the IVIM model cannot be used to measure perfusion rate. We believe that a model taking into account the exchange of protons between vascular and extravascular compartments is necessary to measure perfusion *in vivo* using excited endogenous protons.

2.6 Kinetic Exchange Perfusion Model

The kinetic exchange methods have long been used to measure flow in physiology and nuclear medicine, especially the flow or perfusion across an organ.[44-48] Based upon the discussions in previous sections of this chapter, it is easy to see how to incorporate flow, diffusion, and kinetic exchange into the Bloch equations to develop a perfusion model.

2.6.1 Modified Bloch Equations for Perfusion Model

Consider a tissue system with a flow of blood entering tissue at the exchange rate of K_{in} sec^{-1} and a flow of water protons leaving tissue at the exchange rate of K_{out} sec^{-1}. The transverse and longitudinal magnetization of tissue in a system of modified Bloch equations for flow, diffusion, and the exchanges between tissue and blood can be expressed as a function of time and position

$$\frac{\partial M^+}{\partial t} = D\Delta M^+ - (\nabla \cdot V) M^+ - \frac{M^+}{T_2} - K_{out} M^+ + K_{in} M^+_{blood} - i\gamma (G \cdot r) M^+, \qquad (2.47)$$

$$\frac{\partial M_z}{\partial t} = D\Delta M_z - (\nabla \cdot V) M_z - K_{out} M_z + K_{in} M_{z,\,blood} - \frac{M_z - M_0}{T_1}. \qquad (2.48)$$

In a similar way, we can also write the modified Bloch equations for the blood compartment consisting of exchange terms. The volume differences of the exchange compartments must be considered in the derivation for mass conservation. The details of the derivation can be found in Chapter 3.

2.6.2 Relationship of Exchange Rate and Perfusion

Conventionally, perfusion is measured as a p in ml/g/sec. In the last section, we used an exchange rate K in sec^{-1} to describe perfusion. It will be a logical question to ask what is the relationship between exchange rate and perfusion. In this section, we will derive an equation relating these two parameters.

For simplicity, we consider only the exchange terms in Eq. (2.48) and omit the subscript z in the following discussion. Suppose we have a tissue system with exchange of magnetization between tissue (M) and blood (M_{blood}) compartment. The kinetic equation for tissue magnetization can be written as

$$\frac{dM}{dt} = -K_{\text{out}}M + K_{\text{in}}M_{\text{blood}}. \tag{2.49}$$

If we denote M' as magnetization per gram of tissue and M'_{blood} as magnetization per milliliter of blood, Eq. (2.49) can be rewritten as

$$\frac{d}{dt}M' = -K_{\text{out}}M' + \left(\frac{K_{\text{in}} \cdot 1\ \text{ml}}{1\ \text{g}}\right)M'_{\text{blood}}. \tag{2.50}$$

We now define perfusion as

$$p = \frac{K_{\text{in}} \cdot 1\ \text{ml}}{1\ \text{g}} = \left|K_{\text{in}}\right| \qquad \text{ml/g/sec}, \tag{2.51}$$

thus Eq. (2.51) becomes

$$\frac{d}{dt}M' = -K_{out}M' + pM'_{blood}. \tag{2.52}$$

When water is used as a perfusion tracer a simple assumption that water is freely diffusible is usually made, which means that $M'_{blood} = M'/\lambda$, where λ is the tissue to blood partition coefficient for water defined as (ml of water/g of tissue)/(ml of water/ml of blood). Substituting $M' = \lambda M'_{blood}$ into Eq. (2.52), we have

$$\frac{d}{dt}M' = -K_{out}\lambda M'_{blood} + pM'_{blood}. \tag{2.53}$$

Since the equation equals to zero at equilibrium, finally we obtain the relationship for perfusion and exchange rates at equilibrium as

$$p = K_{out}\lambda = |K_{in}| \qquad \text{ml/g/sec}. \tag{2.54}$$

Also, the relationship for partition coefficient and exchange rates at equilibrium can be found as

$$\lambda = \left|\frac{K_{in}}{K_{out}}\right| \qquad \text{ml/g}. \tag{2.55}$$

CHAPTER 3

AN MRI PERFUSION MODEL INCORPORATING NONEQUILIBRIUM EXCHANGE BETWEEN VASCULAR AND EXTRAVASCULAR COMPARTMENTS

Magnetic Resonance Imaging, Vol. 9, pp. 39-52, 1991.

3.1 Introduction

A significant amount of interest has been shown in using MRI to measure perfusion,[22-33] especially since MRI is able to probe the tissue without using contrast agents or ionizing radiation. Most of the techniques have been based upon models in which the MRI signal amplitude is attenuated through the principle of diffusion. Here we use compartment modeling techniques which have been utilized in other imaging modalities to measure perfusion and that incorporate the effects of exchange between intravascular and extravascular spaces. The modeling approach adds another dimension in terms of measuring perfusion in that it models the modulation of the signal amplitude by time-of-flight effects of flow,[34-36] diffusion, and exchange between vasculature and extravasculature spaces. A model that includes these time-of-flight effects in addition to phase dispersion due to flow and diffusion during gradient application, would be a more appropriate model of tissue perfusion.

Diffusion, on which most of the present perfusion models are based, is a random effect characterized by a pure, incoherent motion, causing the average phase of the transverse magnetization of diffusing spins to be zero and creating a nonrecoverable

attenuation of the signal amplitude in the presence of a gradient. Early on the effect of diffusion on the spin-echo signal was recognized by Hahn,[37] studied in more detail by Carr and Purcell,[18] and then later described mathematically by Torrey[38] who modified the Bloch equations with the addition of diffusion terms. Subsequently, Stejskal and Tanner[19] were able to measure diffusion coefficients in liquids using strong gradient pulses added to a spin-echo sequence. Later the Bloch-Torrey equations were modified by Stejskal[39] to include restricted diffusion which was studied experimentally by him and Tanner.[40] Restricted diffusion was also studied both theoretically and experimentally by Packer[41] for several different pulse sequences. It was later found that restricted diffusion was an important effect in biological tissues, where diffusion coefficients are lower than in pure water, due to the viscosity and restricted diffusion effects attributed to the limitation of water displacement by microscopic obstacles.[42] In all of this work, the attenuation of the spin echo signal for a diffusion process has become a well understood phenomenon.

Some of the early work in diffusion imaging was reported by Taylor and Bushell,[22] Ahn et al.,[25] and Le Bihan et al.[16] In Le Bihan's initial work, he proposed that the in vivo diffusion image is a map of intravoxel incoherent motions (IVIM) where the calculated diffusion coefficient is really an apparent diffusion coefficient (ADC) incorporating the effects of all IVIMs, including molecular diffusion and the seemingly random arrangement of the microcirculation in tissue.[16] Le Bihan et al.[30] later proposed a technique in which two images at two separate diffusion gradient values were obtained in addition to an image obtained using a zero diffusion gradient in order to separate signal attenuation due to molecular diffusion caused by perfused capillaries. Ahn et al.[27] proposed a method for isolating perfusion from diffusion based upon the assumption that the perfusion fraction of the signal attenuation at the first echo signal will give an even echo enhancement. More recent work has built upon Le Bihan's model which more accurately evaluates perfusion by using the technique reported in ref. 25 where the signal attenuation is measured at several gradient amplitudes and diffusion and perfusion values

are determined by least squares fitting to several measurements. However, these methods suffer from long imaging times; thus the images are susceptible to motion effects which dominate the perturbation of the signal. More recent work has developed techniques to obtain diffusion and perfusion data in a shorter imaging time. This has led to the application of steady-state free precision pulse sequences[31,32,43] and echo planar imaging techniques.[33]

Our approach is to develop a compartment model that includes the exchange of protons between blood and extravascular compartments using first order kinetics. The impetus for this is derived from the work in physiology[44,45] and nuclear medicine[46-49] where models are tested using radioactive tracers in an indicator dilution technique. Also, our work has been motivated by the work of Harpen[23] who first proposed the use of protons as an indicator for measuring tissue perfusion with MRI. Our model extends his work to include exchange between blood and extravascular compartments. The differences between tracer studies in nuclear medicine and kinetic studies in MRI using excited protons are that the former deals with scaler observables (counts/sec), and MRI deals with vector observables (longitudinal and transverse magnetization). In addition, NMR relaxation rates are much faster than tracer decay rates.

Compartment modeling is not new to NMR applications but has been used to study biological processes in tissues primarily at the intracellular level.[50] The exchange process between compartments has previously been described and represented mathematically by the Bloch-McConnell equations.[51] The assumptions embodied in these equations are summarized in ref. 32 and several authors have discussed various implications of these assumptions.[52-57] Analytical solutions have been given for Bloch-McConnell equations for the CPMG sequences[58] and for some other sequences with specific conditions,[59] but in many cases have to be solved numerically.[58]

In this paper, the Bloch equations for the perfusion model are developed taking into account the flow, dispersion, and fluid exchange between capillaries and tissue. The

model extends the Bloch-McConnell equations by adding flow and diffusion terms and applies it to an MR imaging application. The equations are solved numerically for the longitudinal magnetization in a volume of tissue which is selectively excited. The longitudinal magnetization is followed as a function of time as excited and nonexcited spins exchange between the blood and tissue compartments. A finite difference technique for solving the system of second order partial differential equations is derived and results from computer simulations are presented. We demonstrate from the simulations that there is amplitude modulation of the signal caused by the time-of-flight effect of flowing, diffusing, and exchanging spins between blood and tissue compartments.

3.2 Perfusion Model

The perfusion model is based upon the use of MRI to excite a slice of tissue shown in Fig. 3.1 and the assumption that perfusion of the tissue modulates the signal detected in the excited slice. The tissue is considered to be a network of capillaries surrounded by a tissue matrix. Blood enters the organ from the arterial side, permeates through the tissue matrix. As it perfuses through the capillary network, the blood diffuses through the capillary endothelium into the tissue consisting of cells and extracellular spaces. The perfused blood in the tissue chamber also diffuses back into the vascular chamber and eventually exits at the venous side.

It is assumed that the blood perfuses the tissue with a flow velocity W parallel to the z axis, and the tissue compartment has flow velocity equal to zero. The exchange of water and/or protons between the intravascular and extravascular spaces is described by the two compartment model shown in Fig. 3.2. Water protons in the blood diffuse into the tissue compartment with a rate constant K_1 and water protons in the tissue reversibly diffuse into the vasculature compartment with a rate constant K_2. The tissue compartment has a diffusion coefficient D representing primarily molecular diffusion; whereas, the capillary network has a diffusion coefficient D^* incorporating the effects of all intravoxel

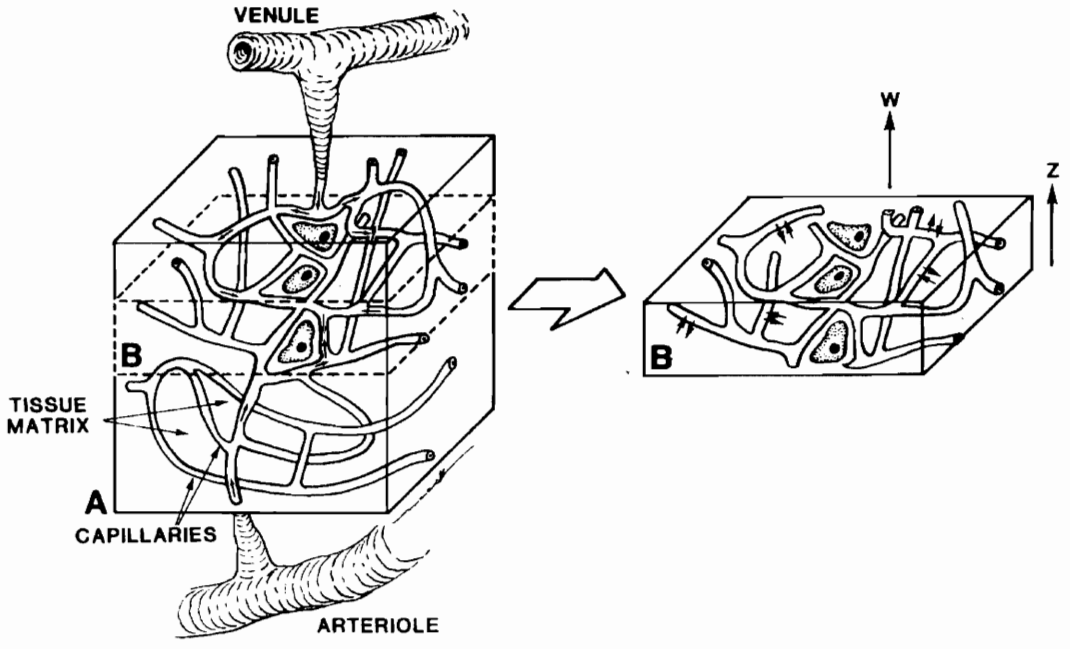

Fig. 3.1 Network of capillaries surrounded by a tissue matrix. Using MRI a slice of tissue B is excited by an rf pulse.

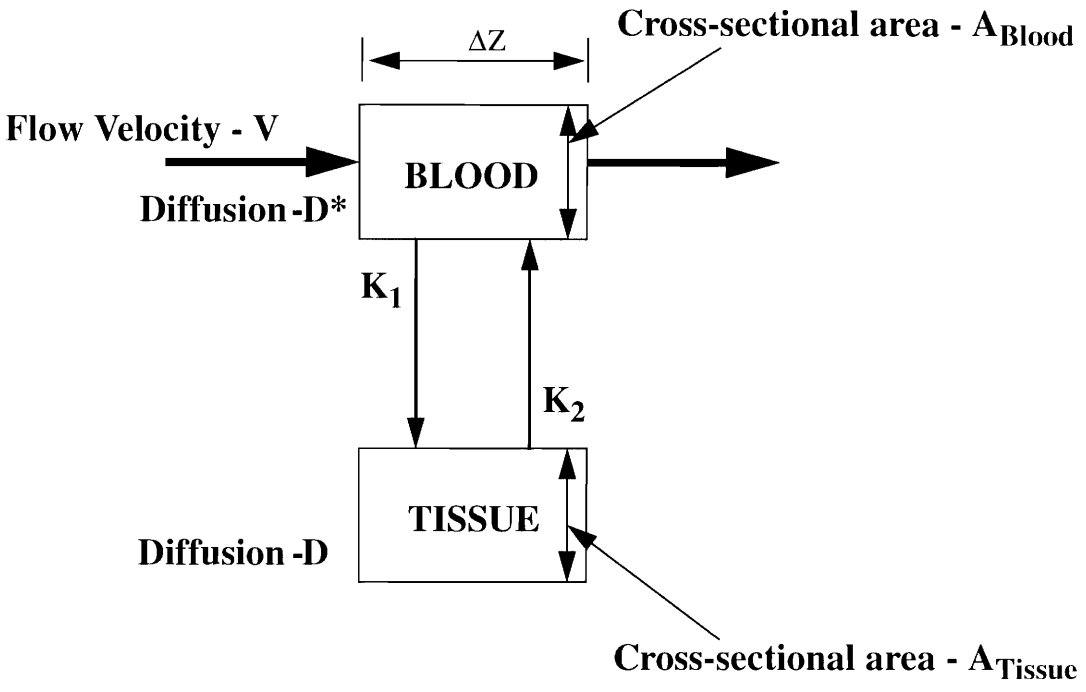

Fig. 3.2 The selected slice in Fig. 3.1 is represented mathematically in Eqs. (3.5) and (3.6) as a two compartment model with exchange rate constants K_1 and K_2. The tissue compartment which includes all extravascular spaces has a cross-sectional area A_t and the blood compartment has a cross-sectional area A_b. The factor β in Eqs. (3.5) and (3.6) is the ratio of these two cross sectional areas: $\beta = A_t/A_b$.

incoherent motions including molecular diffusion and the seemingly random arrangement of the microcirculation in tissue.[16,30]

In using MRI to measure perfusion, excited proton spins are used as the "tagged" material. This means, for example, that the longitudinal magnetization $M_z(z, t)$ in the blood and $m_z(z, t)$ in the tissue are proportional to the concentration of excited spins at the point z and the time t. The excited spins are predominantly water protons which have an equilibrium magnetization M_0 and m_0 in the blood and tissue compartments, respectively. When the tissue section is excited, the changes in the longitudinal magnetization for blood, $M_z(z, t)$, and for tissue, $m_z(z, t)$, are followed as a function of time and as a function of the point z along the slice selection axis. Notice that in MR, the "tagged" material is a vector with longitudinal and transverse magnetization which differs from isotope studies where the "tagged" tracer is a scaler quantity (9). However, in this paper we will study only the variation of the longitudinal magnetization with time.

To develop the Bloch equations which describe the model, let us first consider only the exchange between the extravascular and intravascular compartments; that is, there isn't any flow or dispersion. Also, we will investigate only the longitudinal magnetization. By conservation of matter, we have

$$\frac{\partial M_z}{\partial t} + \beta \frac{\partial m_z}{\partial t} = 0, \tag{3.1}$$

where β is the ratio of the available cross-sectional area of tissue compartment to the available cross-sectional area of blood and is denoted by $\beta = A_t/A_b$. Note, the cross-sectional areas A_t and A_b are orthogonal to z and lie in the slice plane. The rate equation for the extravascular space is

$$\frac{\partial m_z}{\partial t} = \frac{-K'_2\phi}{A_t} m_z + \frac{K'_1\phi}{A_t} M_z, \tag{3.2}$$

where K'_1, K'_2 are the permeability coefficients for flux out of and into the capillary, respectively, and ϕ is the surface area per unit length of the capillary. The parameters K'_1, K'_2 are in units of cm/sec. If we set $K_1 = (K'_1\phi)/A_t$ and $K_2 = (K'_2\phi)/A_t$, we see that the rate constants in and out of the extravascular compartment are in units of per second per tissue cross-sectional area (A_t). Substituting Eq. (3.2) into Eq. (3.1), we can rewrite the system of differential equations for the exchange between the intravascular and extravascular compartments as

$$\frac{\partial M_z}{\partial t} = \beta K_2 m_z - \beta K_1 M_z, \tag{3.3}$$

$$\frac{\partial m_z}{\partial t} = -K_2 m_z + K_1 M_z. \tag{3.4}$$

If we add the system of differential equations in Eqs. (3.3) and (3.4) to the Bloch equations with flow and diffusion terms, we come up with the following two second order partial differential equations:

$$\frac{\partial M_z}{\partial t} = D^* \frac{\partial^2 M_z}{\partial z^2} - W \frac{\partial M_z}{\partial z} - (\beta K_1 + 1/T_1) M_z + \beta K_2 m_z + \frac{M_0}{T_1}, \tag{3.5}$$

$$\frac{\partial m_z}{\partial t} = D \frac{\partial^2 m_z}{\partial z^2} - (K_2 + 1/T_1) m_z + K_1 M_z + \frac{m_0}{T_1}. \tag{3.6}$$

The model described by Eqs. (3.5) and (3.6) and illustrated in Fig. 3.2 is an extension of the Bloch-McConnell equations[50,51] to include flow and diffusion and incorporates the principles of compartmentization on which the concurrent flow models for isotope tracer studies are based.[44,45] Notice that we have assumed that T_1 decay is the same in both vascular and extravascular compartments.

The factor β in Eq. (3.5) differs from the perfusion factor f in Le Bihan's work.[30] The perfusion fraction f is the fractional blood volume of the total volume V_{total}. The parameter β ($\beta = A_t/A_b$) is the ratio of the cross-sectional areas of tissue and blood compartments and is defined so that mass is conserved. If we remember that the total volume is $V_{total} = \Delta z\,(A_t + A_b)$ where Δz is the incremental slice thickness in z, it is easy to derive a relationship between perfusion factor f and the area cross-sectional ratio $\beta : f = 1/(1+\beta)$.

3.3 Finite Difference Scheme

A finite difference scheme is used to solve the system of partial differential equations in Eqs. (3.5) and (3.6). The time and spatial domains are subdivided as shown in Fig. 3.3 by a net of a finite number of mesh points. The time t is the product of the nodal coordinate i and the grid spacing h. The integer i denotes the position of the node along t with $i = 0$ corresponding to $t = 0$. The product jk denotes the location z, where j is the position of the node and k is the grid spacing for z. The variables L and N are used to denote the number of nodes in the time and spatial domains, respectively.

Finite difference expressions are derived using approximations of the partial derivatives. If we consider the differential equation

$$\frac{\partial M_z}{\partial t} = D^* \frac{\partial^2 M_z}{\partial z^2} - W \frac{\partial M_z}{\partial z} - K M_z, \tag{3.7}$$

there are several ways to obtain a finite-difference expression. In our work, the parabolic partial differential equation

$$\frac{\partial M}{\partial t} = D^* \frac{\partial^2 M}{\partial z^2} \tag{3.8}$$

is approximated by the classic explicit approximation[60]

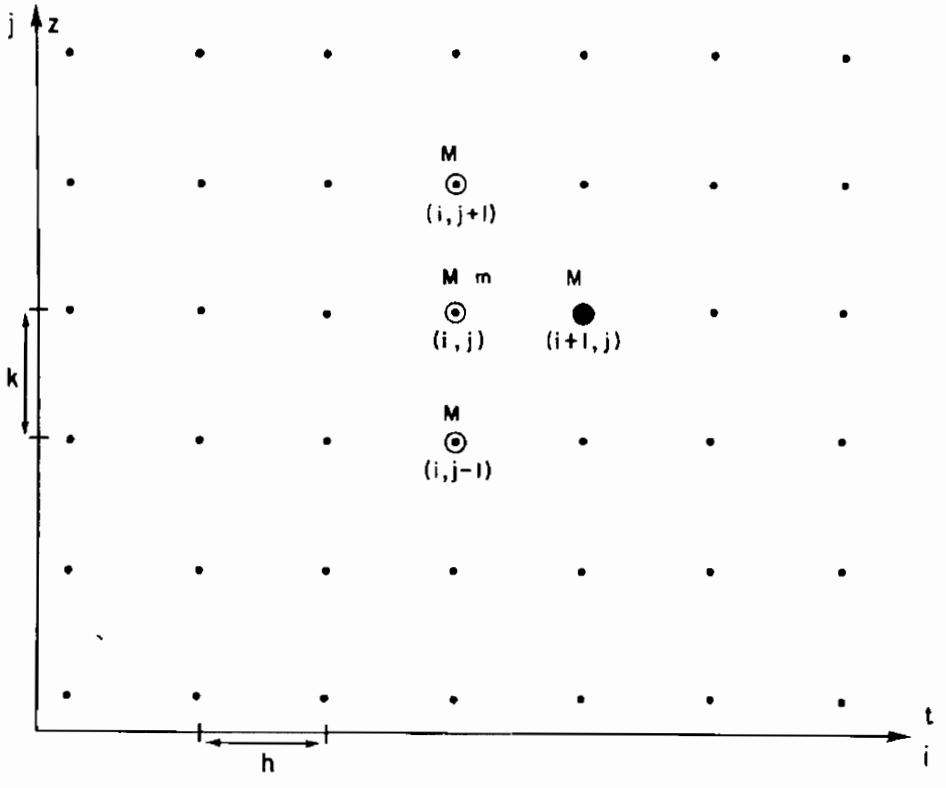

Fig. 3.3 The finite difference scheme in Eqs. (3.13) and (3.14) operates on a grid of mesh points in space and time. For M_z in Eq. (3.13), the value of M_z (= M in figure) at the next time point $(i+1, j)$ is expressed explicitly in terms of M_z at $(i, j+1)$, (i, j), $(i, j-1)$ and m_z (= m in figure) at (i, j). This finite difference scheme is a single-step method.

$$(M_{i+1,j} - M_{i,j}) / h = D^* (M_{i,j+1} - 2M_{i,j} + M_{i,j-1}) / k^2 \tag{3.9}$$

and the partial derivative of M with respect to z is approximated by

$$\frac{\partial M}{\partial z} \approx (M_{i,j+1} - M_{i,j-1}) / (2k) \ . \tag{3.10}$$

Using these approximations, we arrive at the following approximation for the differential equation in Eq. (3.7)

$$\begin{aligned} (M_{i+1,j} - M_{i,j}) / h = \ & D^* (M_{i,j+1} - 2M_{i,j} + M_{i,j-1}) / k^2 \\ & -W (M_{i,j+1} - M_{i,j-1}) / (2k) \\ & -KM_{i,j} \ . \end{aligned} \tag{3.11}$$

Because the approximation for $\partial M_z / \partial z$ is of the same order as for $\partial^2 M_z / \partial z^2$, the approximation remains $O(h^2 + hk^2)$ or $O(h + k^2)$. If, instead, we had used

$$\frac{\partial M}{\partial z} \approx (M_{i,j+1} - M_{i,j-1}) / k \ , \tag{3.12}$$

the result would be less accurate: $O(h^2 + hk)$ or $O(h + k)$.

Substituting the approximations in Eqs. (3.9) and (3.10) into Eqs. (3.5) and (3.6) gives the following system of difference equations:

$$\begin{aligned} M_{z,i+1,j} = \ & h [1/h - 2D^*/k^2 - \beta K_1 - 1/T_1] M_{z,i,j} \\ & + h [D^*/k^2 - W/(2k)] M_{z,i,j+1} \\ & + h [D^*/k^2 + W/(2k)] M_{z,i,j-1} \\ & + h\beta K_2 m_{z,i,j} + hM_0/T_1 \ , \end{aligned} \tag{3.13}$$

$$m_{z,i+1,j} = h[1/h - 2D/k^2 - K_2 - 1/T_1]\, m_{z,i,j}$$
$$+ hD/k^2 m_{z,i,j+1} + hD/k^2 m_{z,i,j-1}$$
$$+ hK_1 M_{z,i,j} + hm_0/T_1 . \qquad (3.14)$$

The symbols $M_{z,i,j}$ and $m_{z,i,j}$ are the longitudinal magnetization at the time $t = ih$ and $z = z_0 + jk$ for the blood and tissue compartments, respectively. Here we assume that z_0 is the initial boundary location for z.

The computation procedure for M_z in Eq. (3.13) is diagrammed in Fig. 3.3. The value of M_z at $(i+1, j)$ is determined by the values of M_z at (i, j), $(i, j+1)$, and $(i, j-1)$ as well as the value of m_z at (i, j). So, the coupling terms [for example, m_z in Eq. (3.13)] in the system of equations are handled by an explicit expression where the current value of each coupling term is used to compute the magnetization at the next time node. The finite difference equations specify a single-step method that uses approximations at one previous time point to determine the value at the next point.

Theoretically, a finite difference approximation should yield exact solutions as the grid sizes h and k approach zero. Because of ringdove errors in the computer, errors are committed as the explicit calculations are carried out. The manner in which these errors are amplified or damped characterizes the stability property of the algorithm. An approximation is said to be stable if the effect of any single fixed roundoff error is bounded. This error is independent of the number of mesh points and can be made arbitrarily small. The method we used is conditionally stable, which means there are restrictive bounds on the grid widths, h and k. Using the methods in ref. 42, one can show that h and k should be chosen so that $Dh/k^2 < \frac{1}{2}$ (D here being the larger of D or D^*).

It is also important to maintain fixed boundary values both in front of and beyond the excited slice. Due to flow the excited magnetization profile could go beyond the preselected computational boundaries. Therefore, the width of the region of computation in z should be chosen sufficiently larger than the slice thickness.

3.4 Computer Simulations

Simulations of slice profiles were performed for the two compartment perfusion model for various values of area cross-sectional ratios β [$\beta = (1-f)/f$ where f is the perfusion fraction defined by Le Bihan et al.[30]] and rate constants K_1 and K_2. From the slice profiles the total slice signal intensity was integrated so as to simulate the signal intensity expected from a slice-selective gradient refocusing pulse sequence. The purpose of the simulations was to evaluate the modulation of the longitudinal magnetization as a function of the physiological parameters: β, K_1, K_2.

The tissue is assumed to be perfused with a flow velocity of $W = 0.8$ cm/sec and a diffusion coefficient $D = 2.5 \times 10^{-5}$ cm^2/sec in tissue and $D^* = 2.0 \times 10^{-4}$ cm^2/sec in blood. D corresponds to a diffusion coefficient of pure water at $40°C$, and D^* is the pseudodiffusion coefficient due to molecular diffusion and the pseudorandom organization of the capillary network.[16,30] It is assumed that the tissue and blood compartments have the same T_1 decay time of 0.5 seconds.

3.4.1 Slice Profile

A 0.5 cm slice of tissue illustrated in Fig. 3.1 was excited with a 90° pulse and slice profiles were calculated numerically using the finite difference equations in Eqs. (3.13) and (3.14). The number of grid points L in time was chosen to be 50,000. This was to cover a time interval corresponding to a TR of 0.5 sec with a grid size h of 1×10^{-5} sec. The grid size k in z was determined from $k = (6h)^{1/2}/8 = 0.0009682$ cm. (Note, this satisfies the requirement that $k > (2D^*h)^{1/2}$.) Simulations were performed on a 2.5 cm width of tissue so that with this grid size there were approximately $N = 2582$ grid points along the spatial coordinate z.

The single-step nature of the algorithm requires initial conditions for M_z and m_z at $t = 0$ or using the index i at $i = 0$. In simulating the excitation of a 0.5 cm slice, we assume the boundary conditions for the blood compartment are

$$M_z(z,t) = M_z(z,0) = \begin{cases} 0 & -0.25 < z < 0.25 \text{ cm} \\ M_0 & otherwise \end{cases}, \tag{3.15}$$

and the boundary conditions for the tissue compartment are

$$m_z(z,t) = m_z(z,0) = \begin{cases} 0 & -0.25 < z < 0.25 \text{ cm} \\ m_0 & otherwise \end{cases}, \tag{3.16}$$

The equilibrium magnetization in the blood compartment was chosen to have a normalized value $M_0 = 1$. The equilibrium magnetization in the tissue compartment m_0 was determined so that at equilibrium $K_1 M_0 = K_2 m_0$.

In addition to the initial conditions, the finite difference equations in Eqs. (3.13) and (3.14) require the boundary values for $M_{z,i,-1}$, $m_{z,i,-1}$ and $M_{z,i,N+1}$, $m_{z,i,N+1}$. The manner in which they are specified may affect the stability characteristics of the algorithm. The approach we used is as follows: $M_{z,i,-1} = M_{z,i,0} = M_0$; $m_{z,i,-1} = m_{z,i,0} = m_0$ and $M_{z,i,N+1} = M_{z,i,N}$; $m_{z,i,N+1} = m_{z,i,N}$ for all $i = 0, 1, 2, \ldots, L$. Substituting these into Eq. (3.13) and (3.14) give the following difference equations for $M_{z,i+1,j}$ and $m_{z,i+1,j}$ when $j = 0$:

$$M_{z,i+1,0} = h[1/h - D^*/k^2 + W/(2k) - \beta K_1] M_0 + h[D^*/k^2 - W/(2k)] M_{z,i,1} + h\beta K_2 m_0, \tag{3.17}$$

$$m_{z,i+1,0} = h[1/h - D/k^2 + K_2] m_0 + hD/k^2 m_{z,i,1} + hK_1 M_0; \tag{3.18}$$

and for $M_{z,i+1,j}$ and $m_{z,i+1,j}$ when $j = N$:

$$M_{z,i+1,N} = h[1/h - D^*/k^2 - W/(2k) - \beta K_1 - 1/T_1] M_{z,i,N} + h[D^*/k^2 + W/(2k)] M_{z,i,N-1}$$

$$+ h\beta K_2 m_{z,i,N} + hM_0/T_1 , \tag{3.19}$$

$$m_{z,\,i+1,\,N} = h\,[\,(1/h) + (D/k^2) + K_2 + 1/T_1\,]\,m_{z,\,i,\,N}$$

$$+ hD/k^2 m_{z,\,i,\,N-1} + hK_1 M_{z,\,i,\,N} + hm_0/T_1 \tag{3.20}$$

Initially, slice profiles were calculated 0.1 seconds after the first, second, third, and tenth pulses of a repetitive 90° pulse with a TR of 0.5 sec. In the simulation the 90° pulse excited a 5 mm slice between -0.25 cm to 0.25 cm. From the results shown in Fig. 3.4, it appears that an equilibrium is reached after three pulses. Therefore, in all the simulations the results were calculated after the third 90° pulse.

Then slice profiles were calculated as a function of time at 0.1, 0.3, and 0.5 seconds after the third 90° pulse and plotted for both the blood and tissue compartments for various physiological parameters β, K_1, K_2. Along the slice coordinate z (Fig. 3.1), three points at z_A = –0.20 cm, z_B = 0.23 cm, and z_C = 0.35 cm were selected to plot the relaxation curves as a function of time.

3.4.2 Total Slice Signal Intensity

The total signal from an excited slice of tissue is the sum of the signal contribution from the blood and tissue compartments and is proportional to the sum of the magnetization concentration in each compartment. The total magnetization concentration as a function of z is

M (magnetization/totoal volume)

$$= \frac{\Delta z A_B}{\Delta z\,(A_B + A_T)} M_z\,(\text{blood magnetization concentration})$$

$$+ \frac{\Delta z A_B}{\Delta z\,(A_B + A_T)} m_z\,(\text{tissue magnetization concentration}) \tag{3.21}$$

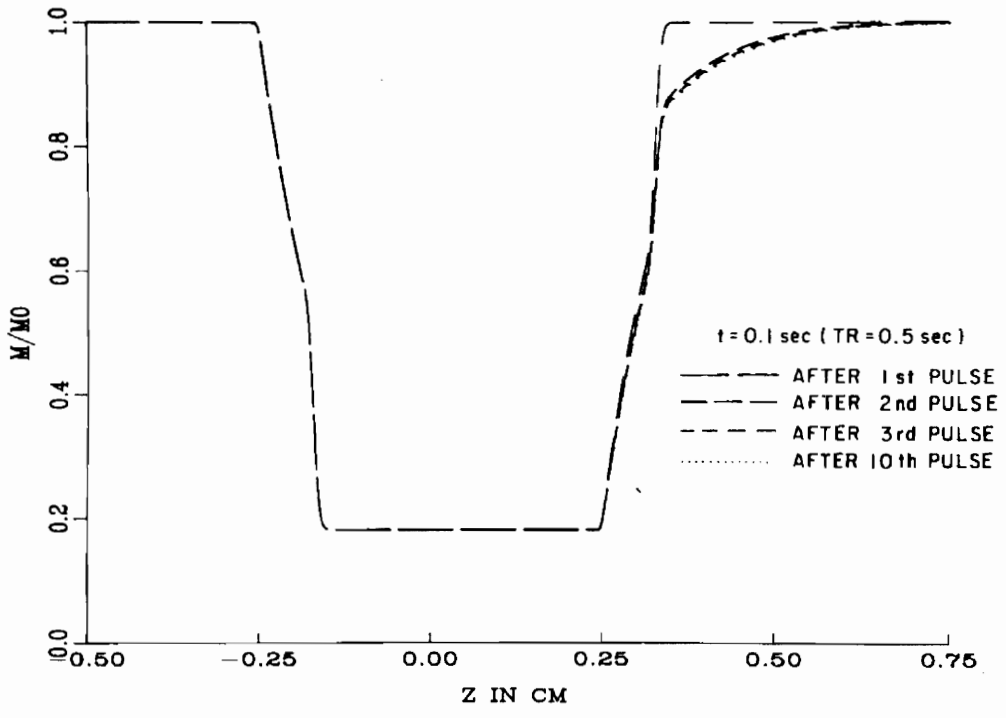

Fig. 3.4 Magnetization profiles for the blood compartment 0.1 seconds after the first, second, third, and tenth pulse. Note that very small differences are seen after the third pulse. The repetition time between the pulses is TR = 0.5 sec ($\beta = 9$; $K_1 = 1.0$; $K_2 = 0.4$ sec^{-1}).

$$= \frac{1}{1+\beta} M_z + \frac{\beta}{1+\beta} m_z . \tag{3.22}$$

The signal for the total slice is obtained by integrating the weighted magnetization in the blood and tissue over the slice coordinate z:

$$S(t) = \frac{1}{1+\beta} \int (M_z + \beta m_z)\, dz . \tag{3.23}$$

In the simulations, the signal in Eq. (3.23) was calculated by numerically integrating the magnetization concentrations at t = 0.5 sec after the third 90° pulse across the selected slice from $z = -0.25$ cm to $z = 0.25$ cm. Since the finite difference method gives values at grid spacing $k = 0.0009682$ cm for z, the integral was calculated by summing over 516 grid points within the 0.5 cm slice.

The total slice signal intensity was calculated numerically (Appendix A) and plotted for various physiological parameters. First, K_2 was fixed at $K_2 = 1.0$ and the signal was plotted as a function of K_1 for $\beta = 0.5, 1.0, 3.0, 5.0, 7.0, 9.0$. For each of the plots the signal was calculated at six K_1 values: 0.4, 0.6, 0.8, 1.0, 1.2, 1.4. Second, K_1 was fixed at $K_1 = 1.0$ and the signal was plotted as a function of K_2 for the same six values as previously plotted for K_1 and for $\beta = 0.5, 1.0, 3.0, 5.0, 7.0, 9.0$. Third, β was fixed at 9.0 and the signal was plotted again as a function of K_1 for K_2=0.4, 0.6, 0.8, 1.0, 1.2, 1.4. Then the third case was redone for a flow velocity $W = 0$.

3.5 Results

3.5.1 Slice Profile

Slice profiles are shown in Figs. 3.5-3.8. Notice that the profiles in the blood do not simply shift to the right as would be expected if flowing spins were the only consideration. Instead, there is dynamic interchange between the blood and tissue of excited and unexcited spins causing the relaxation process to be perturbed in both the blood and tissue compartments.

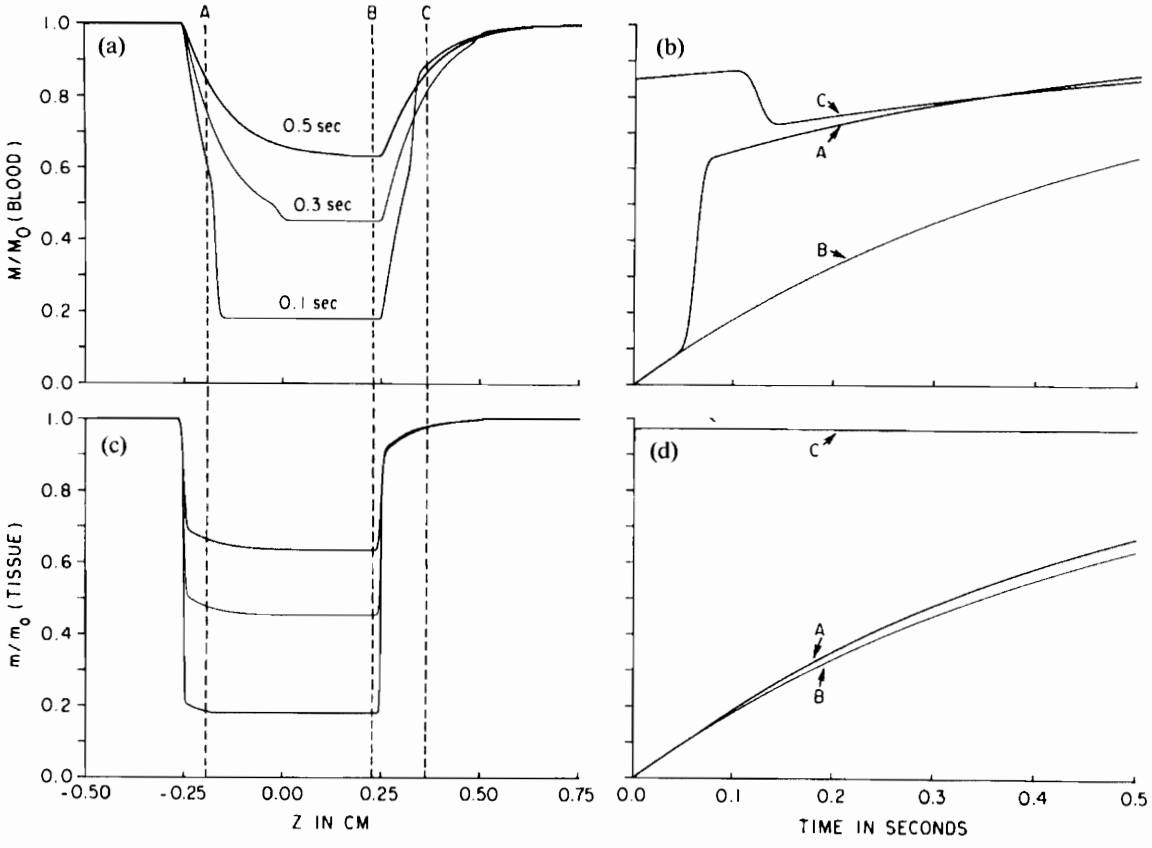

Fig. 3.5 Slice profiles (a) and relaxation curves (b) for the blood compartment, and slice profiles (c) and relaxation curves (d) for the tissue compartment. The plots are obtained from simulations where a 5-mm slice is excited between -0.25 cm to 0.25 cm. Along the slice coordinate z in Fig. 3.1, three points at $z_A = -0.20$ cm, $z_B = 0.23$ cm, and $z_C = 0.35$ cm are selected to plot the relaxation as a function of time in (b) and (d). The flow and diffusion values are $W = 0.8$ cm/sec, $D = 2.5 \times 10^{-5}$ cm^2/sec (tissue), $D = 2.0 \times 10^{-4}$ cm^2/sec (blood). The T_1 decay in the blood and tissue compartments is $T_1 = 0.5$ sec. The ratio of tissue to blood is $\beta = 9$ and the rate constants are $K_1 = 1.0$, $K_2 = 0.4$ sec^{-1} per tissue compartment cross-sectional area.

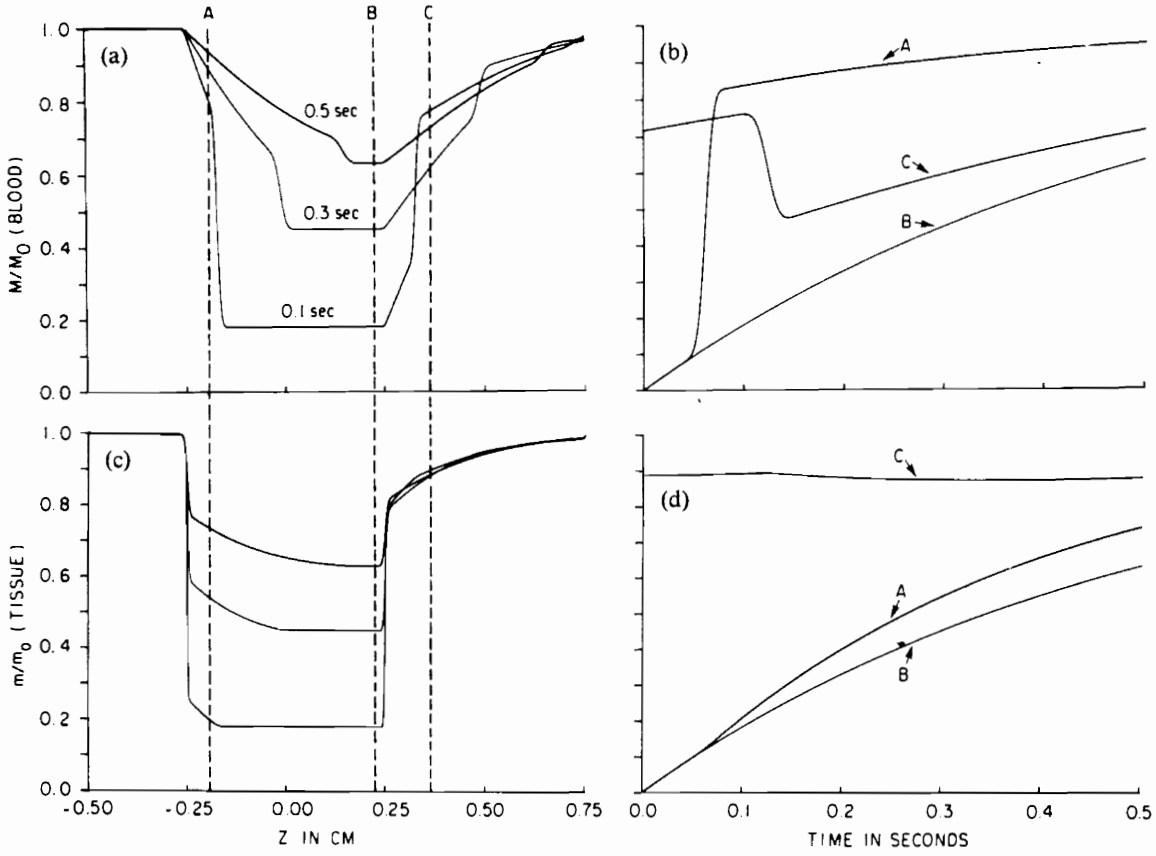

Fig. 3.6 Slice profiles and relaxation curves for blood and tissue compartments where $\beta = 9$, $K_1 = 0.4$, $K_2 = 1.0$ sec^{-1}. All other paprameters are the same as those in Fig. 3.5.

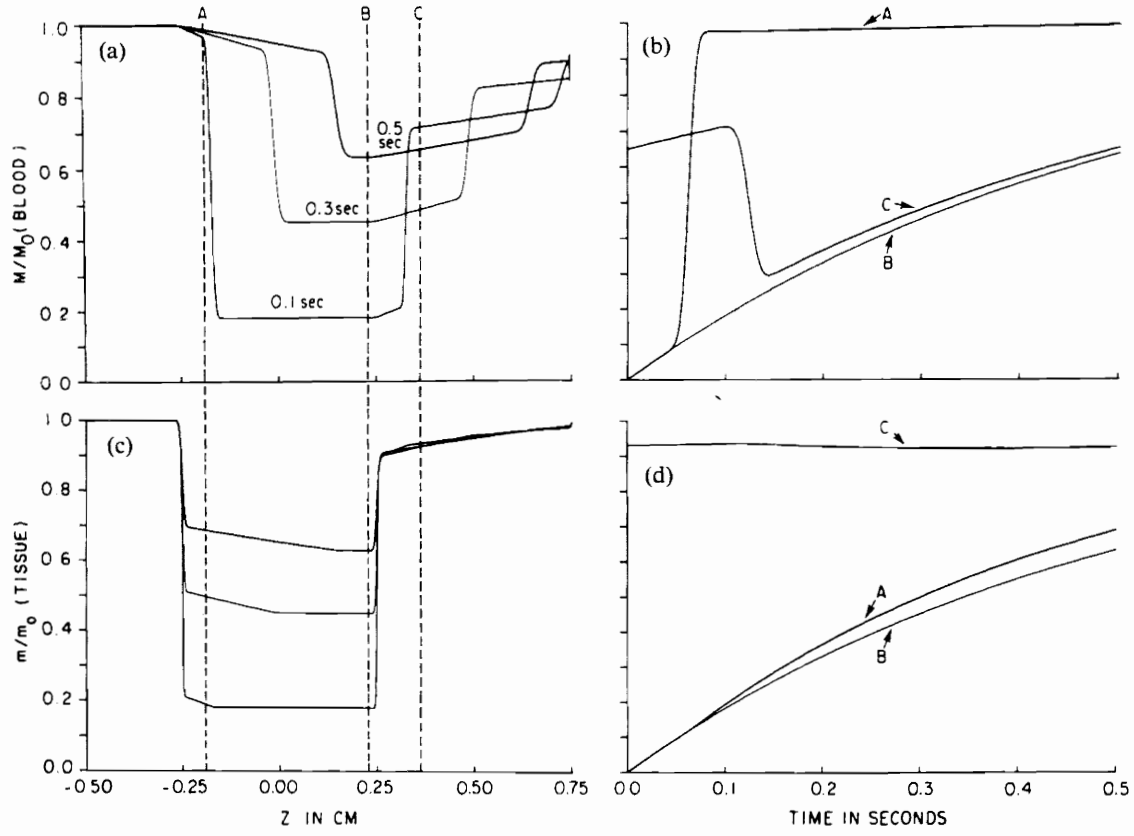

Fig. 3.7 Slice profiles and relaxation curves for blood and tissue compartments where $\beta = 0.5$, $K_1 = 1.0$, $K_2 = 0.4$ sec^{-1}. All other paprameters are the same as those in Fig. 3.5.

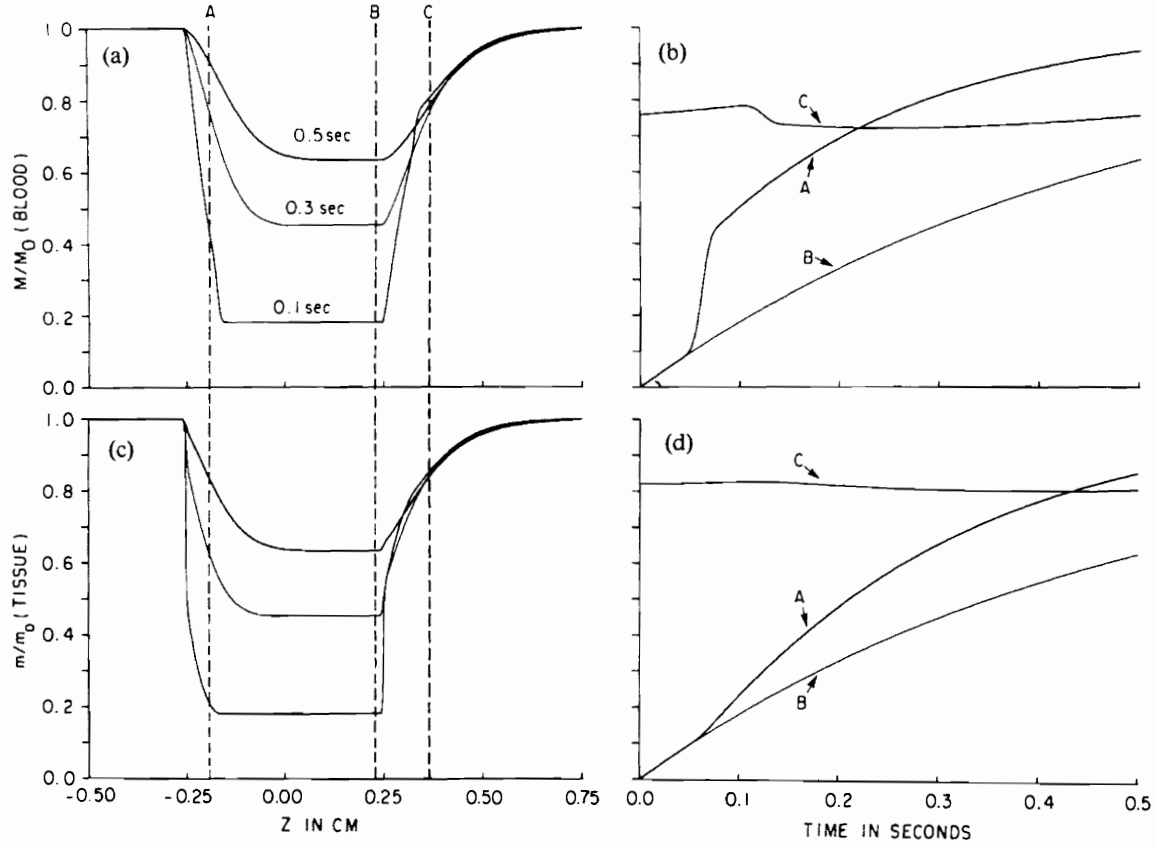

Fig. 3.8 Slice profiles and relaxation curves for blood and tissue compartments where $\beta = 9$, $K_1 = 2.0$, $K_2 = 5.0$ sec^{-1}. All other paprameters are the same as those in Fig. 3.5.

Looking at the profiles, three regions can be identified. In the first region in both the blood and tissue compartments, the magnetization concentration is relaxing faster than T_1 decay due to the increase in concentration of incoming unexcited spins that are at the equilibrium magnetization. However, the relaxation in the blood is not instantaneous as one would expect if no exchange had occurred between blood and tissue. In the central region of the slice, the fresh incoming spins have not penetrated and the spins in the blood and tissue will exchange at a rate that maintains equilibrium between the two compartments. Here the magnetization in the blood and tissue will evolve back to equilibrium at a rate equal to T_1 decay. In the third region, excited spins flow out of the slice. They exchange with tissue causing the excited spins to enter the tissue compartment and unexcited spins to enter the blood compartment at rates that maintain kinetic equilibrium. In this region, the magnetization in both blood and tissue compartments evolves somewhat opposite in direction than that in the first region.

From the figures, we also find that at the edges of the slice profiles and at the transitions between the regions within the slice, the curves are smooth with what appears to be continuous derivatives. This results directly from the effects of diffusion. In simulations with diffusion coefficients of zero, sharp transitions with noncontinuous derivatives were found at each transition region. Since diffusion is a relatively small effect compared to flow, it tends only to smooth the curves at the transition boundaries.

Figure 3.5 shows slice profiles for $\beta = 9, K_1 = 1.0, K_2 = 0.4 \text{ sec}^{-1}$. Assuming that at equilibrium $K_1 M_0 = K_2 m_0$ and $M_0 = 1.0$ in blood, the equilibrium magnetization in the tissue is $m_0 = 2.5$ for this simulation. In the regions at the entrance to and exit from the slice (relative to the direction of flow), the blood profiles in Fig. 3.5(a) show bowing and inflections in the plot between the end points of the region. In these same regions, the tissue curves in Fig. 3.5(c) show a decay slightly faster than normal T_1. This is also exhibited in the plots labeled A and C in Figs. 3.5(b) and 3.5(d). The plots labeled B correspond to samples in the central regions of the profiles and exhibit T_1

relaxation; whereas the plots labeled A and C correspond to samples in the regions at the front and the back of the slice profile and show a decay different from T_1 behavior.

Figure 3.6 shows slice profiles for $\beta = 9$, $K_1 = 0.4$, $K_2 = 1.0$ sec^{-1} with equilibrium magnetization $M_0 = 1.0$ (blood) and $m_0 = 0.4$ (tissue). Here the tissue to blood cross-sectional area is identical to that in Fig. 3.5 but the rate constants are just the reverse, giving an equilibrium magnetization concentration in the tissue more than six times less. This means that as unexcited spins enter the slice through the blood, they will exchange with the tissue at a slower rate than that shown in Fig. 3.5. In comparing the blood curves at the entrance to the slice, the blood curve in Fig. 3.6 appears more rectangular because of slower exchange with the tissue and faster relaxation than that in Fig. 3.5 (Compare plot A in Fig. 3.5(b) and 3.6(b).). Also, even though the rate of exchange between blood and tissue is lower than in Fig. 3.5, the tissue relaxation curve A in Fig. 3.6(d) shows a much larger relative perturbation from normal T_1 decay than is seen in the tissue curves in Fig. 3.5(d). This is because the tissue magnetization concentration is six times less than the tissue concentration in Fig. 3.5, thus giving a relative larger perturbation.

Figure 3.7 shows slice profiles for $\beta = 0.5$, $K_1 = 1.0$, $K_2 = 0.4$ sec^{-1} with equilibrium magnetization $M_0 = 1.0$ (blood) and $m_0 = 2.5$ (tissue). In this example, the rate constants are the same as in Fig. 3.5 but the blood compartment is double the size of the tissue compartment. This causes the incoming spins in the blood pool to be the dominant perturbing effect upon the blood slice profile due to less exchange. In comparing the blood curve in Fig. 3.7(a) to those in Figs. 3.5(a) and 3.6(a), because the incoming spins exchange with a very small tissue compartment, the translated slice profiles appear more rectangular than in previous examples. However, one can still see small changes in the blood curve which are indicative of kinetic exchange. Also, notice that although flow of incoming unexcited spins causes the slice profile in the blood to shift, this does not occur for the tissue curves. Instead, the incoming spins exchange between the blood and

tissue perturbing normal T_1 decay within the regions at the entrance to and the exit from the slice. The tissue curve A in Fig. 3.7(d) shows a relative effect that exhibits a somewhat faster decay than that for the tissue curve A in Fig. 3.5(d), which is due to the smaller tissue compartment. If the rate constants were reversed (i.e., $K_1 = 0.4$ and $K_2 = 1.0$ sec^{-1}), one would observe less of a difference because of a smaller rate of exchange between the blood and tissue compartments.

Finally, in Fig. 3.8, slice profiles are shown for $\beta = 9$, $K_1 = 2.0$, $K_2 = 5.0$ sec^{-1} with equilibrium magnetization $M_0 = 1.0$ (blood) and $m_0 = 0.4$ (tissue). This has the same tissue to blood ratio β as that in Fig. 3.5 but the rate constants are considerably higher. The blood profiles appear to be less rectangular exhibiting more exchange between the unexcited spins flowing into the slice and those in the tissue. In the region at the entrance to the slice, the blood profiles in Fig. 3.8(a) show an almost linear plot between the end points of the region. In this same region, the tissue curves in Fig. 3.8(c) show significant bowing and a significantly faster decay than normal T_1 shown in Fig. 3.5(c).

To summarize the results in Figs. 3.5 -3.8, we see that (1) For fixed K_1 and K_2, large with respect to β corresponds to relatively rapid loss of spins from the blood compartment and buildup of spins in the tissue compartment. For fixed K_1 and K_2, small with respect to β corresponds to relatively rapid build up of spins in the blood compartment and loss of spins in the tissue compartment; (2) For a fixed β, $K_1 < K_2$ results in a relatively rapid buildup of spins in the vascular compartment; likewise, $K_2 < K_1$ results in a relatively rapid buildup of spins in the tissue compartment.

3.5.2 Total Slice Signal Intensity

Figure 3.9 plots the total slice signal intensity (integral of the longitudinal magnetization between -0.25 and 0.25 cm) as a function of K_1 for various tissue to blood volume ratios β. For these simulations, the K_2 was fixed at 1.0. Recall that the time of the integrated signal is at $t = 0.5$ sec after the third 90° pulse which was applied every TR =

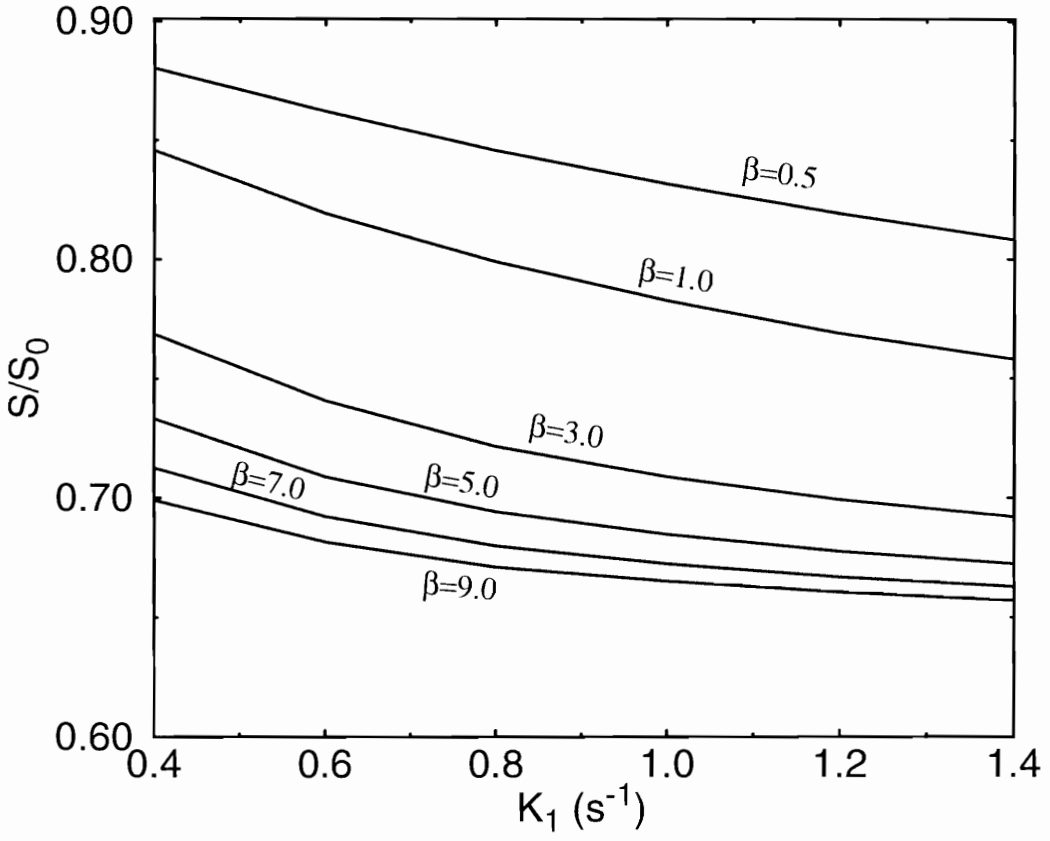

Fig. 3.9 Total signal integrated across the slice [Eq. (3.23)] as a function of K_1 for different cross-sectional area ratio β. K_2 was fixed at 1.0 sec^{-1} and the time of the integrated signal is at t = 0.5 sec after the third 90° pulse which was applied every TR=0.5 sec. All other parameters are the same as those in Fig. 3.5; in particular, the velocity is W = 0.8 cm/sec.

0.5 sec. Notice that, as expected, the signal decreases as K_1 increases. Spins are more likely to be delayed in transit through the slice with increasing K_1 through the exchange process between blood and tissue compartments, thus increasing the saturation with repetitive 90° pulses. Also, notice that the curves decrease in amplitude as the tissue to blood ratio increases. So, as β increases, there is a larger pool to delay spins in transit through the slice. Assuming that at equilibrium $K_1 M_0 = K_2 m_0$, if $M_0 = 1$ and $K_2 = 1$ then $K_1 = m_0$. Thus, the plots are also a function of increasing magnetization concentration in the tissue.

Figure 3.10 plots the total slice signal intensity as a function of K_2 for different cross-sectional area ratios β. Here K_1 is fixed at 1.0 sec^{-1}. All other parameters are the same as those in Fig. 3.9. In contrast to the results in Fig. 3.9, notice that the signal increases as K_2 increases. This is to be expected, as it is more likely that spins will be released from the tissue pool as K_2 increases and allowed to exit the slice more readily. The spins in the slice will be less saturated with increasing K_2, as more unexcited spins replenish the tissue compartment.

Figure 3.11 plots the total slice signal intensity as a function of K_1 for different values of K_2. The tissue to blood cross-sectional area ratio β was fixed at 9.0. All other parameters are the same as those in Figs. 3.9 and 3.10. Notice as in Fig. 3.9, the signal decreases as K_1 increases. The curves reflect that this decrease is a function of K_2; as K_2 increases, the overall amplitude of the curves increase. At higher K_2, the spins are more readily released from the tissue pool so that they can exit the slice through the blood and be replenished by incoming unexcited spins.

The simulations in Fig. 3.11 were redone for all the same parameters except the flow velocity W was set at zero. The results in Fig. 3.12 show a flat curve with plots for different K_2 values superimposed on each other. The results indicate that only perfused tissue can modulate the MRI signal. These simulations also verified the accuracy of the numerical methods Eqs. (3.13) and (3.14) used in solving the Bloch equations.

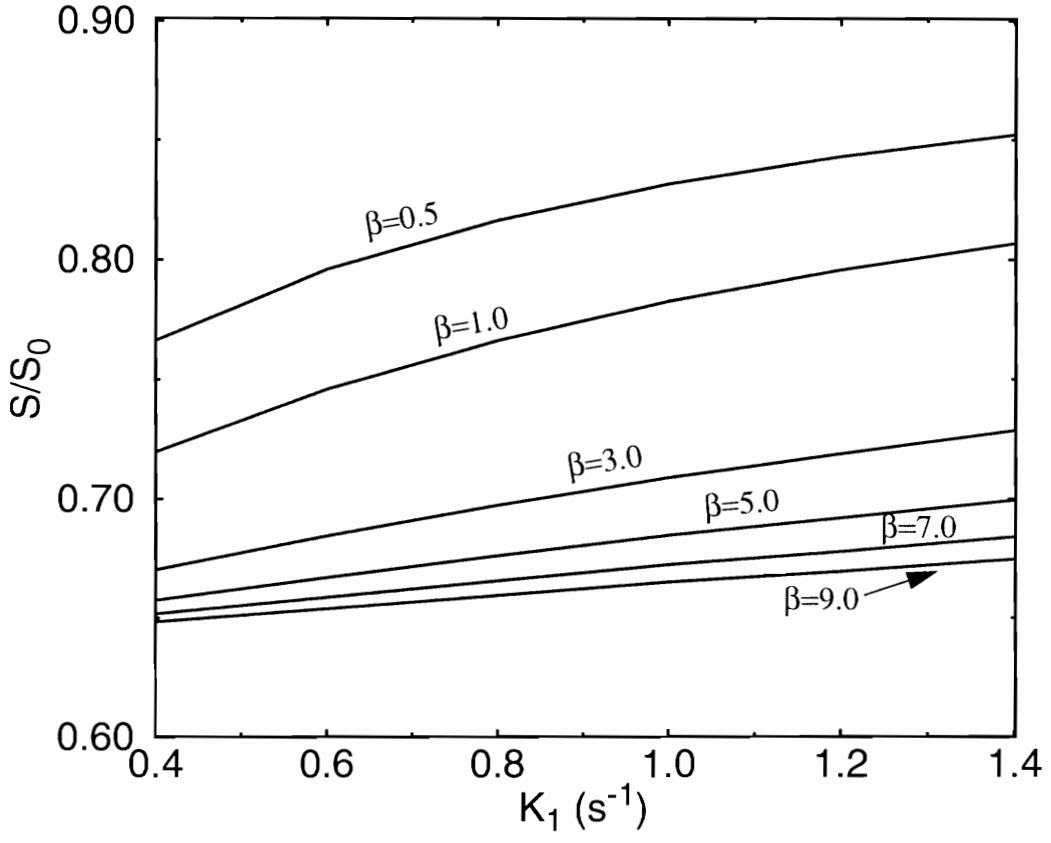

Fig. 3.10 Total signal integrated across the slice as a function of K_2 for different cross-sectional area ratios β. K_1 was fixed at 1.0 sec^{-1}. All other parameters are the same as those in Fig. 3.9.

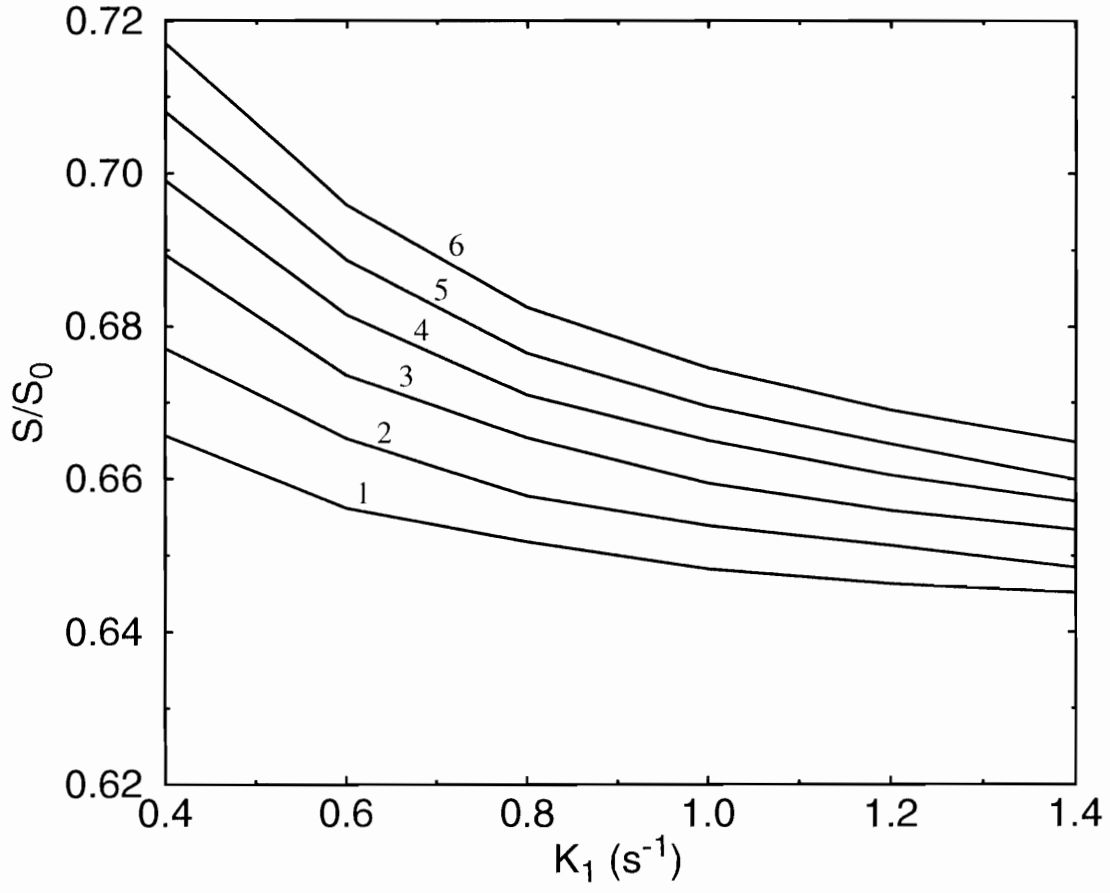

Fig. 3.11 Total signal integrated across the slice as a function of K_1 for different values of K_2: (1) 0.4, (2) 0.6, (3) 0.8, (4) 1.0, (5) 1.2, (6) 1.4. The area ratio β is fixed at 9.0. All other parameters are the same as those in Fig. 3.9.

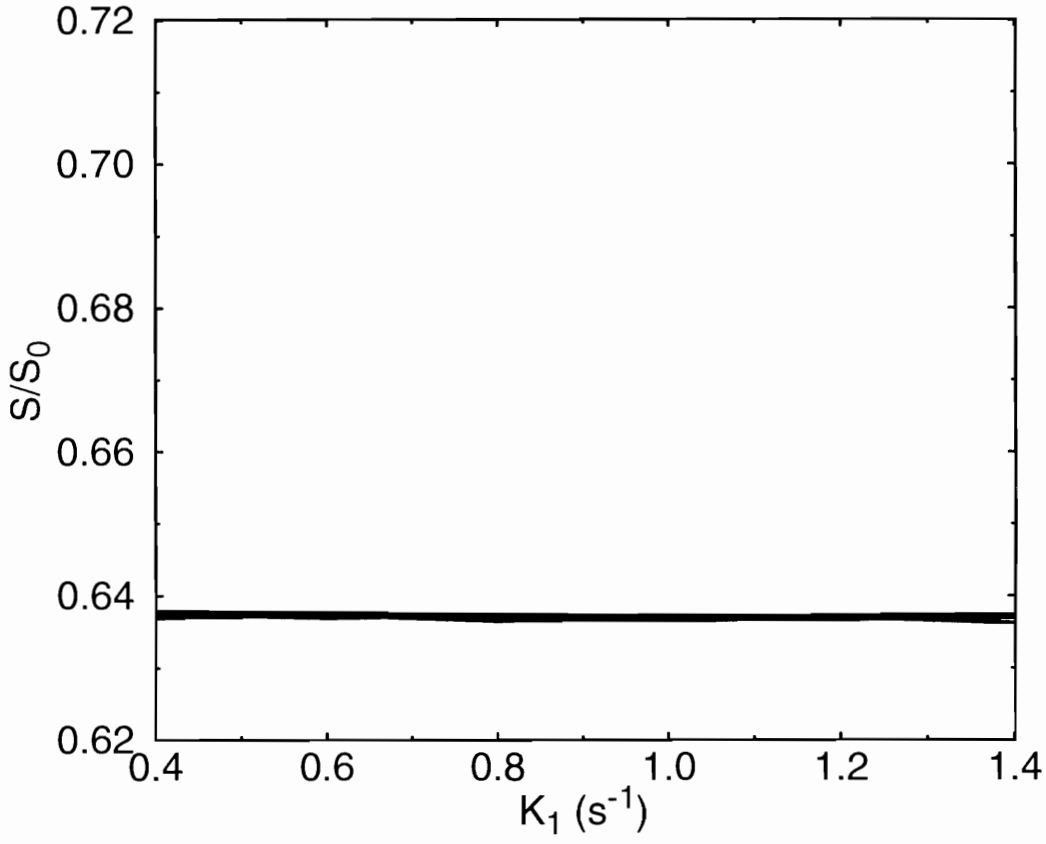

Fig. 3.12 The same as Fig. 3.11 except the flow velocity $W = 0$.

3.6 Discussion

Simulations of a tissue perfusion model show that the MRI signal is modulated by the evolution of excited spins as they relax, flow in capillary networks, disperse in tissue and capillaries, and as exchange takes place between the vascular and tissue compartments. The model is based upon the principles of indicator dilution where excited protons are used as the indicator or "tagged" material. The simulations indicate the modulation of the MRI signal is dependent upon the perfusion of tissue by blood which causes a time-of-flight effect as tissue is continuously excited by a selective rf pulse.

The simulation of a gradient refocusing pulse sequence shows that the slice profiles, including the excited and surrounding regions (upstream and downstream), can be divided into three distinct regions:

1) the unexcited, "fresh" spins entering the excited region have an evolution which is dominated by K_1, K_2 and β;

2) the central region extending to the end of the excited region has an evolution which is T_1 dominated;

3) the tissue outside and downstream of the excited region has an evolution which is dominated by K_1, K_2, and β and evolves somewhat opposite to that in region 1.

The region profiles are modulated by spins flowing in capillaries through the excited slice, and the location of each region boundary depends upon the velocity of the spins. At the transition between the boundaries, the slice profiles are smooth due diffusion processes which exchange spins between the regions in both the tissue and blood compartments. The diffusion effects are subtle because the diffusion coefficient is several orders of magnitude less than the flow velocity.

The total signal intensity (the integral of the longitudinal magnetization across the slice profile) is dominated by the flow velocity and the blood volume and depends less upon diffusion; whereas, Le Bihan's method (10) depends more strongly upon intravoxel incoherent motion due to molecular diffusion and the random arrangement of the capillary

network. In Le Bihan's model the signal modulation is accomplished by attenuating the transverse magnetization with the use of strong gradients that incoherently dephase diffusing spins. The attenuation of the transverse magnetization strongly depends upon the perfusion fraction f and the apparent diffusion coefficient D^* which is a function of the arrangement of the capillaries. Simulations show that with strong diffusion gradients of 0.34 G/cm an echo amplitude can vary more than 80% for D^* ranging between 0 and 2.0×10^{-4} cm^2/sec ; whereas, the total longitudinal magnetization varies less than 0.2%. Therefore, variations in D^* have a significant effect upon the transverse magnetization, but have very little effect upon the longitudinal magnetization signal.

The important aspect of being able to extract rate constants K_1 and K_2, even though slice profiles can show clear functional variations, depends strongly upon the sensitivity of the longitudinal magnetization to rate constant perturbations. From the simulations, the longitudinal magnetization signal appears to be more sensitive to rate constant variations for large blood volumes. The simulations used values of β between 0.5 - 9.0 which is equivalent to a blood volume of 10 - 67%. The larger blood volumes were investigated in order to study the effects of edema. However, for tissue such as the brain with blood volumes typically less than 10% ($\beta > 9$), the signal modulation will be small as can be deduced from Figs. 3.10 and 3.11. It is expected the two compartment model presented here would be most useful for organs like the kidney where the blood volume is in the range of 20-25%.[61]

Presently, work is continuing to develop methods for estimating the model parameters and to develop perfusion models which use the modulation of both the transverse and longitudinal magnetization to extract physiological parameters. In particular, estimation techniques are being investigated where model parameters are determined by least squares fitting to several MRI signal measurements which are obtained by modifying pulse sequence parameters. The combination of flow and diffusion imaging and the modeling of time-of-flight effects may help in isolating and determining

flow and diffusion parameters, thus making it easier to resolve perfusion fraction and rate constant parameters through estimation techniques.

Previous physiological studies[45] have proposed that a three compartment model is more appropriate for water exchange between blood and tissue where the intracellular space is considered a separate compartment. In general, compartments can be defined by boundaries such as the separation of organelles by membranes or the separation between two or more molecular populations.[51] Compartments are identified with quantities of a metabolite that show uniform and distinguishable kinetics of transformation or transport. NMR is useful in probing compartments because it is sensitive both to changes in the intracellular environment and to exchange effects. The degree of compartmentation is a function of the instrument in that it depends upon the time, spatial, and contrast resolution of the measurement system. Considering the present development of MRI technology, it is expected that the two compartment model is more appropriate to elicit in vivo physiological parameters.

Because of the clinical need, tests allowing noninvasive assessment of perfusion will continue to play an important role in clinical medicine. MRI presents promise as a technique by which an imaging protocol could image perfusion without the use of contrast agents or ionizing radiation.

CHAPTER 4

A MAGNETIC RESONANCE IMAGING VERIFICATION OF MULTICOMPARTMENT PERFUSION MODEL FOR A CHROMATOGRAPHY GEL PHANTOM

4.1 Introduction

Experimental verifications[16,27,30-33] of magnetic resonance tissue perfusion models have proven that perfusion processes in biological tissue that modulate the MRI signal intensity are more complicated than elementary models of MRI signal intensity are able to model. Le Bihan[16,30-32] developed a clever approach to measuring tissue vascular perfusion fraction by assuming that the motion of blood in the random arrangements of capillaries would give a diffusion signature similar to that of molecular diffusion, wherein flow through capillaries would mimic the Brownian motion of protons, thus attenuating the MRI signal intensity. However, he pointed out[16] that the model failed to take into account the exchange of protons between vascular and extravascular compartments. We have focused upon this aspect of tissue perfusion in an attempt to understand the effect on the MRI signal intensity of the exchange of excited protons between extravascular and intravascular compartments.[62] A model developed for tissue perfusion[62] is extended to model the exchange in chromatography columns, assuming that the exchange processes can be described by first-order kinetics similar to the approach used with indicator dilution theory, which utilize radioisotopes.[44,45] It is anticipated that the observed modulation of the MRI signal due to exchange between extrabead and intrabead compartments will be similar to the perfusion effect in biological tissue; however, the complexity of NMR makes the process of measuring perfusion processes, including exchange between

compartments, more complicated than that of indicator dilution techniques in PET[63] and SPECT.[64]

A two-compartment model of MRI signal intensity[62] was previously developed based upon the assumption that biological tissue can be represented by intravascular and extravascular compartments. The signal intensity was derived from modified Bloch equations that include the physiological parameters of blood flow velocity, perfusion fraction, diffusion, and rate of exchange between blood and tissue compartments. The model extended the Bloch-McConnell equations[51] by adding flow and diffusion terms. A key assumption was that the MRI signal is modulated by a time-of-flight effect whereby unexcited spins perfuse into the excited region and exchange from blood to tissue compartments, thus immediately increasing the slice signal intensity. However, the exchange of spins with extracapillary tissue delays the exit of spins from the slice, thereby decreasing their contribution to slice signal intensity in future repetitive pulse measurements. This model also included the effects of pseudodiffusion of a random array of capillaries in addition to the time-of-flight effect caused by the exchange of protons between blood and tissue. Computer simulations showed that the exchange of protons between intravascular and extravascular compartments could modulate the signal intensity in a slice- selective pulse sequence by as much as 2%.

For the work described in this paper chromatography columns were chosen as a phantom to verify experimentally the perfusion model. A Sephadex G-25 and a G-50 gel were selected so that the gel particles were of the same size but with different pore sizes to simulate different exchange rates between extrabead and intrabead compartments. The same particle size was used so that the signal differences would not be a function of different compartment volume sizes. It was initially anticipated that a three-compartment model that included exchange between, extrabead, intrabead, and immobile water compartments would better represent the MRI signal intensity than our previously developed two-compartment model.[62] The short relaxation times of the immobile water

compartment dominate the T_1 and T_2 decay of the entire sample and it seemed that the rate of exchange between free and immobile water could also modulate the signal. The immobile water compartment is composed of both loosely and tightly bound water inside the gel beads. It was expected that any T_1 and T_2 differences between the G-25 and G-50 gels would be due to the size difference of the tightly bound water component.

In this paper the modeling of exchange processes in chromatography columns is evaluated by using computer simulations and experiments to compare two- and three-compartment models. First a two-compartment model is developed to model the exchange of protons between extrabead and intrabead compartments of a chromatography column containing a Sephadex gel. The Bloch equations for the perfusion model are developed, including longitudinal and transverse magnetization and taking into account flow, diffusion, and fluid exchange between extrabead and intrabead compartments. Then the two-compartment model is extended to a three-compartment model with the addition of an immobile water compartment to model the exchange between free water and water bound to the gel matrix of the Sephadex beads. The two- and three-compartment models are applied to an MR imaging application that uses a spin-echo pulse sequence. The Bloch equations of second-order partial differential equations are solved numerically, using a finite difference technique to solve for the longitudinal and the transverse magnetization in a selectively excited slice of the gel phantom. The longitudinal and transverse magnetization is followed as a function of time to calculate the signal at the time of the echo. The simulation results of the two- and three-compartment models are compared with experimental results using two chromatography gel columns, one containing a G-25 gel and the other containing a G-50 gel, of two different pore sizes but the same intrabead to extrabead volume ratio.

4.2 Theoretical Background

4.2.1 Two-compartment Perfusion Model

Our previous two-compartment perfusion model was based on the use of MRI to excite a slice of tissue.[62] The excited tissue was considered to be a network of capillaries surrounded by a tissue matrix. Blood enters the slice from the arterial side and permeates through the tissue matrix. As it perfuses through the capillary network, the blood diffuses through the capillary endothelium into the tissue (extravascular space), which consists of cells and extracellular spaces. The perfused fluid in the tissue compartment also diffuses back into the vascular compartment and eventually exits the slice as the blood drains into the venous system. The perfusion of the excited slice and exchange produce a time-of-flight effect that modulates the signal detected in the slice. Bloch equations were developed, which include flow in the blood compartment, diffusion in both blood and tissue compartments, and exchange between the blood and tissue compartments.

A similar model was developed and evaluated for the chromatography gel phantoms shown in Fig. 4.1. The gel phantoms were used to simulate tissue, with the extrabead compartment corresponding to blood and the intrabead compartment corresponding to the extravascular tissue of the tissue two-compartment model. The model includes flow, diffusion, and exchange between extrabead and intrabead compartments within the excited slice. It is assumed that the protons in the extrabead spaces perfuse through the excited slice with a flow velocity V parallel to the z axis, and the intrabead compartment has a flow velocity equal to zero. The exchange of water and/or protons between the extrabead and intrabead compartment is described by the two-compartment model shown in Fig. 4.2. Water protons in the extrabead compartment diffuse into the intrabead compartment with a rate constant K_1, and water protons in the intrabead compartment diffuse back into the extrabead compartment with a rate constant K_2 (note: K_1 and K_2 are in units of inverse time normalized to the cross-sectional area of

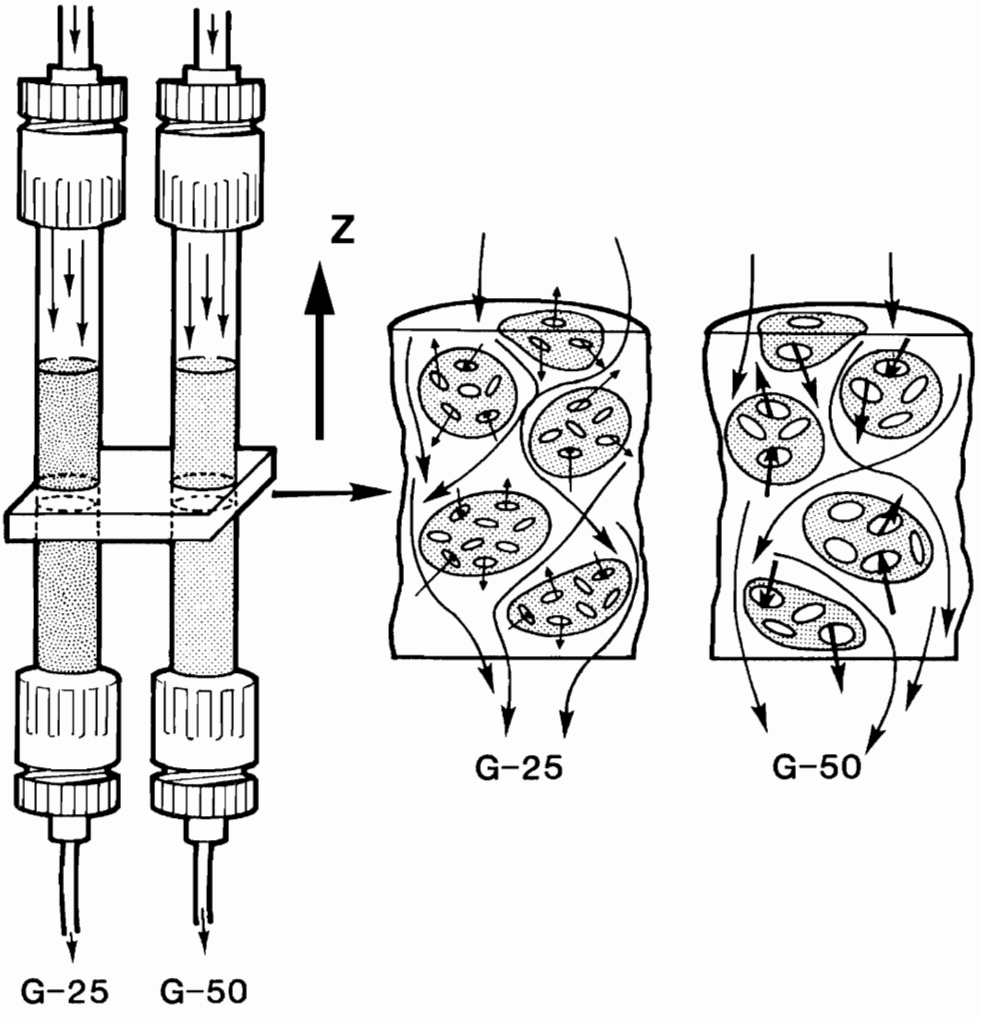

Fig. 4.1 Chromatography columns packed with Sephadex gel beads. The selected slice is also illustrated. Sephadex G-25 and G-50 have the same bead size but different pore sizes.

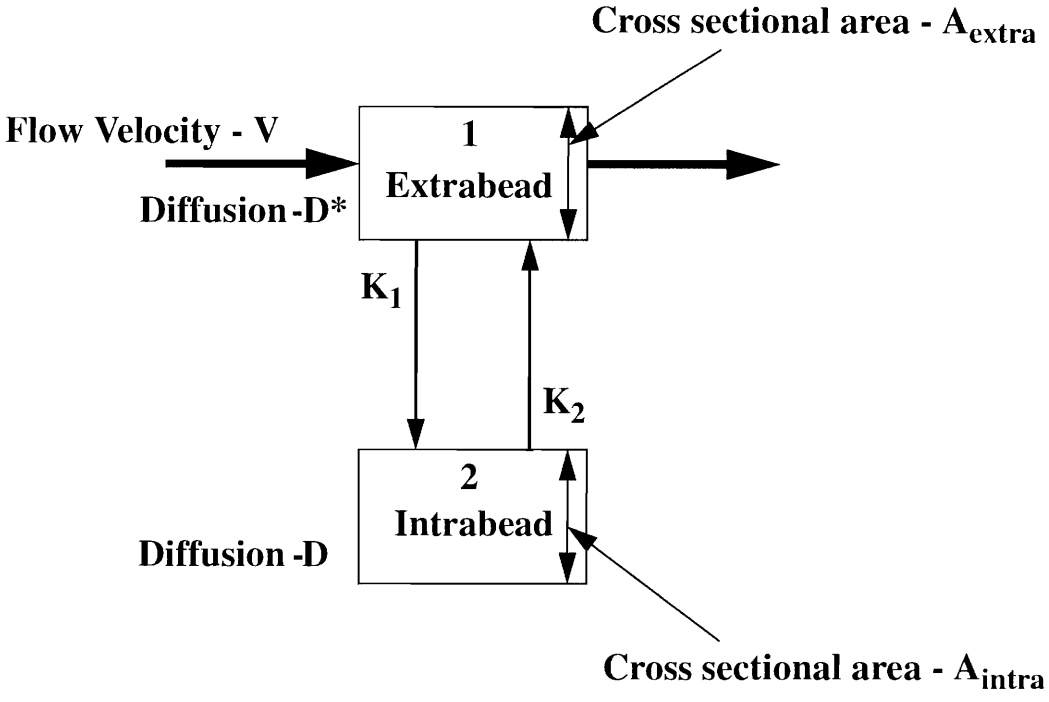

Fig. 4.2 The selected slice in Fig. 4.1 is represented here as a two-compartment model with exchange rate K_1 between extrabead and intrabead compartments and exchange rate K_2 between intrabead and extrabead compartments. β is the ratio of the intrabead A_{intra} to extrabead A_{extra} cross-sectional areas. D and D^* are the diffusion coefficients in the intrabead and extrabead compartments, respectively.

the intrabead compartment). The intrabead compartment has a diffusion coefficient D, whereas the extrabead compartment has a pseudodiffusion coefficient D^*.

In using MRI to measure perfusion, excited proton spins are used as the "tagged" material. For example, when a transaxial slice orthogonal to the z axis is excited, spins in the extrabead and intrabead compartments will be excited, producing a transverse magnetization in both compartments. The excited spins are predominantly water protons, which have an equilibrium magnetization ${M^1}_0$ and ${M^2}_0$ in the extrabead and intrabead compartments, respectively. After the excitation, the longitudinal magnetization and the transverse magnetization in extrabead and intrabead compartments can be followed as a function of time t and as a function of the position z along the slice selection axis.

Using ${M^1}_z(z,t)$ and ${M^2}_z(z,t)$ to denote the longitudinal magnetization in the extrabead and intrabead compartment, and $M^{1+}(z,t) = {M^1}_x(z,t) + i \cdot {M^1}_y(z,t)$ and $M^{2+}(z,t) = {M^2}_x(z,t) + i \cdot {M^2}_y(z,t)$ to denote the transverse magnetization in the extrabead and intrabead compartment, respectively, the following system of second-order partial differential equations are used to define the transverse and longitudinal magnetizations in the extrabead and intrabead compartments as a function of time t and position z:

$$\frac{\partial}{\partial t}M^{1+} = D^*\frac{\partial^2}{\partial z^2}M^{1+} - V\frac{\partial}{\partial z}M^{1+} - \left(\beta K_1 + \frac{1}{{T^1}_2}\right)M^{1+} + \beta K_2 M^{2+} - i\gamma G_z z M^{1+}, \tag{4.1}$$

$$\frac{\partial {M^1}_z}{\partial t} = D^*\frac{\partial^2 {M^1}_z}{\partial z^2} - V\frac{\partial {M^1}_z}{\partial z} - \left(\beta K_1 + \frac{1}{{T^1}_1}\right){M^1}_z + \beta K_2 {M^2}_z + \frac{{M^1}_0}{{T^1}_1}, \tag{4.2}$$

$$\frac{\partial}{\partial t}M^{2+} = D\frac{\partial^2}{\partial z^2}M^{2+} - \left(K_2 + \frac{1}{T^2_2}\right)M^{2+} + K_1 M^{1+} - i\gamma G_z z M^{2+}, \tag{4.3}$$

$$\frac{\partial M^2{}_z}{\partial t} = D\frac{\partial^2 M^2{}_z}{\partial z^2} - \left(K_2 + \frac{1}{T^2{}_1}\right)M^2{}_z + K_1 M^1{}_z + \frac{M^2{}_0}{T^2{}_1}, \tag{4.4}$$

where γ is the gyromagnetic ratio; β is the ratio of the intrabead volume to the extrabead volume, which is equivalent to the ratio of the available cross-sectional area of the intrabead compartment to the available cross-sectional area of extrabead compartment: $\beta = (A_{\text{intra}} \cdot \Delta z) / (A_{\text{extra}} \cdot \Delta z) = A_{\text{intra}}/A_{\text{extra}}$; $T^1{}_1$ and $T^2{}_1$ are the spin-lattice relaxation times in extrabead and intrabead compartments, respectively; and $T^1{}_2$ and $T^2{}_2$ are the spin-spin relaxation times in extrabead and intrabead compartments, respectively. A more detailed derivation of Eqs (4.1)-(4.4) can be found in our previous paper.[62]

In MR the "tagged" material is a vector with longitudinal and transverse magnetization that differs from isotope studies where the "tagged" tracer is a scalar quantity. The model described by Eqs. (4.1)-(4.4) and illustrated in Fig. 4.2 is an extension of the Bloch-McConnell equations[51] to include flow and diffusion, and incorporates the principles of compartmentization on which the concurrent flow models for isotope tracer studies are based.[44] The exchange between the intrabead and extrabead compartments can be thought of as an average diffusion. The model uses exchange rate constants K_1 and K_2, which are defined to be $K_1 = (k_1\phi)/A_{intra}$ and $K_2 = (k_2\phi)/A_{intra}$, where k_1 and k_2 are unidirectional permeability coefficients in units of cm/sec and ϕ is the surface area per unit length of the extrabead passway. The permeability coefficient k_1 is proportional to an average diffusion coefficient D_1: $k_1 = D_1/x$, where D_1 (cm^2/sec) is the average unidirectional diffusion across a membrane of thickness x. Note that in the two-compartment perfusion model the system of differential equations includes a diffusion term along the flow direction (the z-axis) that is perpendicular to the slice, and includes an overall average diffusion in the exchange rate constants to model exchange processes between compartments occurring transaxial to the flow direction. A diffusion coefficient is included as a coefficient of the differential form wherein following changes in

concentration as a function of position is desired; an overall average diffusion coefficient incorporated into the exchange rate constant is used where it is not desired to differentiate spatial differences in concentration.

4.2.2 Three-compartment Perfusion Model

A model for the chromatography gel phantom was developed to include the binding of water protons to the gel matrix as an immobile water compartment. It is known that in tissue the immobile water compartment can dominate the T_1 and T_2 relaxation times within an entire voxel.[65] In fact, the addition of a third compartment to the two-compartment model does not fully describe all species of protons because it does not differentiate between loosely bound and tightly bound water protons, which have very different relaxation times. We assume that loosely bound and tightly bound water protons are considered together in the immobile water compartment. The three-compartment model described in this section and the two-compartment model described in the previous section were evaluated to determine which one better modeled the MRI signal intensity obtained from experiments.

The three-compartment model in Fig. 4.3 is described by Bloch equations with flow in extrabead compartment, diffusion in both extrabead and intrabead compartments, and the exchange between extrabead, intrabead, and immobile water compartments. If we denote $M^3{}_z(z,t)$ as the longitudinal magnetization and $M^{3+}(z,t) = M^3{}_x + i \cdot M^3{}_y$ as the transverse magnetization in the immobile water compartment as a function of time t and position z along a selected slice, the system of second order partial differential equations is:

$$\frac{\partial}{\partial t}M^{1+} = \qquad , (4.5)$$

$$D^*\frac{\partial^2}{\partial z^2}M^{1+} - v\frac{\partial}{\partial z}M^{1+} - \left(\beta K_1 + \frac{1}{T^1{}_2}\right)M^{1+} + \beta\left(K_2 M^{2+} - K_3 M^{1+} + K_4 M^{3+}\right) - i\gamma G_z z M^{1+}$$

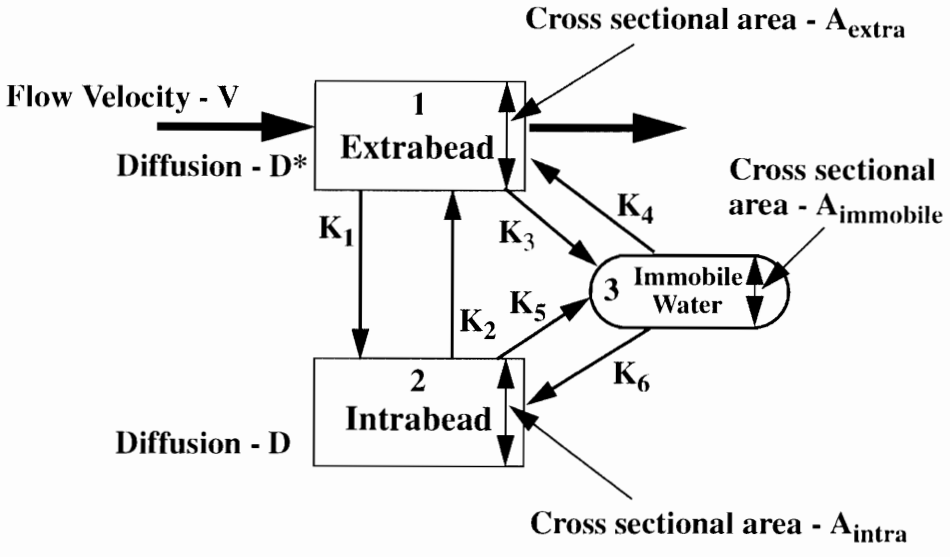

Fig. 4.3 The selected slice in Fig. 4.1 is represented here as a three-compartment model with exchange rate K_1 between extrabead and intrabead compartments, exchange rate K_2 between intrabead and extrabead compartments, exchange rate K_3 between extrabead and immobile water compartments, exchange rate K_4 between immobile water and extrabead compartments, exchange rate K_5 between intrabead and immobile water compartments, and exchange rate K_6 between immobile water and intrabead compartments. β is the ratio of the intrabead to extrabead cross-sectional areas and β_1 is the ratio of the intrabead to gel matrix cross-sectional areas.

$$\frac{\partial M^1{}_z}{\partial t} = D^*\frac{\partial^2 M^1{}_z}{\partial z^2} - V\frac{\partial M^1{}_z}{\partial z} - \left(\beta K_1 + \frac{1}{T^1{}_1}\right)M^1{}_z + \beta\,(K_2 M^2{}_z - K_3 M^1{}_z + K_4 M^3{}_z) + \frac{M^1{}_0}{T^1{}_1}, \quad (4.6)$$

$$\frac{\partial}{\partial t}M^{2+} = D\frac{\partial^2}{\partial z^2}M^{2+} - \left(K_2 + \frac{1}{T^2{}_2}\right)M^{2+} + (K_1 M^{1+} - K_5 M^{2+} + K_6 M^{3+}) - i\gamma G_z z M^{2+}, \quad (4.7)$$

$$\frac{\partial M^2{}_z}{\partial t} = D\frac{\partial^2 M^2{}_z}{\partial z^2} - \left(K_2 + \frac{1}{T^2{}_1}\right)M^2{}_z + (K_1 M^1{}_z - K_5 M^2{}_z + K_6 M^3{}_z) + \frac{M^2{}_0}{T^2{}_1}, \quad (4.8)$$

$$\frac{\partial}{\partial t}M^{3+} = -\left(\beta_1\,(K_4 + K_6) + \frac{1}{T^3{}_2}\right)M^{3+} + \beta_1\,(K_3 M^{1+} + K_5 M^{2+}) - i\gamma G_z z M^{3+}, \quad (4.9)$$

$$\frac{\partial M^3{}_z}{\partial t} = -\left(\beta_1\,(K_4 + K_6) + \frac{1}{T^3{}_1}\right)M^3{}_z + \beta_1\,(K_3 M^1{}_z + K_5 M^2{}_z) + \frac{M^3{}_0}{T^3{}_1}, \quad (4.10)$$

where K_i are the exchange rate constants (normalized to the intrabead cross-sectional area) between the various compartments; K_1 is the rate of exchange of water protons from the extrabead into the intrabead compartment, K_2 is the rate of exchange of water protons from the intrabead into the extrabead compartment, K_3 is the rate of exchange of water protons from the extrabead into the immobile water compartment, K_4 is the rate of exchange of water protons from the immobile water into the extrabead compartment, K_5 is the rate of exchange of water protons from the intrabead into the immobile water compartment, and K_6 is the rate of exchange of water protons from the immobile water into the intrabead compartment. D and D^* are diffusion coefficients in the intrabead and extrabead compartments, respectively. The ratio of the intrabead volume to the extrabead volume is denoted by $\beta = (A_{\text{intra}} \cdot \Delta z) / (A_{\text{extra}} \cdot \Delta z) = A_{\text{intra}}/A_{\text{extra}}$, where A_{intra} and A_{extra} are the cross-sectional areas for the intra- and extrabead compartment, respectively. The ratio of the intrabead volume to the immobile water volume is denoted by $\beta_1 = (A_{\text{intra}} \cdot \Delta z) / (A_{\text{immobile}} \cdot \Delta z) = A_{\text{intra}}/A_{\text{immobile}}$, where A_{immobile} is the cross-

sectional area for the immobile water compartment.

The choice of the rate constants was determined such that at equilibrium $K_1M^1{}_0 = K_2M^2{}_0$, $K_3M^1{}_0 = K_4M^3{}_0$, and $K_5M^2{}_0 = K_6M^3{}_0$ are valid. Because the magnitude of magnetization at equilibrium is virtually proportional to the number of protons per unit volume in a particular compartment, $M^1{}_0$, $M^2{}_0$, and $M^3{}_0$ actually are proportional to each respective compartment volume fraction.

4.3 Methods

4.3.1 Computer Simulations for the Two-compartment Model

Simulations were performed for the two-compartment perfusion model to evaluate the modulation of the MRI signal as a function of the exchange rate between extrabead and intrabead compartments. In all simulations we assumed the application of a perfect rectangular slice selective $90°_x$ rf pulse with no phase dispersion over a 0.3 cm slice. Slice profiles of the transverse and longitudinal magnetization were calculated numerically using finite difference equations (Appendix A).[7]

The single-step nature of the finite difference algorithm requires initial conditions for $M^1{}_z(z, t)$, and $M^2{}_z(z, t)$, $M^{1+}(z, t)$, and $M^{2+}(z, t)$ at $t = 0$. In simulating the excitation of a 0.3 cm slice, we assumed the boundary conditions for the extrabead compartment were

$$M^1{}_z(z, t{=}0) = \begin{cases} 0 & -0.15 < z < 0.15cm \\ M^1{}_0 & otherwise \end{cases}, \tag{4.11}$$

$$M^1{}_y(z, t{=}0) = \begin{cases} M^1{}_0 & -0.15 < z < 0.15cm \\ 0 & otherwise \end{cases}, \tag{4.12}$$

and the boundary conditions for the intrabead compartment were

$$M^2_z(z, t{=}0) = \begin{cases} 0 & -0.15 < z < 0.15cm \\ M^2_0 & otherwise \end{cases}, \tag{4.13}$$

$$M^2_y(z, t{=}0) = \begin{cases} M^2_0 & -0.15 < z < 0.15cm \\ 0 & otherwise \end{cases}. \tag{4.14}$$

The equilibrium magnetization in the extrabead and intrabead compartments were chosen to have a value equal to its fractional volume contribution of the total equilibrium magnetization of 0.9: $M^1_0 = 0.9/(1+\beta) = 0.393$, where $\beta = 1.28$ and $M^2_0 = 0.507$. The value of 0.9 is the fraction of water protons contributing to the MRI signal. It was assumed that the gel matrix made up 10% of the total volume and did not contribute to the signal. Simulations were performed for $K_1 = 0, 1, 2, 3$ sec^{-1}. In order to satisfy the equilibrium condition $K_1 M^1_0 = K_2 M^2_0$, K_2 was set to $K_2 = K_1\left(M^1_0/M^2_0\right)$.

After excitation the evolution of the magnetization as a function of time was calculated in the slice and also in adjacent regions. The number of grid points L in time was chosen to be 40,000. This covered a time interval corresponding to a TR of 0.4 sec with a grid size $h = 1\times10^{-5}$ sec. The grid size k in z was determined from $k = (6h)^{-1/2}/8 = 0.0009682$ cm.[60,62] Simulations were performed so as to represent a 0.7 cm segment length of the gel phantom so that with this grid size there were approximately $N = 723$ grid points along the spatial coordinate z.

The spins in the extrabead compartment relaxed with T^1_1 and T^1_2 relaxation times of both equal to 2.0 s, simulating that of tap water. The spin relaxation time T^2_1 in the intrabead compartment was calculated to be equal to 390 ms using the expression: $1/T_1 = \left(1/T^1_1 + \beta/T^2_1\right)/(1+\beta)$. Similarly T^2_2 was calculated to be equal to 32 ms. These were calculated assuming $\beta = 1.28$ and assuming a $T_1 = 0.604$ sec and

T_2 = 0.057 sec for the entire sample, which corresponds to measurements of the G-25 gel in Table 4.1. Using the initial conditions [Eqs. (4.11)-(4.14)], the finite difference method[7] was used to solve Eqs. (4.2) and (4.4) for the profile of the longitudinal magnetization at a time, TR, of 0.4 s, where upon the next $90°_x$ rf pulse was applied. This cycle was repeated three times. (Further repetitions yielded negligible changes in the magnetization profile.) After the 4th $90°_x$ rf pulse the finite difference technique was used to solve Eqs. (4.1) and (4.3) for the transverse magnetization as a function of time and position across the slice, from which a slice profile of signal intensity was calculated at the time of the echo TE=15 ms later. This gave a map of the signal intensity across the slice at the time of the echo after the fourth perfect rectangular slice selective 90° rf pulse. In our previous paper[62] we showed that the longitudinal magnetization reaches a steady state approximately after three repetitions of a 90° pulse for a T_1 of 0.5 s and a TR of 0.5 s.

A pseudodiffusion coefficient was calculated for the extrabead compartment based upon a statistical approach that describes Brownian motion as a series of random molecular jumps.[30] The pseudodiffusion coefficient D^* can be described as $D^* = \overline{v \cdot l}/6$, where $\bar{l}$ is the mean length of the jumps and $\bar{v}$ is the mean proton velocity. In the MRI experiments each chromatography column was perfused with a flow velocity V of anywhere between 0 to 0.6 mm/sec. If we assume that the mean diameter of the swelled bead is 100 μm and the velocity is as high as 0.6 mm/sec, we can expect a value for D^* as high as 1.0×10^{-4} cm^2/sec in the extrabead compartment. Therefore, a value of $D^* = 1.0 \times 10^{-4}$ cm^2/sec was chosen for the extrabead compartment, which is four times greater than that of pure water at $40°C$: $D = 2.5 \times 10^{-5}$ cm^2/sec. The value for pure water was chosen for the diffusion coefficient in the intrabead compartment.

The total signal from an excited slice of the gel phantom is the sum of the signal contributions from the extrabead and intrabead compartments, and is proportional to the sum of the transverse magnetization in each compartment at the time of the measurement. The total magnetization in the transverse plane as a function of z is the weighted sum of

Table 4.1 Relaxation time measurements for Sephadex gel phantoms G-25, and G-50. An inversion recovery pulse sequence was used to measure T_1 and the results were calculated by linear fitting the logarithm of the signals for varied TI. T_2 was calculated using a spin-echo pulse sequence for different TE.

Sephadex gel	T_1 (ms)	T_2 (ms)
G-25	603.57±3.38	56.97 ± 1.84
G-50	637.11 ± 2.65	455.20 ± 5.77

the transverse magnetization in the extrabead compartment and the transverse magnetization in the intrabead compartment:

$$M^+(z,t) = \frac{\Delta z A_{\text{extra}}}{\Delta z\,(A_{\text{extra}} + A_{\text{intra}})} M^+(\text{extrabead}) + \frac{\Delta z A_{\text{intra}}}{\Delta z\,(A_{\text{extra}} + A_{\text{intra}})} M^+(\text{intrabead}) = \frac{1}{1+\beta} M^{1+} + \frac{\beta}{1+\beta} M^{2+} \qquad (4.15)$$

The total signal from the entire slice is obtained by integrating the magnetization contribution from the extrabead and intrabead compartments over the slice coordinate z:

$$S_V(t) = \frac{1}{1+\beta} \int (M^{1+} + \beta M^{2+})\, dz\,. \qquad (4.16)$$

For the two-compartment model we assumed $\beta = 1.28$. The signal was calculated by integrating from -0.15 cm to 0.15 cm at t = TE = 15 ms after the fourth 90° pulse. Since the finite difference method gives values at grid spacing $k = 0.009682$ cm for z, the integral was calculated by summing over 310 grid points within the 0.3 cm slice.

In general the total MRI signal intensity is a function of flow velocity V, diffusion coefficients D and D^*, volume ratios β and β_1, and exchange rate constants K_j, as well as M_0, T_1, T_2 for each compartment, the time of echo TE, and the repetition time TR:

$$S_V(\text{TE}) = F\left(V, D, D^*, \beta, \beta_1, K_j, M^{i}_{0}, T^{i}_{1}, T^{i}_{2}, \text{TR}, \text{TE} \right), \qquad (4.17)$$

where i is compartment index and j is exchange rate constant index. At zero velocity V_0 Eq. (4.17) becomes

$$S_{V_0}(\text{TE}) = F\left(0, D, D^*, \beta, \beta_1, K_j, M^{i}_{0}, T^{i}_{1}, T^{i}_{2}, \text{TR}, \text{TE} \right). \qquad (4.18)$$

In our computer simulations, the logarithm of the ratio of $S_V(TE)$ to $S_{V_0}(TE)$ was evaluated and plotted as a function of flow velocity V:

$$ln\left(\frac{S_V(\mathrm{TE})}{S_{V_0}(\mathrm{TE})}\right) = ln\frac{F\left(V, D, D^*, \beta, \beta_1, K_j, M^i{}_0, T^i{}_1, T^i{}_2, \mathrm{TR}, \mathrm{TE}\right)}{F\left(0, D, D^*, \beta, \beta_1, K_j, M^i{}_0, T^i{}_1, T^i{}_2, \mathrm{TR}, \mathrm{TE}\right)}. \tag{4.19}$$

These results were plotted as a function of flow velocity from 0 to 0.6 mm/sec.

4.3.2 Computer Simulations for the Three-compartment Model

Simulations were performed for the three-compartment model. The same slice-selective 90° pulse sequence used in the previous section was simulated, giving a 0.3 cm slice. Keeping the diffusion coefficients and the TE the same as those used for the two-compartment model, the slice profiles of the MRI signal were calculated numerically using the same finite difference approach (Appendix B). The boundary conditions for extrabead and intrabead compartments were the same as Eqs. (4.11)-(4.14), and the boundary conditions for the immobile water compartment were

$$M^3{}_z(z, t{=}0) = \begin{cases} 0 & -0.15 < z < 0.15cm \\ M^3{}_0 & otherwise \end{cases}, \tag{4.20}$$

$$M^3{}_y(z, t{=}0) = \begin{cases} M^3{}_0 & -0.15 < z < 0.15cm \\ 0 & otherwise \end{cases}. \tag{4.21}$$

The total signal from the slice was calculated by integrating across the slice the transverse magnetization contribution from each compartment:

$$S_V(t) = \frac{1}{1+\beta+\frac{\beta}{\beta_1}}\int\left(M^{1+} + \beta M^{2+} + \frac{\beta}{\beta_1}M^{3+}\right)dz. \tag{4.22}$$

In the simulations the integration was performed from -0.15 cm to 0.15 cm at the time of the echo (TE=15 ms) after the fourth 90° pulse.

For the three-compartment model, the normalized signal intensity $[ln(S_V(TE)/S_{V_0}(TE))]$ was plotted as a function of flow for various values of K_1, K_5, and the physical intrabead to extrabead volume ratio $\beta_{physical}$. Also, simulations were performed to evaluate the effect of slice thickness.

4.3.2.1 Determination of the Volume Fractions

The Sephadex G-25 and G-50 gel phantoms were selected so that the physical intrabead to extrabead volume ratio $\beta_{physical}$ were the same but each gel had a different pore size to simulate different exchange rates. In these simulations it was assumed that each gel had four physical regions as illustrated in Fig. 4.4, such that the summation of the four volume fractions equaled to 1:

$$f_{extra} + f_{intra} + f_{immobile} + f_{matrix} = 1, \tag{4.23}$$

where f_{extra} is the extrabead free-water volume fraction, f_{intra} is the intrabead free-water volume fraction, $f_{immobile}$ is the intrabead immobile water volume fraction, and f_{matrix} is the gel matrix volume fraction. It was assumed that the extrabead free-water fraction was the same as the physical extrabead volume fraction; whereas it was assumed that the inside of the bead was composed of an intrabead free-water compartment and an intrabead immobile water compartment. Therefore, β defined as the ratio of intrabead free-water volume to the extrabead water volume differed from $\beta_{physical}$.

The ratio β_1 of intrabead free-water volume to immobile water volume can be expressed in terms of $\beta_{physical}$ and β. Assuming that the gel matrix makes up 10% of the total volume ($f_{matrix} = 0.1$), β_1 can be determined from Eq. (4.23) by setting $\beta_{physical} = (f_{intra} + f_{immobile})/f_{extra}$ and $\beta = f_{intra}/f_{extra}$:

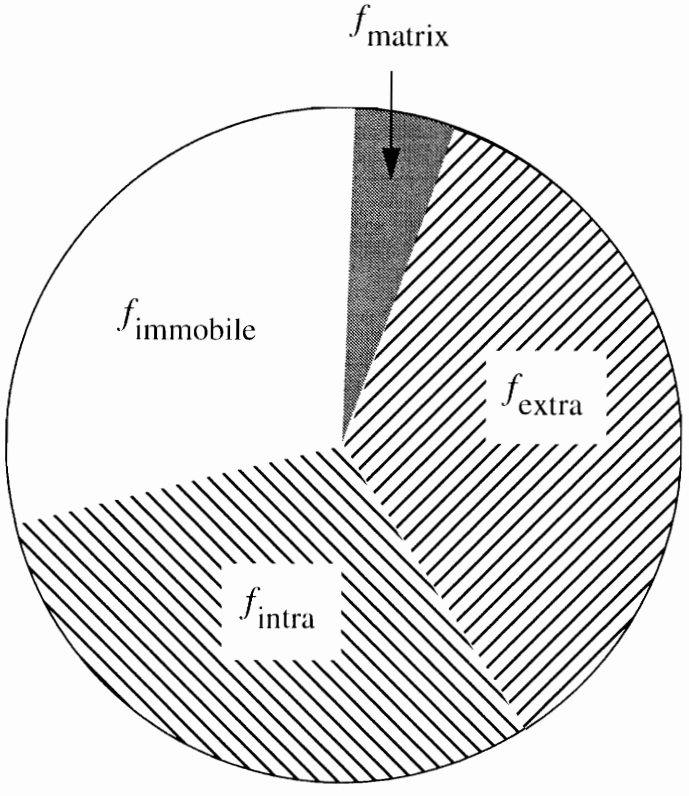

Fig. 4.4 The gel phantom is segmented into four volume fractions. The symbol f_{matrix} is the volume fraction of the gel matrix, f_{extra} is the volume fraction of the extrabead free water, f_{intra} is the volume fraction of the intrabead free water, and $f_{immobile}$ is the volume fraction of the intrabead immobile water.

$$\beta_1 = \frac{f_{intra}}{f_{immobile}} = \frac{\beta f_{extra}}{0.9 - f_{extra}(1+\beta)} = \frac{\beta}{\beta_{physical} - \beta}, \tag{4.24}$$

where

$$f_{extra} = \frac{0.9}{1+\beta_{physical}}. \tag{4.25}$$

4.3.2.2 Determination of Equilibrium Magnetizations

If we assume that the total magnetization is equal to the summation of the volume fractions for the three-compartments containing water:

$$M_0 = f_{extra} + f_{intra} + f_{immobile} = 0.9, \tag{4.26}$$

the equilibrium magnetization for each compartment can be assigned a value equal to its volume fraction. Therefore, using Eq. (4.25) produces

$$M^1{}_0 = f_{extra} = \frac{0.9}{1+\beta_{physical}}. \tag{4.27}$$

Likewise, using $\beta = f_{intra}/f_{extra}$ produces

$$M^2{}_0 = f_{intra} = \frac{0.9\beta}{1+\beta_{physical}}. \tag{4.28}$$

To calculate the equilibrium magnetization $M^3{}_0$ for the immobile water compartment, substituting the results in Eqs. (4.27) and (4.28) into Eq. (4.26) gives

$$M^3{}_0 = f_{immobile} = 0.9\left(1 - \frac{(1+\beta)}{1+\beta_{physical}}\right). \tag{4.29}$$

4.3.2.3 Determination of Exchange Rate Constants

In the simulations the exchange rate constants K_1, K_3, and K_5 were allowed to vary. The exchange rate constants K_2, K_4, and K_6 were determined in terms of K_1, K_3, K_5, $\beta_{physical}$, and β by satisfying the equilibrium conditions $K_1 M^1{}_0 = K_2 M^2{}_0$, $K_3 M^1{}_0 = K_4 M^3{}_0$, and $K_5 M^2{}_0 = K_6 M^3{}_0$:

$$K_2 = \frac{K_1 M^1{}_0}{M^2{}_0}, \tag{4.30}$$

$$K_4 = \frac{K_3 M^1{}_0}{M^3{}_0}, \tag{4.31}$$

$$K_6 = \frac{K_5 M^2{}_0}{M^3{}_0}, \tag{4.32}$$

where $M^1{}_0$, $M^2{}_0$, and $M^3{}_0$ are given in Eqs. (4.27), (4.28), and (4.29).

In magnetization transfer experiments performed on the chromatography columns, K_3 or K_5 could not be measured, implying that K_3 and K_5 had to be significantly greater than $1/T_1$ for water. Therefore, the value of K_5 was always chosen in the simulations to be greater than $1/T_1$ for water.

4.3.2.4 Determination of Relaxation Times

Using the fast-exchange model of Zimmerman and Brittin (wherein the exchange of protons between the compartments is fast relative to relaxation, i.e., a proton can easily reach any compartment and relax in any one of them), the T_1 relaxation time for the entire sample is

$$\frac{0.9}{T_1} = \frac{f_{extra}}{T^1{}_1} + \frac{f_{intra}}{T^2{}_1} + \frac{f_{immobile}}{T^3{}_1} \quad . \tag{4.33}$$

Assuming $T^1_1 = T^2_1$, Eq. (4.33) can be written as

$$\frac{0.9}{T_1} = \frac{f_{extra} + f_{intra}}{T^1_1} + \frac{f_{immobile}}{T^3_1} \quad . \tag{4.34}$$

Solving for T^3_1 gives

$$T^3_1 = \frac{0.9 - f_{extra}(1+\beta)}{\frac{0.9}{T_1} - \frac{f_{extra}(1+\beta)}{T^1_1}}, \tag{4.35}$$

where f_{extra} is given in Eq. (4.25). Similarly,

$$T^3_2 = \frac{0.9 - f_{extra}(1+\beta)}{\frac{0.9}{T_2} - \frac{f_{extra}(1+\beta)}{T^1_2}}. \tag{4.36}$$

The T^1_1, T^1_2, T^2_1, and T^2_2 relaxation times in both the extrabead and the intrabead compartments were chosen to be 2.0 s, equal to that of tap water. To simulate the chromatography columns with Sephadex G-25 and G-50 gels, the T^3_1 and T^3_2 relaxation times in the immobile water compartment were calculated from Eqs. (4.35) and (4.36) using T_1 and T_2 measurements of the entire sample given in Table 4.1.

4.3.3 Chromatography Gel Phantom Experiments

A gel-type phantom was chosen to study perfusion processes similar to those that might occur in tissue. It has been shown that gels can be used to simulate the T_1 and T_2 properties of tissue.[66] Different gels that have been studied include acrylamide,[67,68] hydrogel,[66] and agarose.[69-71] Dextran Sephadex gels were selected for our study rather than those mentioned because two gels (G-25 and G-50) with the same bead size but different pore sizes could be selected in order to study, independent of bead size, the effect

of different exchange rates between extrabead and intrabead compartments on the MRI signal.

A dextran Sephadex gel is a polysaccharide composition, built from glucose residues.[72,73] The dextran is cross-linked to form a three-dimensional network of polysaccharide chains. When in solvent, the three-dimensional network swells into gel beads. The polysaccharide chains can be cross-linked with different size pores, providing different permeabilities for chromatography applications.

In the phantom experiments a Sephadex G-25 gel was packed in one column and a G-50 gel was packed in the other. The G-50 gel has almost twice the pore size of the G-25 gel. The bead diameters and the ratio of intrabead to extrabead volume are the same. Measurements of MRI signal intensity as a function of the rate of exchange between extrabead and intrabead compartments were made using these two gels.

4.3.3.1 Preparation of the Gel Chromatography Column

Before packing the columns, Sephadex G-25 and G-50 gels were swollen in two beakers from dry storage form using water as a solvent. Best results were obtained using a hot water bath solvent. Sephadex G-25 has a bed volume of 2.5 ml/gram and G-50 has a bed volume of 5.0 ml/gram of Sephadex.[73] The gels were swollen for 10 hours.

For packing, the columns were first placed in an upright position. Water was injected onto the filter secured to the bottom cap of the chromatography column to remove any air trapped in the filter. Then the bottom cap was secured to the chromatography column. Water was passed through the column to check for any air blockage in the filter.

Then excess water was decanted from the swollen gels in each beaker so that approximately 70 percent of gel remained. Gel and water were gently stirred to give a uniform mixture.

With the bottom valve open to allow flow, a third of the chromatography column was filled with water. Then the gel mixture was poured along a glass rod into the column. The gel was poured uniformly so as not to trap air bubbles. As the gel was packed, three

regions in the column could be seen: a bottom layer of packed gel, above that a layer of gel and excess water, and above that pure water. The bottom packed layer increased up the column as the gel in the middle layer settled. The bottom packed layer was not disturbed. The column was gently tapped along the outside as the gel settled. Once the gel settled, water was passed through the column to stabilize the packing.

4.3.3.2 Measuring the Physical Volume Ratio $\beta_{physical}$

For each packed column the total volume (v_{total}) was found from the equation $v_{total} = \pi r^2 l$, wherein the radius of the column r was known (1.6 cm) and the height of the packed gel l was measured. The volume outside the gel ($v_{outside}$) was found by chromatography of a sample of Blue Dextran. The water that carried the Blue Dextran through the packing corresponds exactly to the liquid volume between the particles. Blue Dextran has a high molecular weight so it will not flow into the gel bead, but remains in the water outside as it flows through the packed gel. The volume inside the gel bead (v_{inside}) was computed according to the following equation:[73]

$$v_{inside} = \frac{S_r d}{(S_r d + \rho)} (v_{total} - v_{outside}) , \tag{4.37}$$

where S_r is the water regain, which is defined as the grams of water taken up by 1 gram of gel during swelling. The values of S_r were obtained from Reference 73: for Sephadex G-25, $S_r = 2.5$, and for Sephadex G-50, $S_r = 5.0$. The density of the gel in its swollen state is $d = 1.13$ g/ml for G-25 and $d = 1.07$ g/ml for G-50. The density of water ρ is 1.0 g/ml.

From the measurement results of $v_{outside}$ and v_{inside} we calculated $\beta_{physical} = v_{inside}/v_{outside}$. The reference values[73] and measured values of $\beta_{physical}$ are listed in Table 4.2. The difference between the reference value and the measured value is believed to be caused by temperature differences. G-50 has a pore size almost double that

Table 4.2 Volume ratio $\beta_{physical}$ measurements. $\beta_{physical} = V_i/V_0$ was calculated from the measurements of V_i and V_0, where V_i is the physical intrabead volume and V_0 is the physical extrabead volume. Before and after the MRI experiments the volume ratio $\beta_{physical}$ was measured. The results listed here were from the average of two measurements. The difference between the reference value and the measured value is believed to be caused by the temperature difference.

Sephadex gel	$\beta_{physical}$ (Reference)	$\beta_{physical}$ (Measured)
G-25	1.25	1.28 ±0.023
G-50	1.25	1.28 ±0.018

of the G-25 gel.[22] Because the exchange rate is proportional to the pore size on the gel bead surface, it was expected that the exchange rate for G-50 will also be double that of the G-25 gel.

4.3.3.3 MRI Experiment

Both columns in Fig. 4.1 were oriented parallel to each other in a 1.5T imager with water flowing through each column. Before and after the MRI experiment the volume ratio $\beta_{physical}$ was measured. The results listed in Table 4.2 were from the average of the two measurements. A five- gallon container with a constant water level was used to obtain hydrostatic pressure. Water was allowed to flow through the tubes connected to the chromatography columns. Care was taken to avoid air bubbles in the tubes, which could flow through the image slice during the scan or change the flow rate by blocking the passageway in the tubes.

For each MRI experiment, a single spin echo image was obtained in a plane perpendicular to the cylinder axis in the middle portion of the packed gel. Flow compensation gradient in the slice selection direction was used to eliminate any phase dispersion due to constant flow in the slice direction. Each image was obtained with a 48 cm field of view using a 256x128 matrix, a 3 mm slice thickness, TR=400 ms and TE=15 ms. For each flow rate from zero to the maximum used, five such images were obtained. For each image the signal was averaged over a circular region of interest of approximately 16 pixels contained just within the transaxial slice of the column. This average measurement was normalized to the average of the five such measurements obtained at zero flow rate. Finally, the five normalized measurements at each mean flow velocity were averaged.

The flow rates were measured before and after the five scans at each flow rate by measuring the volume of water collected over a two-minute period. The mean flow velocities were then determined by taking the measured flow rates and dividing by the extrabead cross- sectional area perpendicular to the direction of flow within the column.

The range of mean velocity used in these experiments was kept between 0 and 0.66 mm/sec. The velocity allowed for the Sephadex G-25 and G-50 gels packed in a 20 cm column is about 1.0 mm/sec. In general, a velocity higher than this maximum can result in deformation of the gel. Even at mean velocities slightly below this maximum, it has been observed that the increased hydrostatic pressure can still slightly compress the gel. The effect of this slight compression on the $\beta_{physical}$ measurements was taken into account by averaging the volume measurements before and after the MRI scan.

4.4 Results

4.4.1 Computer Simulations for the Two-compartment Model

The results of the computer simulations for the two-compartment model are shown in Fig. 4.5. For each flow velocity simulated, the integrated MRI signal was calculated at TE=15 ms after the fourth 90° pulse (TR=0.4 s) using Eq. (4.16), and this calculation was normalized to the integrated MRI signal at a flow velocity $V = 0$. The computer simulations show that the MRI signal intensity is modulated by flow in the extrabead compartment as well as the exchange between the intrabead and extrabead compartments. The curves of the normalized signal intensities for $K_1 = 0, 1, 2, 3$ sec^{-1} are clearly separated. The separation of the curves increases with the increase in flow velocity, which clearly shows that the time-of-flight effect is a key factor in this model. In all simulation results the curve with the greater exchange rate is always below the one with a lesser exchange rate. Greater rate constants cause a delayed exit from the selected slice, increasing the saturation of spins and reducing the MRI signal.

4.4.2 Computer Simulations for the Three-compartment Model

The results of the computer simulations for the three-compartment model are shown in Figs. 4.6-4.9. Curves of the natural logarithm of the normalized MRI signal intensity as a function of flow are plotted. The scale in the plots is kept constant so that comparisons can more easily be made.

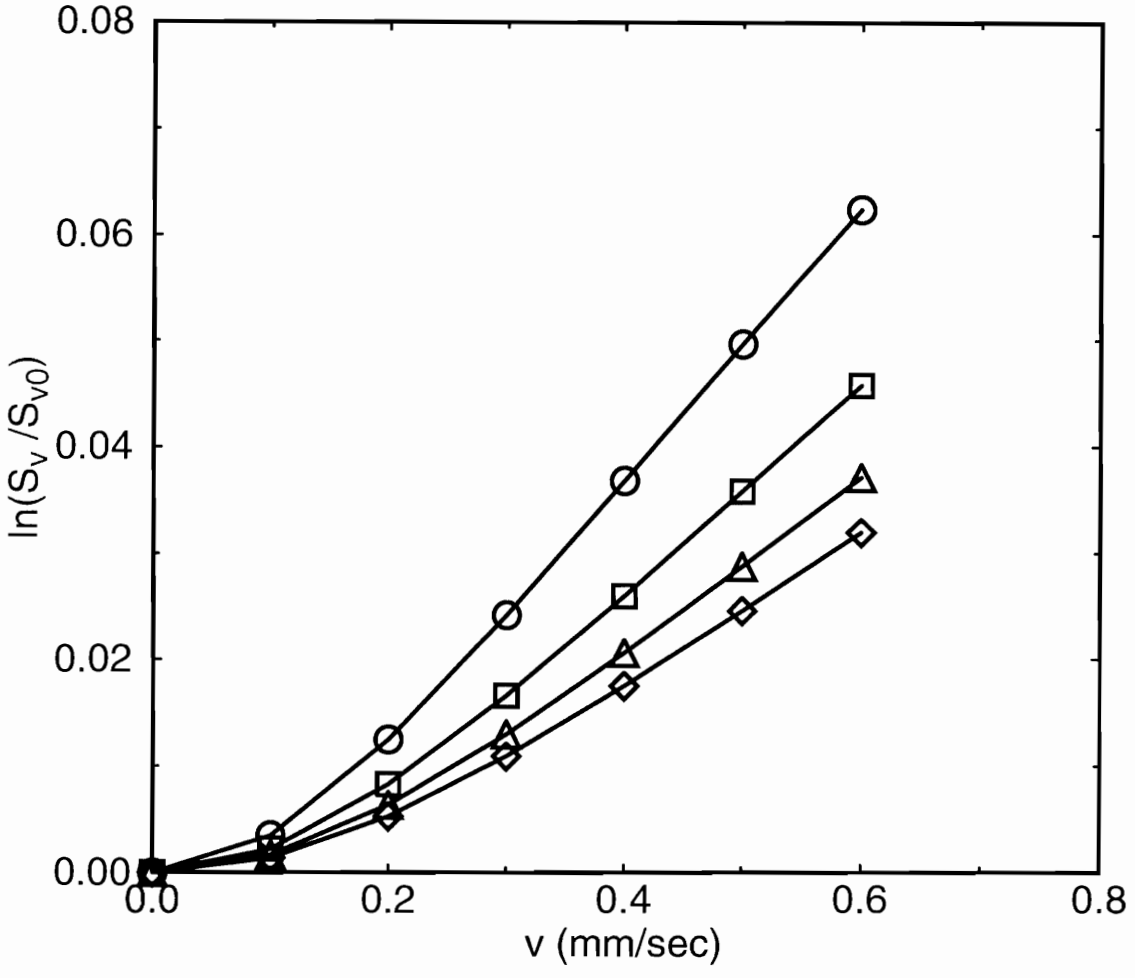

Fig. 4.5 Two-compartment model computer simulations. The natural logarithm of the integrated MRI signal intensity normalized to the calculation at a flow velocity $V = 0$ is plotted as a function of flow for exchange rates: $K_1 = 0$ sec^{-1} ($K_2 = 0$ sec^{-1}) (circle), $K_1 = 1$ sec^{-1} ($K_2 = 0.78$ sec^{-1}) (square), $K_1 = 2$ sec^{-1} ($K_2 = 1.56$ sec^{-1}) (triangle), $K_1 = 3$ sec^{-1} ($K_2 = 2.34$ sec^{-1}) (diamond). The simulations assumed that $\beta = 1.28$. The $T^1{}_1$ and $T^1{}_2$ relaxation times in the extrabead compartment were both equal to 2.0 s, simulating that of tap water. The $T^2{}_1$ and $T^2{}_2$ relaxation times in the intrabead compartment were 0.39 sec and 0.032 sec, respectively. These values were calculated assuming a $T_1 = 0.604$ sec and $T_2 = 0.057$ sec for the entire sample which corresponds to measurements of the G-25 gel in Table 4.1.

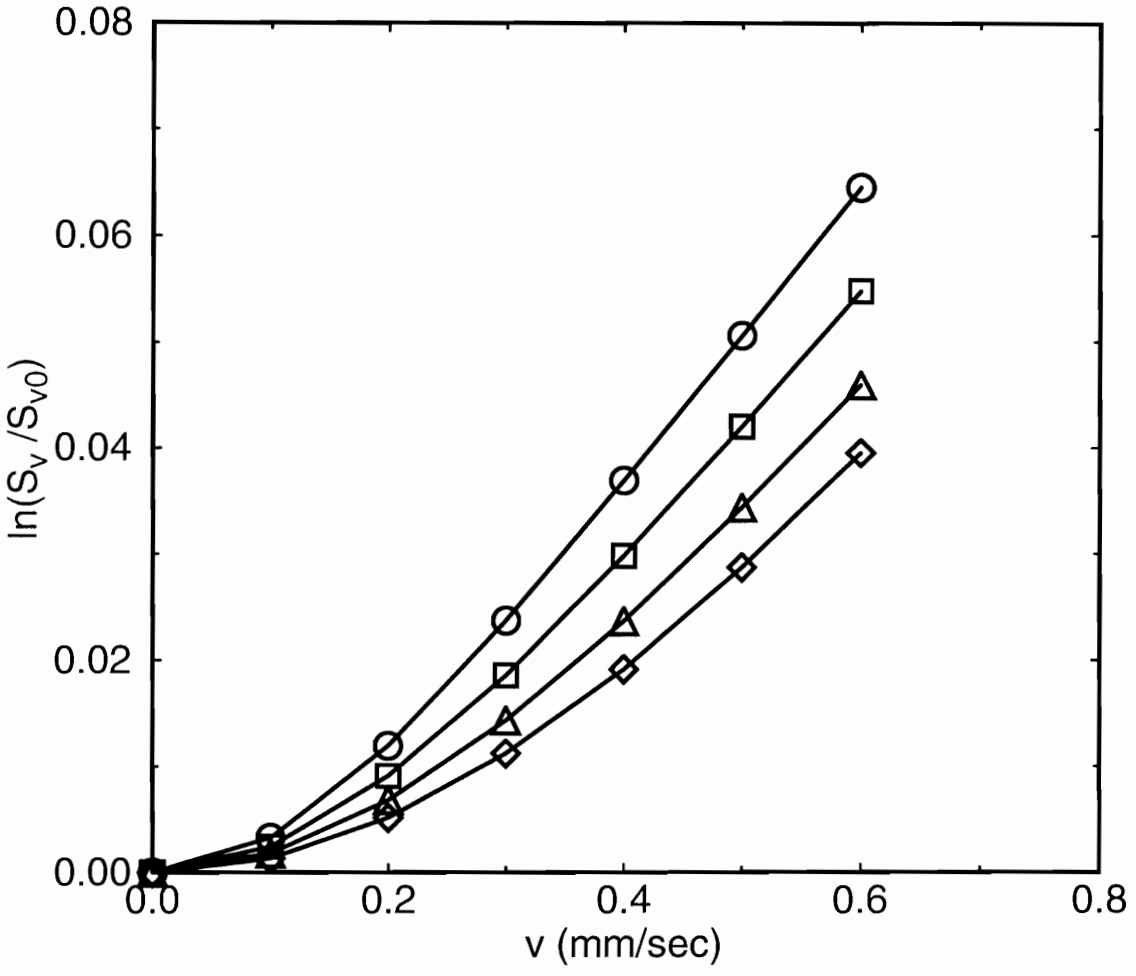

Fig. 4.6 Three-compartment model computer simulations. The natural logarithm of the integrated MRI signal intensity normalized to the calculation at a flow velocity $V = 0$ is plotted as a function of flow for exchange rates: $K_1 = 0$ sec^{-1} ($K_2 = 0$ sec^{-1}) (circle), $K_1 = 1$ sec^{-1} ($K_2 = 0.909$ sec^{-1}) (square), $K_1 = 2$ sec^{-1} ($K_2 = 1.82$ sec^{-1}) (triangle), $K_1 = 3$ sec^{-1} ($K_2 = 2.73$ sec^{-1}) (diamond). The simulations assumed $\beta = 1.1$, $\beta_1 = 6.11$, $K_3 = 0.4$ sec^{-1} ($K_4 = 2.22$ sec^{-1}), and $K_5 = 10.$ sec^{-1} ($K_6 = 61.11$ sec^{-1}). The $T^1{}_1$, $T^1{}_2$, $T^2{}_1$, and $T^2{}_2$ relaxation times in the extrabead and intrabead compartments were all equal to 2.0 s, simulating that of tap water. The $T^3{}_1$ and $T^3{}_2$ relaxation times in the immobile water compartment were calculated to be 66 ms and 4.6 ms, respectively. These values were calculated assuming a $T_1 = 0.604$ sec and $T_2 = 0.057$ sec for the entire sample, which corresponds to measurements of the G-25 gel in Table 4.1.

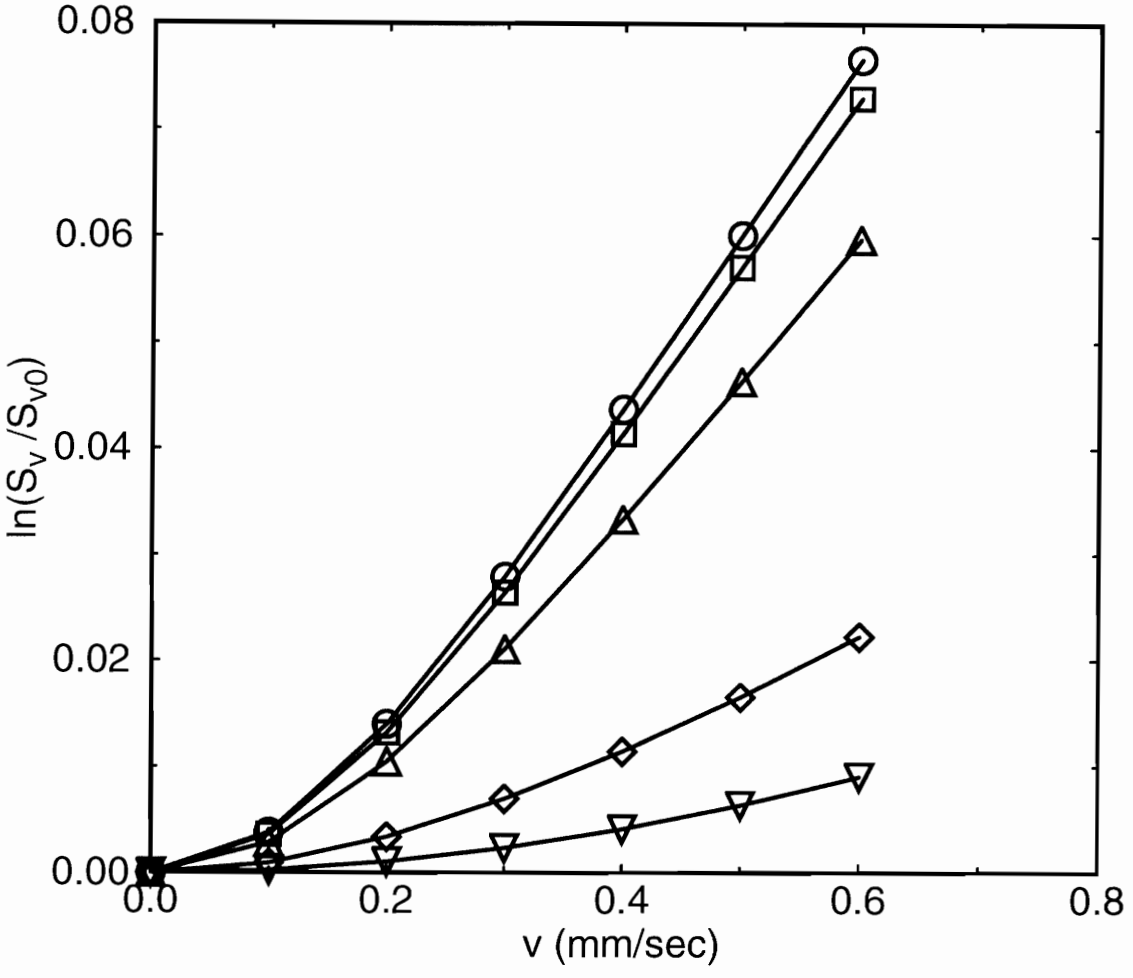

Fig. 4.7 Three-compartment model computer simulations. The natural logarithm of the integrated MRI signal intensity normalized to the calculation at a flow velocity $V = 0$ is plotted as a function of flow for exchange rates: $K_5 = 8$ sec^{-1} ($K_6 = 48.89$ sec^{-1}) (circle), $K_5 = 9$ sec^{-1} ($K_6 = 55.0$ sec^{-1}) (square), $K_5 = 10$ sec^{-1} ($K_6 = 61.11$ sec^{-1}) (triangle up), $K_5 = 11$ sec^{-1} ($K_6 = 67.22$ sec^{-1}) (diamond), $K_5 = 12$ sec^{-1} ($K_6 = 73.33$ sec^{-1}) (triangle down). The simulations assumed that $K_1 = 0.4$ sec^{-1} ($K_2 = 0.36$ sec^{-1}) and $K_3 = 0.4$ sec^{-1} ($K_4 = 2.22$ sec^{-1}). The relaxation times, the volume ratio β, and the volume ratio β_1 were the same as those used for the simulations in Fig. 4.6, based upon a G-25 gel.

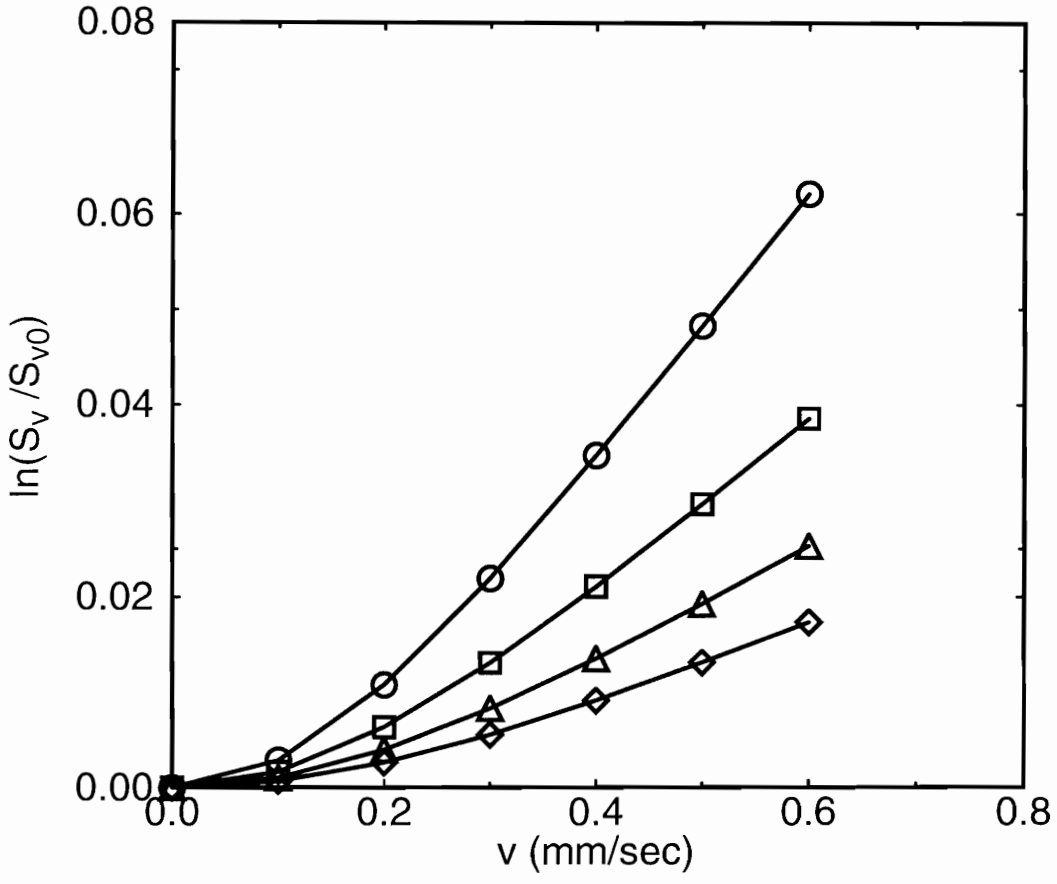

Fig. 4.8 Three-compartment model computer simulation. The natural logarithm of the integrated MRI signal intensity normalized to the calculation at a flow velocity $V = 0$ is plotted as a function of flow for volume ratios $\beta_{physical} = 1.5$ (circle), $\beta_{physical} = 2.0$ (square), $\beta_{physical} = 2.5$ (triangle), $\beta_{physical} = 3.0$ (diamond), where it was assumed that $\beta_1 = 6.11$, $K_1 = 1.\ sec^{-1}$, $K_3 = 0.8\ sec^{-1}$, $K_5 = 0.8\ sec^{-1}$, and $T^3{}_1$ and $T^3{}_2$ were calculated using Eqs. (4.35)-(4.36); The $T^1{}_1$, $T^1{}_2$, $T^2{}_1$, and $T^2{}_2$ relaxation times in the extrabead and intrabead compartments were all equal to 2.0 s, simulating that of tap water. The relaxation times for immobile water were calculated assuming a $T_1 = 0.604$ sec and $T_2 = 0.057$ sec for the entire sample, which corresponds to measurements of the G-25 gel in Table 4.1.

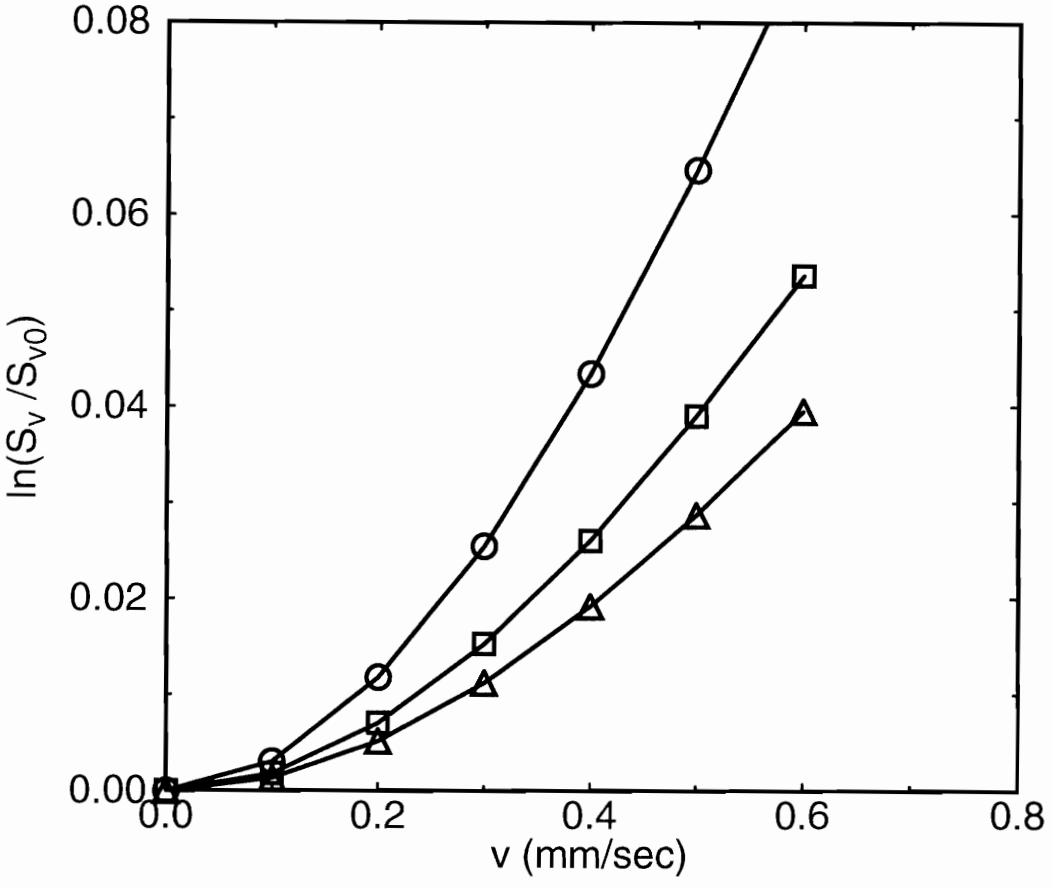

Fig. 4.9 Slice thickness dependence of the normalized MRI signal from the three-compartment model. Slice thickness was: 1. mm (circle), 2. mm (square), 3. mm (triangle). The other parameters were same as those used in Fig 4.6 when $K_1 = 3$.

Figure 4.6 shows the effect of the rate of exchange between the extrabead compartment and the intrabead compartment on the normalized MRI signal intensity. The T^1_1, T^1_2, T^2_1, and T^2_2 relaxation times in the extrabead and the intrabead free water compartments were set to values of 2.0 s and the $T^3_1 = 66$ ms and $T^3_2 = 4.6$ ms for the immobile water compartment were calculated using Eqs. (4.35) and (4.36) and assuming a $T_1 = 0.604$ sec and a $T_2 = 0.057$ sec for the entire sample, which corresponds to measurements of the G-25 gel in Table 4.1. The intrabead to immobile water volume ratio β_1 was calculated as 6.11 using Eq. (4.24) and assuming an intrabead to extrabead volume ratio of $\beta = 1.1$. Compared with Fig. 4.5, the separation between the curves for the three-compartment model seem to be more evenly distributed than for the two-compartment model for the specific parameters used in these simulations.

Figure 4.7 shows the effect of exchange between free water in the intrabead compartment and bound water in the immobile water compartment on the normalized MRI signal intensity. The simulations assumed that $K_1 = 0.4$ sec^{-1} ($K_2 = 0.36$ sec^{-1}) and $K_3 = 0.4$ sec^{-1} ($K_4 = 2.22$ sec^{-1}). The relaxation times, the volume ratio β, and the volume ratio β_1 were the same as those for the simulations in Fig. 4.6, based upon measurements of a G-25 gel. The curves show that the normalized MRI signal decreases with an increase in the rate of exchange between free water in the intrabead compartment and bound water in the immobile water compartment. Notice the large separation between the curves for $K_5 = 10$ and $K_5 = 11$

Figure 4.8 shows the effect of the ratio of the physical intrabead volume to the physical extrabead volume $\beta_{physical}$ on the normalized MRI signal intensity. Plots are shown for $\beta_{physical} = 1.5$, 2.0, 2.5, and 3.0. The T^1_1, T^1_2, T^2_1, and T^2_2 relaxation times in the extrabead and intrabead compartments were all equal to 2.0 s, simulating that of tap water. In the simulations the following parameters were fixed to $\beta_1 = 6.11$, $K_1 = 1.0$ sec^{-1}, $K_3 = 0.8$ sec^{-1}, $K_5 = 0.8$ sec^{-1}. For each $\beta_{physical}$ value, the exchange rate constants K_2, K_4, and K_6 were calculated using Eqs. (4.30)-(4.32), β was

calculated using Eq. (4.24)-(4.25), and the relaxation times T^3_1 and T^3_2 for immobile water were calculated using Eq. (4.35)-(4.36) assuming a $T_1 = 0.604$ sec and $T_2 = 0.057$ sec for the entire sample, which corresponds to measurements of the G-25 gel. Results show that when $\beta_{physical}$ increases (flow compartment volume decreases) the signal is attenuated due to fewer spins flowing into the slice bring with them refreshed magnetization. Notice that by increasing $\beta_{physical}$ the volume of the immobile water compartment increases, and the T^3_1 and T^3_2 increase in order that the total sample T_1 and T_2 can remain constant. This offsets somewhat the decrease in signal that would be expected if the T^3_1 and T^3_2 had remained constant and the sample T_1 and T_2 had decreased.

Figure 4.9 shows the dependence of the normalized MRI signal on slice thickness. The parameters used in the simulation were the same as those used in Fig. 4.6 for the simulation with $K_1 = 3$. Even though flow was very slow relative to the thickness of the slice, the results show that the normalized MRI signal is sensitive to slice thickness. The results show that as the slice thickness decreases the amplitude of the normalized signal increases.

4.4.3 Chromatography Gel Phantom Experiments

Figure 4.10 shows transaxial spin echo images of the G-25 and G-50 chromatography columns for different mean flow velocities. For each flow rate five images were acquired. The average signal over a region of interest within each column was calculated and normalized to the signal at zero flow. Then the mean and variance of the five normalized values were calculated and the natural logarithm was plotted in Figs. 4.11 and 4.12 as a function of mean flow velocity. The mean flow velocities ranged from zero to 0.66 mm/sec. Exchange between Sephadex beads of a larger exchange rate constant (G-50 greater than G-25) results in a greater MRI signal loss, which agrees with the computer simulations for the two-compartment and the three-compartment models shown in Figs. 4.5 and 4.6.

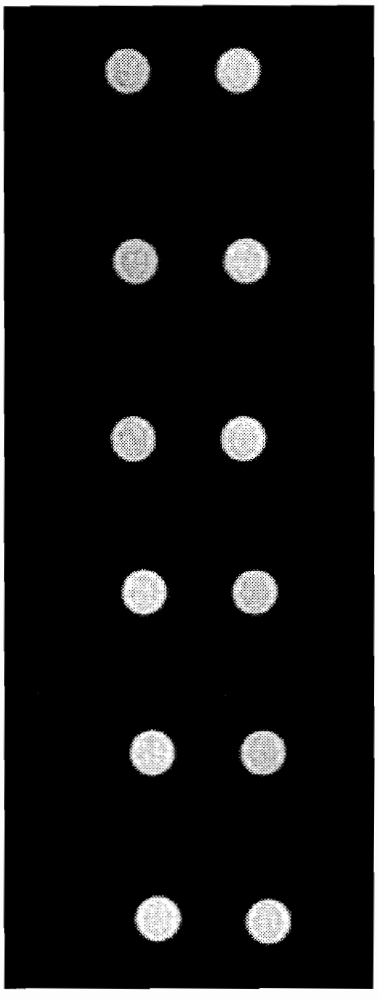

Fig. 4.10 Transaxial spin echo images of the Sephadex G-25 column on the left and the Sephadex G-50 column on right. The mean flow velocity for the G-25 column is 0.0, 0.11, 0.22, 0.36, 0.51, and 0.66 mm/sec from top to bottom. The mean flow velocity for the G-50 column is 0.0, 0.1, 0.2 0.3, 0.53, 0.65 mm/sec.

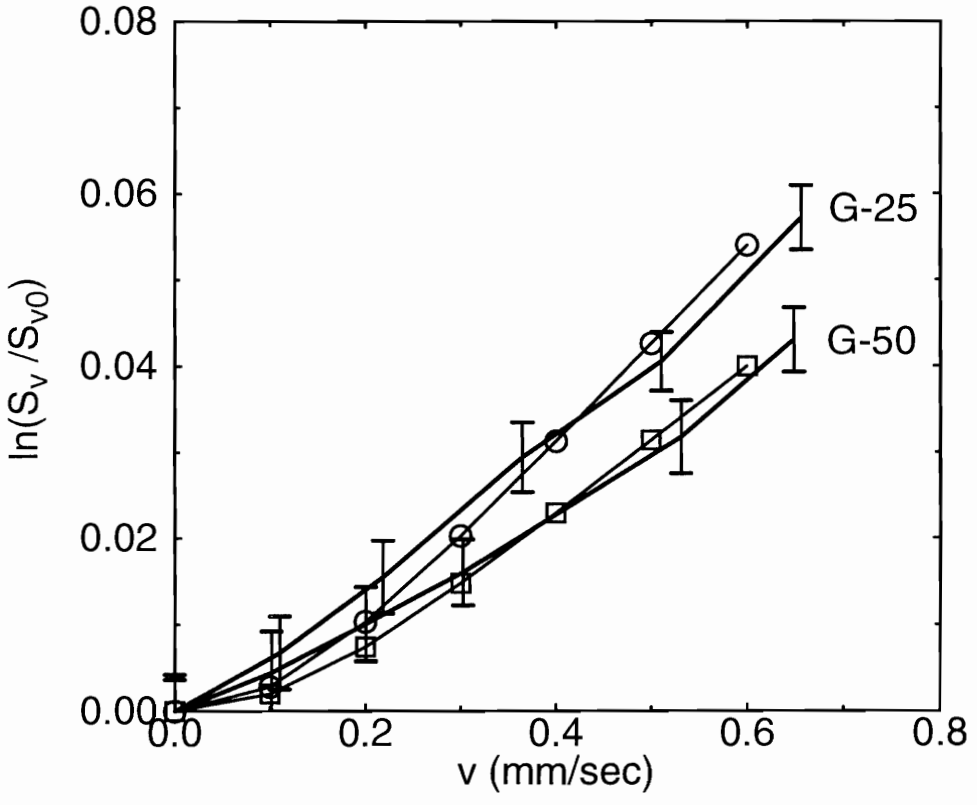

Fig. 4.11 Comparison of experimental results with a two-compartment simulation. The natural logarithm of the measured MRI signal intensity normalized to the measurement at a flow velocity $V = 0$ is plotted as a function of flow for the G-25 and G-50 columns. The measurements were obtained by averaging the signal within a circular region of interest (about 16 pixels) of the appropriate column section illustrated in Fig. 10 and normalizing to the average signal at zero flow. The results from a two-compartment model simulation are superimposed upon the experimental results. The curve superimposed on the G-25 experimental data was generated using $K_1 = 0.4 \ \text{sec}^{-1}$ ($K_2 = 0.313 \ \text{sec}^{-1}$) and the curve superimposed on the G-50 experimental data were generated using $K_1 = 0.8 \ \text{sec}^{-1}$ ($K_2 = 0.625 \ \text{sec}^{-1}$). In the simulations it was assumed that $\beta = 1.28$. The $T^1{}_1$ and $T^1{}_2$ relaxation times in the extrabead compartments were equal to 2.0 s. The $T^2{}_1$ and $T^2{}_2$ relaxation times in the intrabead compartment were 390 ms and 32 ms for the G-25 gel. The $T^2{}_1$ and $T^2{}_2$ relaxation times in the intrabead compartment were 416 ms and 283 ms for the G-50 gel.

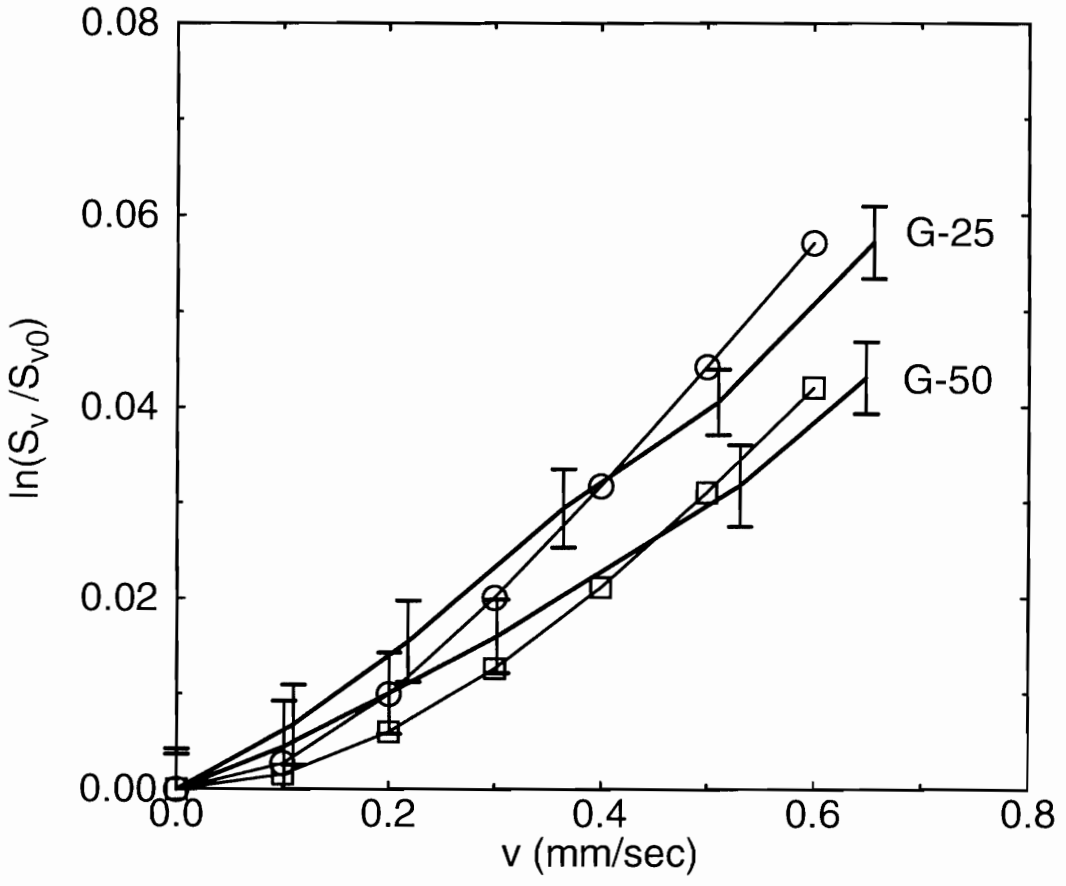

Fig. 4.12 Comparison of the same experimental results given in Fig. 11 with a three-compartment simulation. The results from a three-compartment model simulation are superimposed upon the experimental results. The curve superimposed on the G-25 experimental data was generated using $K_1 = 0.4\ \text{sec}^{-1}$ ($K_2 = 0.363\ \text{sec}^{-1}$), $K_3 = 0.4\ \text{sec}^{-1}$ ($K_4 = 2.22\ \text{sec}^{-1}$), and $K_5 = 10.1\ \text{sec}^{-1}$ ($K_6 = 61.72\ \text{sec}^{-1}$). The curve superimposed on the G-50 experimental data was generated using $K_1 = 0.8\ \text{sec}^{-1}$ ($K_2 = 0.727\ \text{sec}^{-1}$), $K_3 = 0.8\ \text{sec}^{-1}$ ($K_4 = 4.44\ \text{sec}^{-1}$), and $K_5 = 3.2\ \text{sec}^{-1}$ ($K_6 = 19.56\ \text{sec}^{-1}$). In the simulations it was assumed that $\beta = 1.1$ and $\beta_1 = 6.11$ for both gels. The $T^1{}_1$, $T^1{}_2$, $T^2{}_1$, and $T^2{}_2$ relaxation times for the extrabead and intrabead compartments were equal to 2.0 s. The $T^3{}_1$ and $T^3{}_2$ relaxation times in the immobile water compartment were 66 ms and 4.6 ms for the G-25 gel and 71 ms and 45 ms for the G-50 gel.

The results of a two-compartment model simulation are superimposed upon the experimental results in Fig. 4.11. The curve superimposed on the G-25 experimental data was generated using $K_1 = 0.4\ \text{sec}^{-1}$ ($K_2 = 0.313\ \text{sec}^{-1}$) and the curve superimposed on the G-50 experimental data was generated using $K_1 = 0.8\ \text{sec}^{-1}$ ($K_2 = 0.625\ \text{sec}^{-1}$). The volume ratios and the T_1 and T_2 were chosen as described in Fig. 4.11. The fitting was performed by changing the K_1 value. The difference in the exchange rate constants between the two fits was a factor of two. Notice that the simulated curves fit the experimental data fairly well at the faster flow rates. The fit is not as good for the slower flow rates. We expect that some of this is due to the larger experimental errors at the slower flow rates.

The results of a three-compartment model simulation are superimposed upon the experimental results in Fig. 4.12. The curve superimposed on the G-25 experimental data was generated using $K_1 = 0.4\ \text{sec}^{-1}$ ($K_2 = 0.363\ \text{sec}^{-1}$), $K_3 = 0.4\ \text{sec}^{-1}$ ($K_4 = 2.22\ \text{sec}^{-1}$), and $K_5 = 10.1\ \text{sec}^{-1}$ ($K_6 = 61.72\ \text{sec}^{-1}$). The curve superimposed on the G-50 experimental data was generated using $K_1 = 0.8\ \text{sec}^{-1}$ ($K_2 = 0.727\ \text{sec}^{-1}$), $K_3 = 0.8\ \text{sec}^{-1}$ ($K_4 = 4.44\ \text{sec}^{-1}$), and $K_5 = 3.2\ \text{sec}^{-1}$ ($K_6 = 19.56\ \text{sec}^{-1}$). The K_1 values for G-25 and G-50 gel were chosen based upon the two-compartment fit in Fig. 4.11. The K_3 value was arbitrarily chosen to be equal to K_1. Then the data were fit by changing the value of K_5. Comparing with Fig. 4.11, for these parameters the three-compartment model does not fit the experimental data as well as the two-compartment model in Fig. 4.11.

4.5 Discussion

The modeling of proton exchange between extrabead and intrabead compartments was evaluated using computer simulations and experiments performed on chromatography columns. Two-compartment and three-compartment models were developed to model the exchange processes in Sephadex gels. The computer simulations were compared with experimental results. The computer simulations and experimental

results demonstrated that proton exchange modulates the signal amplitude; however, incorrectly estimating the size of the bound water compartments and the values of T_1 and T_2 for these compartments could mask any sensitivity of signal modulation to exchange processes. The results indicate that both a three-compartment model, which includes extrabead, intrabead, and immobile water compartments, and a two-compartment model of only extrabead and intrabead compartments could be used to model the experimental results. In this work no attempt was made to estimate rate parameters; however, the model approximations of the experimental data are very encouraging and indicate that the next step of this research should investigate the potential of estimating model parameters using nonlinear estimation techniques to fit the complex multiparameter variation of the MRI signal.

The process of exchange of protons between extrabead and intrabead compartments modulates the signal due to a time-of-flight effect. It has been understood for some time that flow in a vessel, even without exchange, can cause the signal in the vessel to vary depending upon the pulse sequence and the flow velocity.[74] As an rf pulse continually excites a slice, in-flowing spins are continually refreshing the slice and saturated spins are continually exiting the slice. Therefore as flow increases, more refreshed spins will enter the slice, thus increasing the signal, and as flow decreases spins are delayed in exiting the slice, saturating the flowing spins and decreasing the signal in the vessel. Likewise, if the additional possibility of exchange between extrabead and intrabead compartments is considered, we see that, as the exchange rate constant increases, spins entering the slice will remain longer within the slice by exchanging with protons in the extrabead compartment, thus increasing the saturation of the spins in both the extrabead and intrabead compartments with repeated pulses and decreasing the total MRI signal. As the exchange rate constant increases, the overall average time spent in the slice increases and the MRI signal becomes more saturated. Therefore the intensity of the

total MRI signal provides a signature whereby exchange rates might be differentiated. Computer simulations and experiments were pursued to study this time-of-flight effect.

Computer simulations were performed for two-compartment and three-compartment models used to describe the exchange of protons between extrabead and intrabead compartments, assuming first-order kinetics. Bloch equations were developed that included flow, diffusion, and exchange between extrabead, intrabead, and immobile water compartments. Finite difference methods were used to solve the Bloch equations of a system of second-order partial differential equations. The development of the system of finite difference equations used to solve the system of second-ordered differential equations was the same as that used in Chapter 3.[60] The finite difference approach required initial conditions to be stated from which the solution is determined at grid points increasing in a single spatial coordinate z and time t. The parabolic portion of the differential equation was approximated by the classic explicit approximation,[60] and all derivatives in z were determined by central difference approximations. The accuracy of the finite difference algorithm is of $O(h^2 + hk^2)$ or $O(h + k^2)$ [60] where h is the grid spacing in t and k is the grid spacing in z. The computation time of the algorithm required about 8 hours on a SUN SPARC 10 workstation to generate the data for Fig. 4.6. The extension of the model to three-dimensional spatial coordinates is approaching feasibility with the improvement in computation speed of new computer hardware.

The experiments were designed so as to isolate as best as possible signal differences due to exchange processes, but it became clear that in order to do this, the differences in T_1 and T_2 properties also had to be considered. The Sephadex G-25 and G-50 gels, each having the same ratio of intrabead to extrabead volumes but different T_1 and T_2 properties, were selected so that signal differences would not be due to different compartment volumes, but would vary due to different exchange rates (with the G-50 gel having a larger exchange rate constant than the G-25 gel due to larger pore size). Water was passed through two chromatography columns, one column packed with the Sephadex

G-50 gel and a second column packed with the G-25 gel. The flow rates were varied in order to analyze the MRI signal intensity within an excited slice of each column as a function of flow velocity. For the G-50 gel the natural logarithm of the signal normalized to the signal at zero flow for all flow velocities was less than the logarithm of the normalized signal for the column with the G-25 gel, indicating that with a larger pore size there is a greater exchange of spins between the various compartments of the slice, thus delaying the exit of the spins from the excited slice and saturating the overall proton signal with repeated rf pulses. What makes this difference even more significant is that it would be expected that the difference would be even greater if the normalized signal for the G-25 gel were not attenuated more than the normalized signal for the G-50 gel because of a much shorter T_2.

A concern was whether signal loss was due to the extra water content in the G-50 gel because of a smaller gel matrix density in its swollen state. Computer simulations were performed using a two-compartment model, comparing $\beta = 1.28$ and $\beta = 1.29$ representing a 0.6 percent volume increase in intrabead compartment. In the simulations $K_1 = 0.8\ \text{sec}^{-1}$ $(K_2 = 0.625\ \text{sec}^{-1})$, the $T^1{}_1$ and $T^1{}_2$ relaxation times in the extrabead compartments were equal to 2.0 s, and the $T^2{}_1$ and $T^2{}_2$ relaxation times in the intrabead compartment were 416 ms and 283 ms based on measurements of the G-50 gel. The results showed that a 0.6 percent increase of water content in the intrabead compartment had an insignificant effect on the signal. The greater effect between the G-25 gel and the G-50 gel was not the small difference in water content but the large differences in T_1 and T_2.

Computer simulations were used to study four additional features in addition to showing that MRI signal loss depends upon the exchange rate constants between extrabead and intrabead compartments: (1) differences between the two-compartment and three-compartment models, (2) signal variation as a function of exchange between free water in the intrabead compartment and bound water in the immobile water compartment,

(3) signal variation as a function of intrabead to extrabead volume ratios, and (4) signal variation as a function of slice thickness.

Computer simulations in Fig. 4.6 indicated that a three-compartment model more evenly distributed the normalized signal-versus-flow velocity curves for increasing exchange rate constants for the particular parameters simulated. It was found that the separation between the curves for a rate constant $K_1 = 1$ and $K_1 = 2$ sec^{-1} was about the same as between a rate constant $K_1 = 2$ and $K_1 = 3$ sec^{-1} for a three-compartment model, whereas the separation between the first pair of curves was about twice the separation between the second pair of curves for a two-compartment model. This is due to the fact that the rate of exchange ($K_5 = 10$ sec^{-1}) between free and immobile water somewhat dampens the differences between the curves of different rates of exchange between the extrabead and intrabead compartments for the particular parameters simulated. On the other hand, we have observed that a shorter T_1 in the immobile water compartment for the same exchange rate constant K_5 between free and immobile water results in greater separation between the curves for different exchange rate constants K_1. This illustrates the flexibility of models with more than two-compartments and their ability to model various rates of exchange between many potentially different water compartments. The physical properties of a chromatography gel phantom would suggest that a three-compartment model that includes an immobile water compartment would better model the kinetics of the physical gel system. In fact, it is expected that water protons bound to the gel matrix dominate the T_1 and T_2 decay of the MRI signal. However, this does not imply that a three-compartment model would be easier than a two-compartment model to fit to experimental data.

Computer simulations studied the effect of the immobile water compartment, showing in Fig. 4.7 that the normalized MRI signal decreases with an increase in the rate of exchange between free and immobile water. Also, notice that the effect is not necessarily linear, nor does the rate of change necessarily increase monotonically, as

shown with the considerable increase in separation between the curves for $K_5 = 10$ and $K_5 = 11$ and then a decrease in the separation with increasing K_5. Independent of whether the spins are in the intrabead or extrabead compartment, they are constantly exchanging with the immobile water compartment, resulting, on average, in further delays in exiting the excited slice, even though this exchange may be fast. We attempted to measure the exchange rate constant K_5 [$K_5 = 1/T_{1\,sat}(1 - M^0{}_{sat}/M^0)$] between mobile and immobile water using magnetization transfer techniques.[65] The experiments were not successful because $T_{1\,sat}$ could not be measured accurately without a second independent rf channel that could maintain a constant saturation using an off resonance rf pulse. Also, note that in order for this to work, the T_1 of the mobile water compartment must be of the same order as K_5 ($1/T_{1\,sat} = 1/T_1 + K_5$). In tissue K_5 can range between 1 and 3 sec^{-1}.[65] (Note that in the simulations we typically used values of $K_5 = 10$.)

Computer simulations in Fig. 4.8 showed that decreasing $\beta_{physical}$ (thus increasing the volume of the flow compartment) extends the range of the curves by increasing the time-of-flight effect. The extrabead volume size significantly affects the amplitude of the normalized MRI signal intensity. With a flow fraction of 22% for the lowest curve in the simulation in Fig. 4.8, the simulations were still far from representing a volume fraction of 10% for biological tissue. However, the signal not only is a function of volume fraction, which determines the contribution from each compartment to the entire sample (voxel), but also depends upon the relaxation times for each compartment. In our simulations in Fig. 4.8, we varied $\beta_{physical}$ but kept the overall T_1 and T_2 constant and equal to the measured values. Thus, increasing $\beta_{physical}$ while keeping β_1 a constant results in an increase in volume fraction for the immobile water compartment. This causes the relaxation times for the immobile water compartment to be a bit longer, which causes the extrabead free water and intrabead free water to relax more slowly through exchange, thus compensating for the signal loss due to a smaller flow compartment volume. The signal decrease for the overall signal we observed in Fig. 4.8 by increasing $\beta_{physical}$ indicates

that the decrease of the flow compartment volume is a major factor for this signal loss. Suppose instead, T_1 and T_2 in the immobile water compartment and $\beta_{physical}$ remain constant, and the overall T_1 and T_2 is allowed to vary. By decreasing the intrabead free water compartment volume and increasing the immobile water compartment volume, it is expected that the signal will decrease because a larger immobile water compartment causes more spins involved in the exchange between free water and immobile water. On average, spins will spend more time within the slice, thus becoming more saturated.

The slice thickness has a significant effect upon the signal-versus-flow curves because the perfusion model is based upon a time-of-flight effect. The dynamic range in the signal-versus-flow curves increases with a decrease in slice thickness, whereas the overall curve becomes more attenuated with increase in slice thickness. Also, the incremental change in the attenuation becomes less with increase in slice thickness. A smaller slice thickness would be desired to resolve smaller differences between exchange rate constants. However, there is a trade-off in the signal-to-noise ratio, which was not analyzed in our simulations; the signal-to-noise is expected to decrease with a decrease in slice thickness.[75]

For the Sephadex G-25 and G-50 gel phantoms, exchange between extrabead and intrabead occurs when, due to molecular thermodynamic motion, water protons pass through the pores. The exchange rate constant is proportional to the area of the pore on the gel bead surface, mean velocity of the protons, and the proton density. Since a G-50 gel has a pore size almost double that of the G-25 gel, it was expected that the exchange rate constant for G-50 would be approximately double that of the G-25 gel. This is what we found in Fig. 4.11, with simulated curves corresponding to $K_1 = 0.4$ for G-25 and $K_1 = 0.8$ for G-50 in close comparison with the experimental data. The pore size and the average number of pores per bead (each bead of approximately 100 μm diameter) could not be obtained from the gel manufacturer, which would have helped to estimate the exchange rate constant. Instead, the manufacturer provides the permeability of the gel to

describe the property of exchange. The permeability of a gel is not expressed in terms of the permeability of each bead, but in terms of the permeability through a layer of material. The ratio of the permeability of G-50 to the permeability of G-25 is $k\,(\text{G-50})\,/\,k\,(\text{G-25}) = 1450/800 = 1.81$.[72] The reason that the permeability for G-50 is not exactly double the value of that for G-25 is because of the slight deformation that occurs during the packing caused by the reduced gel material in the G-50 gel. The velocity (cm/sec) of the solvent with a viscosity η through the gel layer is proportional to the permeability and is given by the common expression $V = k\,(\text{permeability})\,P\,(\text{pressure})\,/\,[\eta\,(\text{viscosity})\,L\,(\text{length of Sephadex packing})]$.[72]

There has been significant work using NMR to study properties of porous media (see special issue of Magnetic Resonance Imaging[76]). Most of this work has been concerned with studying the T_1, T_2 and diffusion properties of the media. One paper[77] in this issue discussed the fluid dynamic properties of porous media. However, most of the work treats the porous media as a whole, arriving at T_1, T_2 and diffusion coefficients for the total sample. Our approach has been different in that the sample is divided into separate compartments and the properties are specified for each. In following this approach, it is recognized that the estimation of the physical constants becomes more complex.

It can be a difficult task to obtain a phantom that simulates perfusion in biological tissue. Biological tissues are complex and heterogeneous in nature; consequently, their NMR properties depend upon many factors.[71] Proton MRI phantoms have been made of agarose, hydrogel, and acrylamide gels, which have been shown to be more tissue-like in terms of T_1 and T_2 properties than simple aqueous solutions.[67] The gel concentration determines the T_2 of the material and the paramagnetic concentration determines the T_1.[71] Our desire was not so much to match the T_1 and T_2 characteristics of tissue but more to study the exchange process, which would mimic the exchange between the intravascular and extravascular compartments of biological tissue. In the search for a gel type phantom,

it was not necessarily easy to find gels of the same size with different pore sizes. In most cases, if two gels had different pore sizes, they also had different bead sizes.

The extrapolation of our results to biological tissue must consider the significant differences between the extrabead volume in the gels used in the experiments and the intravascular blood volume found in biological tissue. The simulations were performed with T_1 and T_2 values similar to that of tissue and flow similar to that of slow flowing capillaries, but the 40% extrabead volume fraction was considerably larger than the 10% or lower intravascular volume fraction expected in biological tissue. For tissue with a slow flow of 0.6 mm/sec, it would be expected that the dynamic range would be two orders of magnitude less than the dynamic range obtained in the computer simulations and experiments. However, instead of relying on tagging tissue directly, perfusion experiments in animals[78,79] and humans[80] have relied more upon bolus tracking techniques to tag tissue with an in-flow velocity as larger as 80 cm/sec. This fast in-flow gives a "blush" to the MR image of the tissue that can be measured and could potentially be fit to compartment models.

Because biological tissue is complex, it becomes a difficult task to estimate all potential kinetic parameters. The multicompartment perfusion model works well to demonstrate the modulation of the MRI signal by exchange between compartments. However, the exchange rate constants and volume ratios are embedded in a milieu of several other parameters that affect the NMR signal of biological tissue. Although it is possible in principle to fit the measured signal intensity to these parameters using nonlinear estimation techniques, until now this still remains a challenging task. It may be that a two-compartment model will be easier than a three-compartment model to fit to experimental biological data. To estimate model parameters in practice, it would be useful to utilize methods that isolate parametric effects. For example, magnetization transfer techniques may be useful to obtain the mobile and immobile water exchange. Also, it would be useful when estimating compartment model parameters to remove the coupling

between the compartments, which prevents solving the system of differential equations analytically. This might be done by designing a specific pulse sequence. We emphasize that in applying compartment modeling *in vivo*, parameter estimates cannot be derived by varying flow. In fact, we expect that independent measurements of flow will have to be made in order to estimate exchange rate constants.

A simplification of the compartment models investigated in this paper can be obtained using constant infusion techniques. This approach is used many times in nuclear medicine experiments and has recently been used in MRI.[78,79] The approach uses a tag that is constantly infused into the area of interest and assumes that the partition coefficient (ratio of concentration in the tissue to concentration in the blood) is known at equilibrium. The tag could be a radioisotope or spins saturated by a pulse applied externally to the area of interest. This approach has recently been applied in MRI to measure tissue perfusion in rats.[78,79] The spins are continuously excited in a slice or region of the carotid arteries that flow into a region of interest in the brain. The excitation is accomplished using an rf channel and coil separate from that used to image the region of interest. Magnetization transfer is used to suppress signal variations that depend upon the immobile water compartment. In a recent abstract,[80] our model was used to show that the signal contrast used in calculating the perfusion depends upon the flow velocity.

In summary, we have performed experiments to verify the application of a multi-compartment model to represent perfusion in a chromatography gel phantom. We have demonstrated that the exchange between the compartments does modulate the MRI signal intensity. We feel that the results show promise for the use of compartment modeling of endogenous protons to better understand tissue perfusion.

CHAPTER 5

APPLICATION OF MULTICOMPARTMENT PERFUSION MODEL TO HUMAN USING ARTERIAL TAGGING OF ENDOGENOUS PROTONS AND MAGNETIZATION TRANSFER TECHNIQUES

5.1 Introduction

In general a multicompartment model has to be used to describe tissue perfusion and differential equations associated with this model are not solvable analytically. In practice there is a need for simplification of the compartment models. In the last Chapter we have discussed the possibility of tagging flowing spins external to the tissue area to study tissue perfusion instead of relying on tagging tissue directly. These tagged flowing spins can be used as information to estimate parameters of a multicompartment tissue perfusion model as the one described in Eqs. (4.5)-(4.8). More importantly people gave attention to this technique simply because they expected that the coupling between compartments can be removed by using a pulse labelling sequence. In using a tagging technique the in-flow velocity has to be very fast such that those tagged spins can form a "blush" of the tissue area where perfusion occurs before the spins relax. From intuition one would expect the MRI signal contrast with and without using arterial spin labeling technique should be flow velocity dependent. It means that in applying compartment modeling *in vivo*, parameter estimates from the signal contrast cannot be derived without knowing the information of flow velocity.

Recently, this arterial spin labeling technique has been used in MRI to measure tissue perfusion in rats.[78,79] It was reported that perfusion can be measured quantitatively

based upon the assumptions that the tagged flowing spins flush into the different tissue areas (voxels) with the same flow velocity and this velocity is fast enough without the need of considering relaxations during the time tagged spins travel from the tagging position to the tissue. This caused us to wonder whether these assumptions were made correctly.

Another mechanism that causes coupling of differential equations in tissue perfusion compartmentization is due to exchange of magnetization between compartments. The effect of magnetization transfer between free water and immobile water in tissue on MRI contrast have been studied and verified by Balaban et al.[65] In their study a saturation transfer method was applied to saturate spins in the immobile water compartment such that parameters such as exchange rate constant and apparent relaxation times associated only with the free water are isolated. This simplifies the model in which only one differential equation corresponding to tissue compartment is considered.

In this chapter, we first introduce the saturation transfer method to study magnetization transfer and show the experimental results using this method on dog kidney tissue. Based upon the understanding of the magnetization transfer effect in tissue on MRI contrast we then give a description of a perfusion model for arterial labelling technique to measure tissue perfusion quantitatively.[78,79] Finally, we use our multicompartment tissue perfusion model to study the external labelling technique and to determine the signal contrast expected for various flow velocities of blood flowing into a selected tissue slice by both computer simulations and experiments on human brain.

5.2 Magnetization Transfer Contrast (MTC) and Tissue Water Proton Relaxation Measurement on Dog Kidney

In conventional MRI imaging the contrast of biological tissue is based upon water T_1/T_2 relaxation properties. The variations in water relaxation rates generate image contrast between different tissues and pathologies depending on how the MR image is collected. For a number of years another relaxation mechanism in biological tissue was

extensively studied.[81-86] This relaxation is related to cross-relaxation and/or chemical exchange between free water protons and protons associated with macromolecules or immobile water. Since the relaxation of immobile water dominates the T_1 and T_2 relaxation times, the rate of exchange between free and immobile water becomes an important factor in the relaxation process.[65]

5.2.1 The Saturation Transfer Method

In this study we used the saturation transfer method to measure the rate of magnetization exchange between spins in free water and spins in immobile water. This method originally described by Forsen and Hoffman[87] in which the rate of magnetization exchange between two pools can be quantitatively determined. Saturation transfer technique uses a constant selective irradiation, with radiofrequency energy of one member of an exchange pair of spins, and observe the effect of this irradiation on its nonirradiated exchange partner. If exchange exists, it is expected to see a decrease in the steady-state magnetization and a decrease in the observed T_1 of the nonirradiated spins. Since the immobile water magnetization has a wide spectrum of frequencies, Wolff and Balaban[65] used the saturation transfer method on biological tissue with an off-resonance frequency with respect to free water resonance frequency for irradiation.

The exchange of magnetization is illustrated in Fig. 5.1. The pseudo-first-order rate constant of exchange from free water to immobile water is denoted by k and k' is the rate constant of magnetization transfer from immobile water to free water. We can write the Bloch equation for the free water pool as

$$\frac{\partial M}{\partial t} = -\frac{M - M_0}{T_1} - kM + k'M_{\text{immobile}}. \tag{5.1}$$

If the off-resonance irradiation is long enough the magnetization in the immobile water pool will be totally saturated. Thus Eq. (5.1) becomes

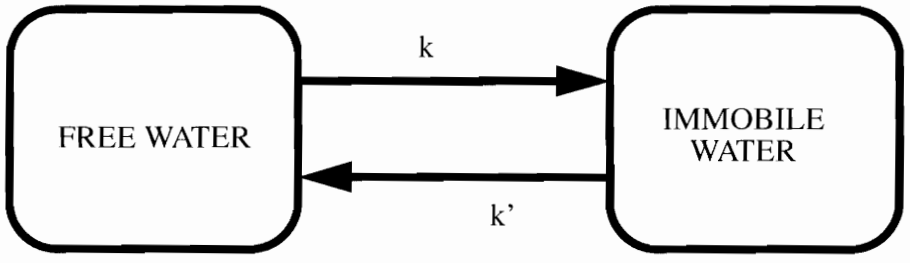

Fig. 5.1 Simple two-compartment model consisting of a free water and immobile water compartment with two-way exchange. The pseudo-first-order rate constant of exchange from free water to immobile water is denoted by k and k' is the rate constant of magnetization transfer from immobile water to free water.

$$\frac{\partial M}{\partial t} = -\frac{M - M_0}{T_1} - kM. \tag{5.2}$$

A new relaxation time $T_{1\,\mathrm{sat}}$ for the tissue magnetization M is

$$1/T_{1\,\mathrm{sat}} = 1/T_1 + k. \tag{5.3}$$

At new steady-state (Eq. (5.2) equals zero), using Eqs. (5.2) and (5.3) we can calculate the exchange rate constant k by

$$k = \frac{1}{T_{1\,\mathrm{sat}}}\left(1 - \frac{M_{\mathrm{sat}}}{M_0}\right). \tag{5.4}$$

5.2.2 Magnetization Transfer Experiment on a Dog Kidney

5.2.2.1 Materials and Methods

A sample of dog kidney tissue (immersed in D_2O solution) was placed in a 4.7 T IBM MR 200 spectrometer. D_2O solution was used to reduce the water density that decreases signal to match the small signal level allowed by the signal receiving hardware. After putting the sample of dog kidney tissue into a tube containing D_2O solution the tube was sealed and seated for more than 4 hours waiting for the equilibrium of water density inside the tissue. Experiments were performed using saturation transfer method by irradiating the immobile water pool with a constant off-resonance rf pulse. The off-resonance frequency used for irradiation pulse was selected between 5-50 kHz. It was assumed that when the off-resonance frequency is greater than 5 kHz we can consider the off-resonance pulse is selective for immobile water spins since the immobile water spins would have an NMR linewidth much greater than that for free water. Both high- and low-power irradiation pulses were used to study the effect of power dependence of the free water signal intensity after the off-resonance irradiation. It was observed that high power off-resonance irradiation pulse generated greater saturation in magnetization magnitude at

free water resonance frequency after irradiation. In experiments we used an rf power corresponding to the rf power control parameter DP=1 L, which produced a 16% decrease in the magnitude of the water resonance for a irradiation at a frequency 50 kHz below the water resonance frequency.

First a 90° pulse was used at water resonance to collect FID signals. M_0 was obtained by measuring the magnitude at peak for the spectrum generated from FID signals. Then we used a pulse sequence consisting of a constant off-resonance pulse for 4 s followed by a 90° pulse at water resonance for obtaining FID signals after irradiation. M_{sat} was measured in the same way as to measure M_0. In experiments T_{1sat} was measured using the same irradiation pulse combined with an inversion recovery pulse sequence.

Different off-resonance frequencies from -5 to -50 kHz were used to study the frequency dependency of the signal M_{sat}. The exchange rate constant k was calculated according to Eq. (5.4).

5.2.2.2 Results

The results of the saturation transfer experiments on dog kidney are shown in Table 5.1. The first column in the table is the off-resonance frequency used in experiments. The next columns list values for T_{1sat}, M_{sat}/M_0, and k, respectively. Results showed that applying an off-resonance irradiation on dog kidney tissue does generate signal saturation which proves the existence of the exchange between the free water pool and the immobile water pool in tissues. It is also found that T_{1sat} and M_{sat}/M_0 are sensitive to the off-resonance frequency, so is the calculated k. Results show that when the magnitude of the off-resonance frequency decreases a larger saturation appears such that the value of the calculated rate constant increases.

Table 5.1 Effect of ^1H_f saturation for a dog kidney tissue *in vitro*.

Frequency (kHz)	T_{1sat} (s)	M_s/M_0	K (s^{-1})
-50	15.04	0.84	0.011
-30	14.5	0.73	0.018
-10	12.13	0.46	0.045
-5	11.52	0.44	0.049

5.2.2.3 Discussion

In the experiments, a very long T_{1sat} was measured for the dog kidney tissue immersed in D_2O solution. It is believed that this is a result of a much longer correlation time caused by large population of D_2O molecules surrounding a single water molecule. Since the water density inside dog kidney tissue had been changed the value of measured T_{1sat} did not reflect the true value of T_{1sat} for dog kidney tissue. Thus the accuracy of calculated exchange rate constant k was negatively influenced by incorrect T_{1sat} measured using D_2O solution. In fact the values of calculated k listed in Table 5.1 is much smaller than the value reported for a rat kidney.[65] This problem could have been avoided by using an MR imager with a second rf channel. The water signal would not have had to be attenuated using a D_2O solution.

Despite the accuracy of the measured exchange rate constant, the experiments tell us that the saturation of the immobile water pool using preirradiation pulse results in a signal attenuation of free water due to the exchange between free and immobile water. This attenuation of the signal is power and frequency dependent. MRI contrast (directly related to magnetization contrast) will increase with increasing preirradiation pulse power or decreasing off-resonance frequency.

It is anticipated that in a tissue perfusion study, one has to consider the exchange between free water and immobile water. This is due to the fact that biological tissue consists of a fair amount of immobile water due to the existence of cell membranes and less mobile water protons in proteins.

5.3 A Perfusion Model Using Spin Labeling of Arterial Water

Constant infusion techniques are useful for perfusion studies. This approach is used many times in nuclear medicine experiments and has recently been used in MRI by Detre et al.[78] and Zhang et al.[79] The approach uses a tag that is constantly infused into the area of interest and assumes that the partition coefficient (ratio of concentration in the tissue to concentration in the blood) is known at equilibrium. In nuclear medicine the tag

could be a radioisotope and in MRI the tag could be spins saturated by a pulse applied externally to the area of interest. Due to the large concentration of water in blood, it is advantageous to use endogenous water as a tracer for tissue perfusion measurement noninvasively.

The Bloch equation for tissue magnetization along longitudinal direction, which includes T_1 relaxation, tissue perfusion, and cross-relaxation between tissue water and immobile water, can be written as[79]

$$\frac{dM}{dt} = \frac{M^0 - M}{T_1} - k_{for}M + k_{rev}M_{immobile} + pM_a - pM_v, \tag{5.5}$$

where

p = tissue perfusion rate in ml $g^{-1}s^{-1}$,

T_1 = spin-lattice relaxation time of brain tissue water in the absence of perfusion and cross-relaxation,

M = Z magnetization of water per gram of brain tissue,

M^0 = equilibrium value of M,

M_a = Z magnetization of water per milliliter of arterial blood,

M_v = Z magnetization of water per milliliter of venous blood,

$M_{immobile}$ = Z magnetization of immobile water per gram of brain tissue,

k_{for}, k_{rev} = magnetization transfer rate constants between tissue water and immobile water.

Water can be considered as a free diffusible tracer such that

$$M_a^0 = \frac{1}{\lambda}M^0, \tag{5.6}$$

and

$$M_v = \frac{1}{\lambda} M, \tag{5.7}$$

where λ is the partition coefficient defined as (ml of water/g of brain tissue)/(ml of water/ml of blood).

When the spins are continuously saturated in a slice or region of the carotid arteries that flow into a region of interest in the brain those spins are labeled. The saturation can be accomplished by a saturation or an inversion pulse sequence. If we define the degree of spin labeling as

$$\alpha = \frac{1}{2}\left(1 - \frac{M_a}{M_a^0}\right), \tag{5.8}$$

and substitute Eqs. (5.6)-(5.8) into Eq. (5.5), we then have

$$\frac{dM}{dt} = \frac{M^0 - M}{T_1} - k_{for} M + k_{rev} M_{immobile} + (1 - 2\alpha)\frac{p}{\lambda} M^0 - \frac{p}{\lambda} M. \tag{5.9}$$

Now let us consider the terms associated with magnetization transfer in Eq. (5.9). It is easy to see that the term including $M_{immobile}$ can be removed if we apply the saturation transfer method described in Subsection 5.2.1 on the brain tissue region of interest. Assuming a constant off-resonance pulse being turned on all the time during the experiment such that $M_{immobile}$ is perfectly saturated, Eq. (5.9) becomes

$$\frac{dM}{dt} = \frac{M^0 - M}{T_1} - k_{for} M + (1 - 2\alpha)\frac{p}{\lambda} M^0 - \frac{p}{\lambda} M. \tag{5.10}$$

Solving Eq. (5.10) at steady-state we obtain the solution when immobile spins are saturated without arterial spin labeling ($\alpha = 0$)

$$M_{\alpha=0}^{sat} = \frac{1/T_1 + p/\lambda}{1/T_1 + k_{for} + p/\lambda} M^0, \tag{5.11}$$

and when immobile spins are saturated with arterial spin labeling ($\alpha \neq 0$) the steady-state solution gives

$$M_{\alpha}^{sat} = \frac{\frac{1}{T_1} - (2\alpha - 1)\frac{p}{\lambda}}{\frac{1}{T_1} + \frac{f}{\lambda}} M_{\alpha=0}^{sat}. \tag{5.12}$$

Using both Eqs. (5.11) and (5.12) tissue perfusion rate p can be calculated as

$$p = \frac{\lambda}{T_1}\left(\frac{M_{\alpha=0}^{sat} - M_{\alpha}^{sat}}{M_{\alpha}^{sat} + (2\alpha - 1) M_{\alpha=0}^{sat}}\right). \tag{5.13}$$

From Eq. (5.13) it can be seen that the perfusion rate is determined only by the saturated tissue compartment magnetization with and without spin labeling and the degree of the spin labeling. It has been claimed that based on the experiments with rats, the degree of spin labeling is not sensitive to the flow velocity of the tagged spins.[88] However, several research groups have reported results from human studies which showed signal changes do depend upon the flow velocity of the tagged spins.[80,89,90] It is believed that the signal change depending upon the flow velocity of the labeled spins is caused by the combination of the different degrees of spin labeling due to varied transit times and a larger blood volume due to capillary dilatation. The changes in the degree of spin labeling in human study are caused by a slower flow and a greater distance from the spin labeling position to the image plane which results in the different transit time for different flow velocity. People call this phenomenon an in-flow effect. In application of Eq. (5.13), this technique requires an effective way to extract the signal only from the tissue compartment,

thus separating the tissue signal from the total signal that includes the signal contributed by the magnetization in capillary blood.

It has been shown that using the arterial spin labeling technique reduces the number of compartments, thus reducing the number of parameters that need to be estimated in the perfusion model.[78,79,91] The importance of this model is to provide a feasible method to quantify perfusion.

In the next section the three-compartment perfusion model developed in Chapter 4 is used to study the effect of flow rate on MRI signal using the arterial spin tagging technique. In fact, whether perfusion measurement depends upon flow velocity has become a very important and interesting research topic in today's MRI perfusion study.

5.4 The Effect of Flow Rate of Arterially Tagged Endogenous Protons on the MRI Signal Intensity

MR imaging of tissue perfusion by pulse labeling endogenous water spins has the advantage of not requiring the injection of a fairly high concentration of contrast material. In Chapter 3, we developed a model for the MRI signal of an excited slice of tissue which was a function of perfusion and extraction assuming that biological tissue can be represented by a blood and a tissue compartment. A key factor in the modulation of the MRI signal is a time-of-flight effect whereby unexcited spins perfuse the excited region and exchange with the blood and the tissue compartments. The exchange delays the exit of the spins from the slice, thereby decreasing their contribution to the slice signal intensity in future repetitive pulse measurements. In Chapter 4, we modified this two-compartment model to include a third compartment for immobile water (Fig. 4.3), which we have verified by computer simulations and phantom experiments.

The constant infusion technique discussed in Section 5.3 has been proposed to measure tissue perfusion by pulse labeling endogenous spins external to the tissue region and to follow the change in the MRI signal as the labeled arterial spins flow into the tissue region of interest.[78,79] The MRI signal is modelled using Fick's principle in combination

with the Bloch equations. The approach uses a tag that is constantly infused into the area of interest and assumes that the partition coefficient (ratio of concentration in the tissue to concentration in the blood) is known at equilibrium. By continuously infusing tagged spins in the carotid arteries, the tissue in the region of interest in the brain comes to equilibrium with the blood compartment. This simplifies the equations for the MRI signal since the blood magnetization can be replaced by the tissue magnetization divided by the partition coefficient. The purpose of the study in this section is to use our three-compartment perfusion model of differential equations to study the external labelling technique and to determine the signal contrast expected for various flow velocities of blood flowing into a selected tissue slice. Magnetization transfer is also used to suppress signal variations that depend upon the immobile water compartment.

5.4.1 Theory

For regions both internal and external to the selected slice B, the system of second order partial differential equations [Eqs. (4.5)-(4.10)] are used to define the transverse and longitudinal magnetization in blood [$M^{1+}(z,t)$ and $M^{1}{}_{z}(z,t)$], tissue [$M^{2+}(z,t)$ and $M^{2}{}_{z}(z,t)$], and bound water [$M^{3+}(z,t)$ and $M^{3}{}_{z}(z,t)$] compartments as a function of time and distance perpendicular to the slice, where D^* and D are diffusion coefficients for blood and tissue spins, respectively. V is flow rate, β is volume ratio of tissue to blood, β_1 is volume ratio of tissue to bound water, Ks are rate constants between compartments. The MRI signal in the transverse plane was measured by integrating the transverse magnetization as a function of flow velocity:

$$S_V(t) = \frac{1}{1+\beta+\frac{\beta}{\beta_1}}\int\left(M^{1+}+\beta M^{2+}+\frac{\beta}{\beta_1}M^{3+}\right)dz. \qquad (5.14)$$

5.4.2 Computer Simulations

The simulations had two time periods. During the first 3 s, it was assumed that an off resonance low power pulse was applied to a 0.5 cm selected slice of tissue (slice B in Fig. 5.2), saturating the spins through magnetization transfer and allowing us to set $M_z^3 = 0$. During this first 3 s, we numerically solved the system of differential equations for the MRI signal and integrated this signal across the 0.5 cm slice. After the first 3 s, we assumed that the saturation pulse continued, but we assumed an inversion pulse was applied to a 0.25 cm slice in front of the slice B so that all flowing spins entering the slice were constantly inverted. We continued to numerically solve the system of differential equations to determine the integrated signal across the 0.5 cm slice as the tagged spins continued to enter the slice. To study the effect of flow rate on MRI signal, flow velocities of V=0.5, 1, and 1.5 cm/sec, slice thickness of the imaging plane of Δz=0.2, 0.3, 0.4, and 0.5 cm, and flip angles of the inversion pulse of $\theta = 90°$, $120°$, and $180°$ were simulated. In all simulations, $\beta = 8$, $\beta_1 = 8$, $K_1 = K_3 = 0.8\ s^{-1}$, $K_5 = 1.2\ s^{-1}$, $T_1 = 500$ ms and $T_2 = 50$ ms for the entire sample.

The MRI signal intensity as a function of time and flow velocity was normalized to S_0, the integrated equilibrium magnetization across the slice.

5.4.3 Results

Fig. 5.3 shows the normalized MRI signal integrated across the slice as a function of time and flow velocity. Velocities were chosen as V=0.5, 1.0, 1.5 cm/sec. One notices that the signal after labeling with an inversion pulse at 3 s is significantly affected by flow velocity. The tagged spins perfuse into tissue causing a delayed exit from the selected slice that results in a signal loss. The time-of-flight effect of tagged spins flowing into the slice decreases the signal as the flow velocity increases. It appears that as the velocity increases the signal will approach an equilibrium.

In Fig. 5.4 normalized MRI signal integrated across the slice was plotted as a function of time and slice thickness of the imaging plane: 0.5, 0.4, 0.3, 0.2 cm. Flow

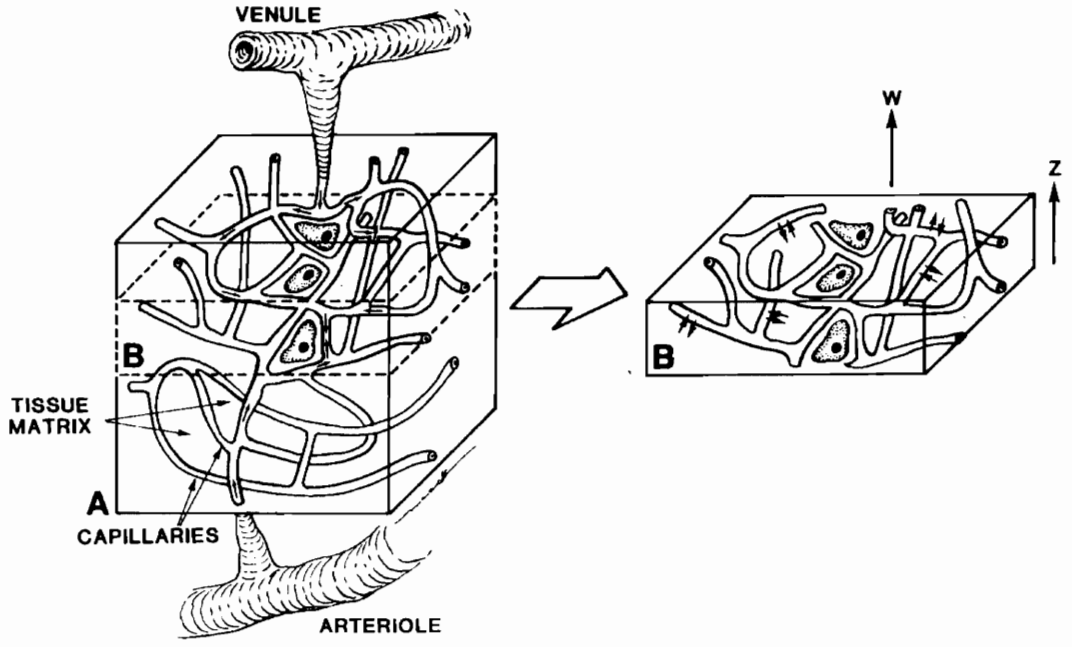

Fig. 5.2 Network of capillaries surrounded by a tissue matrix. Using MRI a slice of tissue B is excited by an rf pulse.

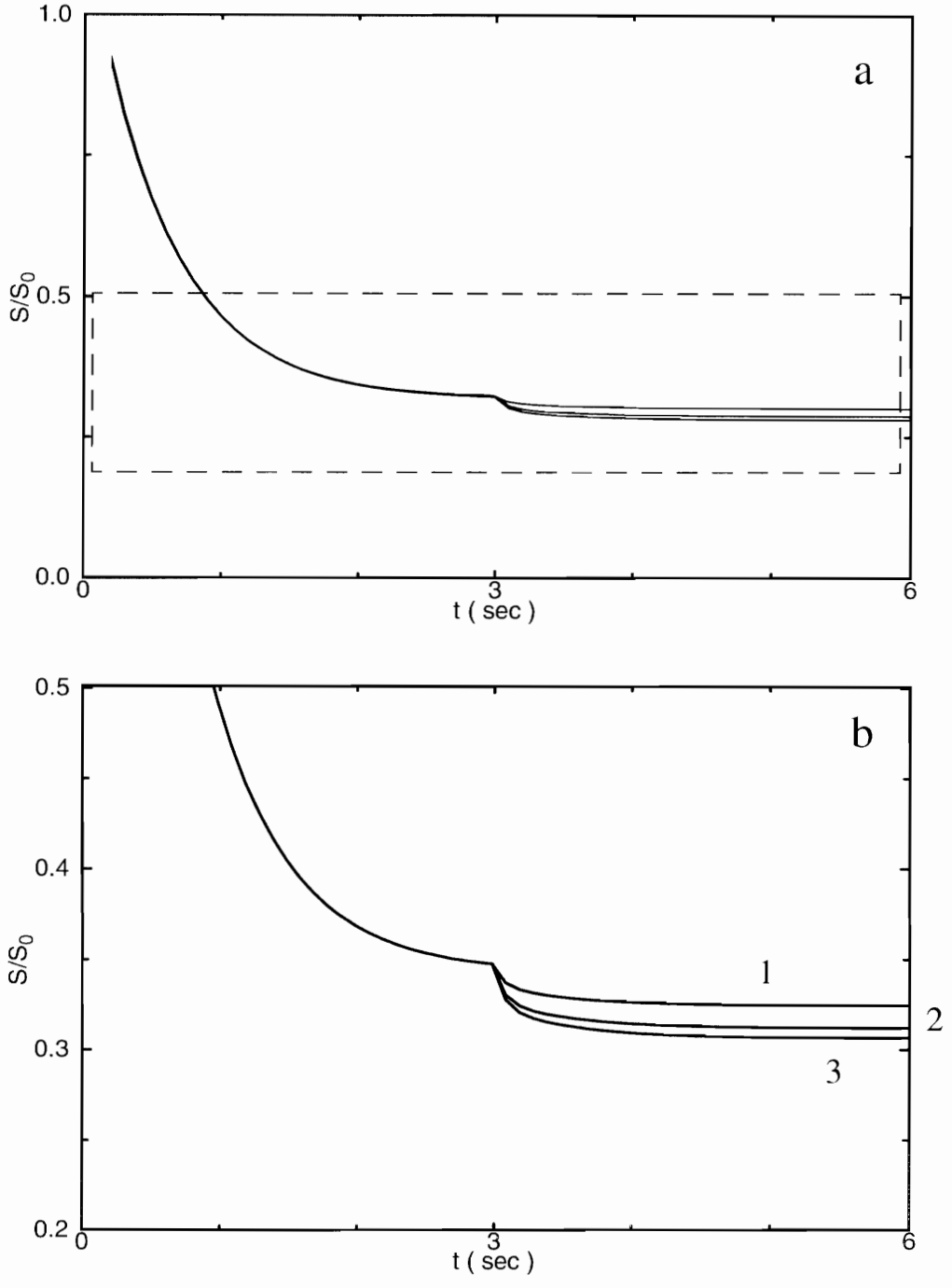

Fig. 5.3 Normalized MRI signal integrated across the slice as a function of time and flow velocity. (a): The saturation of spins with different flow velocity through magnetization transfer during the first 3 s and through the spin labeling in addition to the magnetization transfer during the second 3 s. (b): Magnification of the dotted box in (a) showing flow dependence of signal contrast. Velocities: (1) 0.5, (2) 1.0, (3) 1.5 cm/sec.

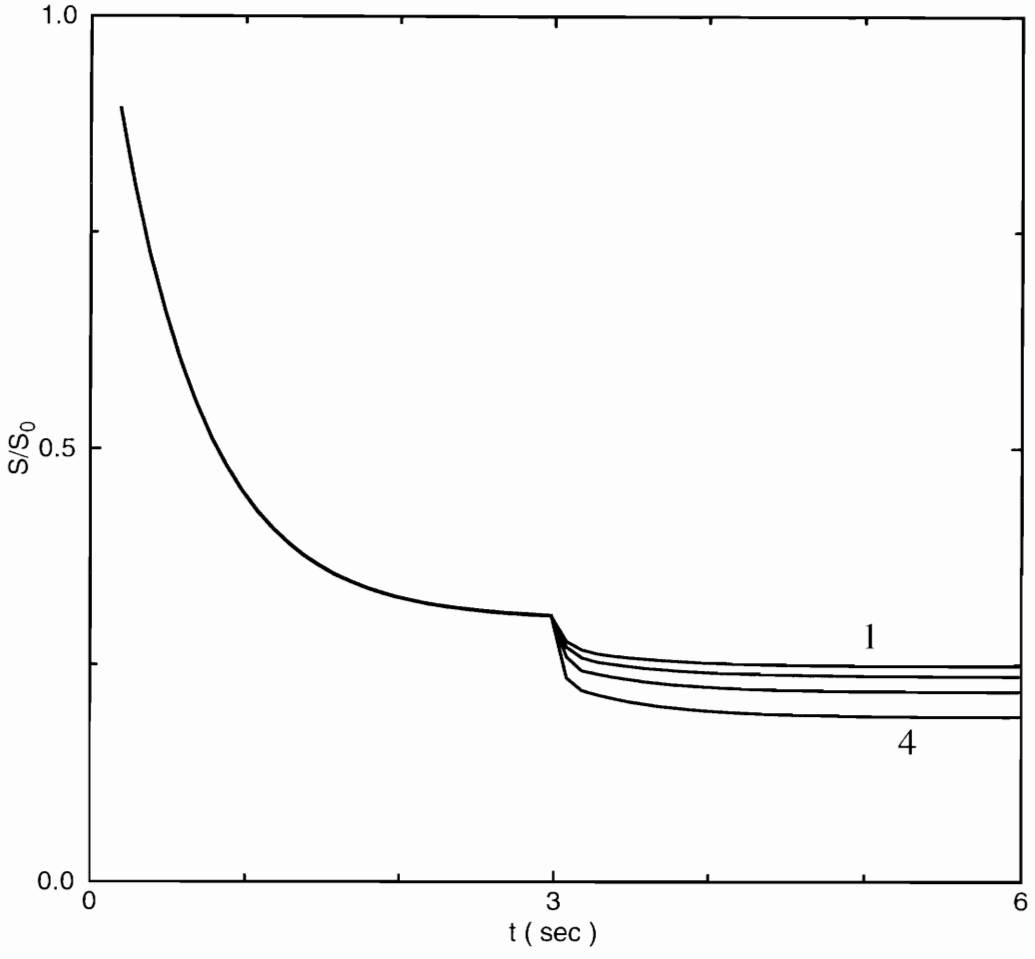

Fig. 5.4 Normalized MRI signal integrated across the slice as a function of time and the slice thickness of the imaging plane. The slice thickness (from top to bottom): (1) 0.5 cm, (2) 0.4 cm, (3) 0.3 cm, (4) 0.2 cm. Flow velocity: V=1.5 cm/sec.

velocity V was equal to 1.5 cm/sec. This graph clearly shows that the normalized signal contrast using the labeling technique depends upon the exchange between the compartments. The spins in tissue exchange with spins in blood causing a mixture of labeled and unlabeled spins in the blood along the flow direction. Increasing the slice thickness results in a smaller portion of labeled spins in blood at the end of the slice and less signal contrast.

Fig. 5.5 plotted the normalized MRI signal integrated across the slice as a function of time and the flip angle of the labeling pulse: 60°, 90°, 120°, 180°. Flow velocity V was equal to 1.5 cm/sec. When increased flip angles are used to label the spins during the saturation pulse, a greater decrease in MR signal intensity is observed.

5.4.4 Experiments

A GRASS pulse sequence with a selective saturation pulse in the z-direction was used on a human brain study. Since the saturation pulse is an off-resonance pulse, magnetization transfer contrast (MTC) occurs. We first used the saturation pulse in the z-direction at a fixed distance above the slice of the region of interest (ROI), and then below the ROI with the same fixed distance to produce the same MTC. However, the saturation pulse below the ROI also labeled the flowing spins by saturation. The intensity difference between the two images should be a function of perfusion. As it was shown in Chapter 3, the time-of-flight effect is a key factor in perfusion studies. Therefore, it is expected that the intensity difference is flow rate dependent.

The experiments were performed on a GE 1.5T scanner. A gradient refocusing pulse sequence was used with flip angle=30°, TE=14 ms, TR=40 ms, and a 1 cm slice thickness in the z-direction was selected. The selective saturation pulse with a flip angle of 90° was applied to an 8 cm slice which was 3 cm above and 3 cm below the imaged slice. The effect of flow rate on labeled spins was studied for hypocarbia (low pCO_2) and hypercarbia (high pCO_2) conditions, respectively.

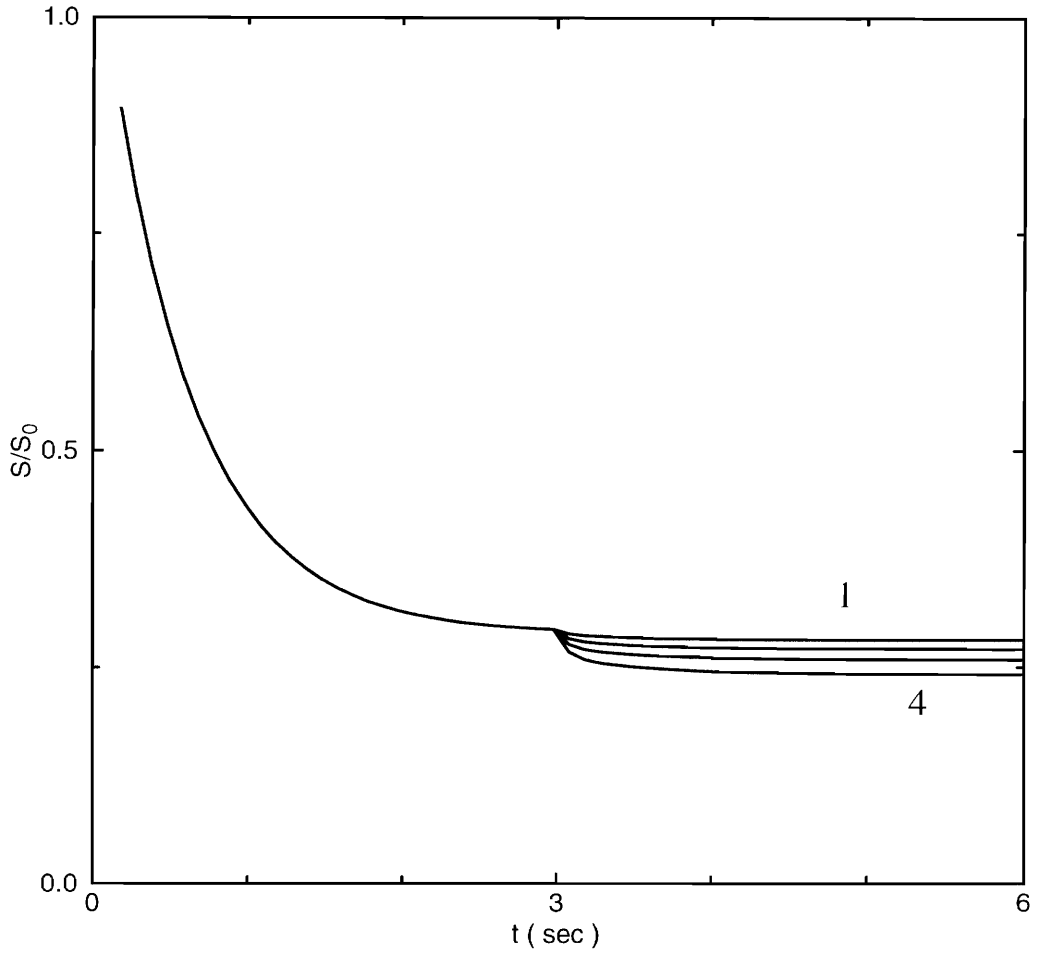

Fig. 5.5 Normalized MRI signal integrated across the slice as a function of time and the flip angle of labeling pulse: (1) 90°, (2) 120°, (3) 150°, (4) 180°. Flow velocity: V=1.5 cm/ sec.

Fig. 5.6. shows transverse MR images of a human brain under hypocarbia condition. Left: the image with the saturation pulse applied to the location superior to the imaging plane. Middle: the image with the saturation pulse inferior to the imaging plane. Right: the subtraction image. A line profile is plotted below the subtraction image. This image shows that the perfusion of the brain can be extracted from the MR signal intensity difference between labeled and unlabeled flowing spins.

Fig. 5.7 shows transverse MR images of the same human brain under hypercarbia condition. The image on the left was obtained with the saturation pulse applied to the location superior to the imaging plane. The image in the middle was obtained with the saturation pulse inferior from the imaging plane. Subtracting the inferiorly saturated image (middle) from the superiorly saturated image (left), we obtain the difference image (right). Compared with Fig. 5.6, we see that the perfusion effect is enhanced when the flow rate is increased.

5.4.5 Discussion

The simulation results show that the MR signal contrast using the arterial spin labeling technique depends upon the slice thickness of the imaging plane and the flip angle of the inversion pulse which is applied outside of the imaging plane.

From simulations and experiments we see that (1) the arterially tagged endogenous protons will saturate the MR signal intensity through tissue perfusion and (2) high flow rate of arterially tagged flowing spins can enhance MR signal contrast which is a function of tissue perfusion.

The model described in Section 5.3 is based upon indicator dilution principles that have been used for years in the study of physiological processes in biology. This model uses excited protons as the indicator to modulate the signal based upon perfusion characteristics. What one needs to keep in mind when using excited protons spins as the indicator is the small change that perfused spins have on the MRI signal. In nuclear medicine with tracer amounts one can expect to obtain significant sensitivity to perfusion

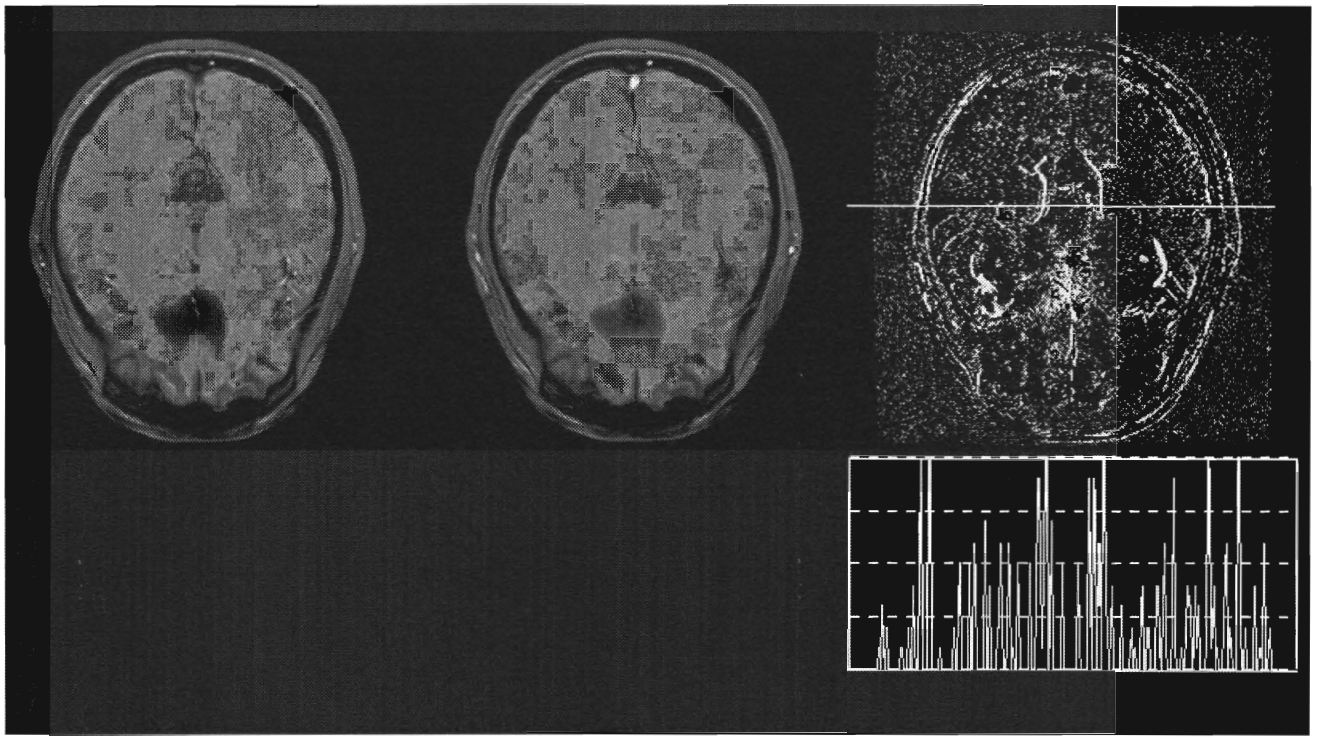

Fig. 5.6 Transverse MR images of a human brain under hypocarbia condition. Left: the image with the saturation pulse applied to the location superior to the imaging plane. Middle: the image with the saturation pulse inferior to the imaging plane. Right: the subtraction image. A line profile is plotted below the subtraction image.

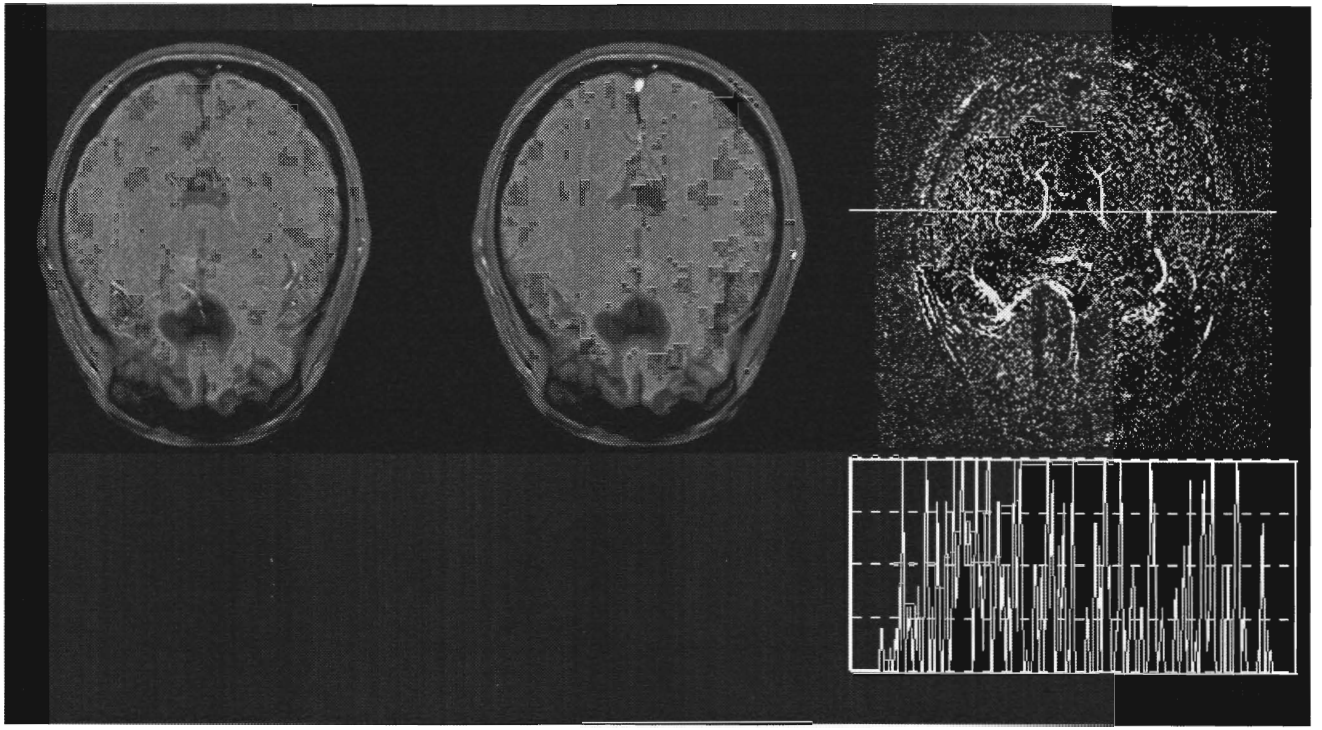

Fig. 5.7 Transverse MR images of the same human brain under hypercarbia condition. Left: the image with the saturation pulse applied to the location superior from the imaging plane. Middle: the image with the saturation pulse inferior from the imaging plane. Right: the subtraction image. A line profile is plotted below the subtraction image.

changes, whereas with MRI, the signal change may be quite small. One of the problems with MRI, is the fast relaxation of the excited protons. Also, because MRI is such a useful tool for measuring so many physical properties, all the parameters that measure these properties come into play when measuring tissue perfusion, such as flow, diffusion, exchange rates between compartments. Therefore, the measurement of tissue perfusion requires the estimation of these parameters unless they can be isolated from the data by some method such as magnetization transfer.

Our model is also based upon the indicator dilution principle but differs on some points from the model described in Section 5.3. First, we describe the perfusion process both in space and time using Bloch equations and combining these with differential equations which describe the kinetic exchange between the blood compartment and extravascular compartment. For the model in Section 5.3, it was assumed that the flow velocity of the labeled spins is fast enough to perfuse the entire imaging plane such that the relaxation of the labeled spins is negligible. Our development includes the rate of change between blood and extravascular compartments whereas the other model assumes constant inflow and uses a partition coefficient to describe the exchange as the ratio of excited proton concentration between the blood and tissue at equilibrium. Also, our development includes the transverse magnetization in the model.

The reason that our simulation results show the sensitivity of the signal contrast to the flow velocity of the labeled spins, when a tagging technique is used, is that the labeled spins will relax during the time the labeled spins flow into the imaging plane. A greater transit time due to a slower flow rate results in a smaller signal contrast. Our experimental results on human brain (the transit time for human brain is longer than that for rat) showed agreement with our computer simulations.

In summary, our simulations and experimental results show that the accuracy of estimated kinetic parameters depend on the signal contrast that in turn is a function of the flow velocity of the labeled spins.

CHAPTER 6

CONCLUSIONS

6.1 Scientific Contributions

An MRI multicompartment tissue perfusion model was developed. Computer simulations of the multicompartment model were performed to study the MRI signal as a function of T_1/T_2 relaxation processes and the following physiological parameters: blood flow velocity, perfusion fraction, diffusion, and rate of exchange between the blood and extravascular tissue compartments. In computer simulations, the modified Bloch equations were solved numerically for both longitudinal and transverse magnetization for each compartment, which distinguishes this work from other perfusion studies using MRI. The total signal was obtained by integrating the transverse magnetization of compartments across the slice. We have demonstrated that the total signal intensity for an excited slice is modulated by the physiological processes, such as relaxation of excited spins, flow in capillary networks, diffusion in tissue and capillaries, and exchanges between the vascular, tissue, and immobile water compartments. The simulations indicate that the modulation of the MRI signal is dependent upon the perfusion of tissue by blood which causes a time-of-flight effect as tissue is continuously excited by a selective rf pulse. The total signal intensity is dominated by the flow velocity and the tissue to blood volume ratio and depends less upon diffusion. The longitudinal magnetization signal appears to be more sensitive to rate constant variations for large blood volumes. However, for tissue such as the brain with blood volumes typically less than 10%, the signal modulation can be as small as 2%. NMR is useful in probing compartments because it is sensitive both to changes in the intracellular environment and to exchange effects.

The multicompartment model was verified by experiments with Sephadex gel phantoms. Computer simulations of two-compartment and three-compartment models were compared in experiments that used two chromatography columns packed with Sephadex gel G-25 and G-50, respectively. The results of the experiments proved that the MRI signal intensity in the perfused columns is a function of the rate of exchange between extrabead and intrabead compartments. The slice thickness has a significant effect upon the signal-versus-flow curves because the perfusion model is based upon a time-of-flight effect. A smaller slice thickness would be desired to resolve smaller differences between exchange rate constants. However, there is a trade-off in the signal-to-noise ratio. The simulations also showed that both two-compartment and three-compartment models could be used to fit the experimental data. However, in practice, it may be that a two-compartment model will be easier than a three-compartment model to fit to experimental biological data.

An effort to simplify the multicompartment models investigated in this study was made using arterially labeled spins as a tracer for a constant infusion technique combined with magnetization transfer technique to reduce the number of compartments (the blood and the immobile water compartments in this situation), thus reducing the number of parameters that need to be estimated in the perfusion model. Simulations and experiments on human brain demonstrate that the arterially tagged endogenous protons will saturate the MR signal intensity through tissue perfusion and high flow rate of arterially tagged flowing spins can enhance MR signal contrast so that the contrast is a function of tissue perfusion. Also, the MR signal contrast using the arterial spin labeling technique is sensitive to the slice thickness of the imaging plane and the flip angle of the inversion pulse which is applied outside of the imaging plane. Therefore, the accuracy of kinetic parameter estimates will rely on the signal contrast that depends upon the flow velocity of the labeled spins and the blood volume. In applying compartment modeling *in vivo*, parameter estimates cannot be derived by varying flow. We speculate that independent

measurements of flow will have to be made in order to estimate exchange rate constants. The arterial spin labeling technique has shown sufficient potential to encourage researchers to continue to seek an approach for measuring perfusion quantitatively using MRI.

Because of the clinical need, tests allowing noninvasive assessment of perfusion will continue to play an important role in clinical medicine. MRI presents promise as a technique by which an imaging protocol could image perfusion without the use of contrast agents or ionizing radiation.

6.2 Future Work

Further research is required to develop methods for estimating the model parameters and to develop pulse sequences that use the modulation of both the transverse and longitudinal magnetization to extract physiological parameters. In particular, estimation techniques need to be developed in which model parameters are determined by least squares fitting to several MRI signal measurements that are obtained for various pulse sequence parameters.

APPENDIX A

THE COMPUTER SIMULATION CODE FOR A TWO-COMPARTMENT MODEL

```
C     PROGRAM PERFUSION_2C
C!!!!!!!!!!!!!!!!!!!!!!!!!!!!!!!!!!!!!!!!!!!!!!!!!!!!!!!!!!!!!!!!!!!!!!!!
C     WRITTEN BY XIANGYANG MA                                          C
C     NOVEMBER 15, 1989                                                C
C     REVISED AUGUST 6, 1994                                           C
C!!!!!!!!!!!!!!!!!!!!!!!!!!!!!!!!!!!!!!!!!!!!!!!!!!!!!!!!!!!!!!!!!!!!!!!!

        COMMON /COEFFICIENT/ UVX,UVY,UVZ,UMX,UMY,UMZ,
     &             SIGNAL,CUZ1,CUZ2,CUZ3,CUZ4,CUZ5,CUZ6,
     &             CVZ1,CVZ2,CVZ3,CVZ4,CVZ5,CVZ6,
     &             CUVXYG,CUXY1,CVXY1,CMZ1,CMZ2,CMZ3,CMZ4,
     &             CMXY1,N,N1,ILEFT,IRIGHT,XL,Z1,Z2,XH,XK,
     &             BETA,BETA1,MM,NSEQ,NTOTAL,BRATIO,GNOR,
     &             U00,V00,UM0

        DOUBLE PRECISION UVX(5000,7),UVY(5000,7),UVZ(5000,7),
     &             UMX(5000,7),UMY(5000,7),UMZ(5000,7),
     &             SIGNAL(100),CUZ1,CUZ2,CUZ3,CUZ4,CUZ5,CUZ6,
     &             CVZ1,CVZ2,CVZ3,CVZ4,CVZ5,CVZ6,CUVXYG,
     &             CUXY1,CVXY1,CMZ1,CMZ2,CMZ3,CMZ4,CMXY1


C
C        XH    - STEP SIZE IN TIME
C        XK    - STEP SIZE IN Z
C        D     - DIFFUSSION COEFFICIENT OF EXTRABEAD
C        DD    - DIFFUSSION COEFFICIENT OF INTRABEAD
C        TU1    - SPIN LATICE RELAXATION TIME OF FLOW
C        TV1    - SPIN LATICE RELAXATION TIME OF TISSUE
C        TU2    - SPIN-SPIN RELAXATION TIME OF FLOW
C        TV2    - SPIN-SPIN RELAXATION TIME OF TISSUE
C        TM1    - SPIN LATICE RELAXATION TIME OF BOUND WATER
C        TM2    - SPIN-SPIN RELAXATION TIME OF BOUND WATER
C        TR     - REPITITION TIME
C        TE     - ECHO TIME
C        XK1    - RATE COEFFICIENT - EXTRABEAD TO INTRABEAD
C        XK2    - RATE COEFFICIENT - INTRABEAD TO EXTRABEAD
C        XKM    - RATE COEFFICIENT - IN AND OUT BOUND WATER
C        BETA   - VOLUME RATIO OF INTRABEAD TO EXTRABEAD
C        BETA1  - VOLUME RATIO OF INTRABEAD TO BOUND WATER
C        W      - FLOW VELOCITY OF EXTRABEAD
C        WT     - FLOW VELOCITY OF INTRABEAD
C        U00    - EQUILIBRIUM MAGNETIZATION IN EXTRABEAD COMPARTMENT
C        V00    - EQUILIBRIUM MAGNETIZATION IN INTRABEAD COMPARTMENT
C        UM0    - EQUILIBRIUM MAGNETIZATION IN BOUND WATER COMPARTMENT

C
         GAMMA=2.68E4
         NFLOW=7
C
C        *************DIFFUSSION COEFFICIENTS**********
C
         D=1.0E-4
C         IN CM^2/SEC
         DD=2.5E-5
C         IN CM^2/SEC
C
C        ******PHYSICAL VOLUME RATIO******
C
         PHYSICAL_BETA= 1.28
C
         VEXTRA= 0.9/( PHYSICAL_BETA + 1 )
C
```

```
C       ******VOLUME RATIO***************
C
        BETA=PHYSICAL_BETA
C
C       ******EQUILIBRIUM MAGNETIZATION**
C
        U00=VEXTRA*1000.
        V00=BETA*VEXTRA*1000.
C
C       ******RATE COEFFICIENTS***********
C
        XK1= 0.0
C         IN SEC**(-1)
C
        XK2= XK1*U00/V00
C         IN SEC**(-1)
C
C       ******RELAXATION TIMES******
C
        T1TOTAL=0.603
C         IN SEC

        TU1=2.5
C         IN SEC

        TV1=BETA*VEXTRA/(0.9/T1TOTAL-VEXTRA/TU1)
C         IN SEC

        T2TOTAL=0.057
C         IN SEC

        TU2=2.0
C         IN SEC
        TV2=BETA*VEXTRA/(0.9/T2TOTAL-VEXTRA/TU2)
C         IN SEC
C
C       ********TIME OF REPITITION*********
C
        TR=0.4
C         IN SEC
C
C       *********ECHO TIME**********
C
        TE = 15.0E-3
C
C       **** MAGNITUDE OF GRADIENT *****
C
        GZ1= 0.0
        GZ2= 0.0
C
C       ***********FLOW RATES***********
C
        DO 7000 MM=1,NFLOW
        W= 0.0 + 0.01*(MM - 1)
C        !CM PER SEC

C
C       *****STEP SIZE*****************
C
        XH=1.0E-05
C         IN SEC
        XK=SQRT(6.*XH)/8.
C
C       ******** TOTAL NO. OF PULSE ********
C
```

```
      NTOTAL=4
C
C     *******POSITIONS OF SLICE BOUNDARYIES********
C
      Z1=-0.15
C       IN CM
      Z2=0.15
C       IN CM
C
C     *********TOTAL LENGTH OF REGION**********
      XL=0.35
C       IN CM
C
C     ****************************************

      N=2.*XL/XK
      N1=N+1
C
      M1=TR/XH
      MTE=TE/XH
C
      ILEFT=(XL+Z1)/XK
      IRIGHT=(XL+Z2)/XK
      BRATIO=BETA/BETA1
      GNOR=1+BETA+BRATIO
      GNOR2=1+BETA
      UVM0=1/GNOR*(U00+BETA*V00+BRATIO*UM0)
      SIGNAL0=UVM0*(Z2-Z1)
C
      DO 15 J=1,N
        UVY(J,2)=0.0
        UVY(J,4)=0.0
        UVZ(J,2)=U00
        UVZ(J,4)=V00
15    CONTINUE

C
      CUZ1=(1./XH-2.*D/XK**2-(XK1+XK3)*BETA-1./TU1)*XH
      CUZ2=(D/XK**2-W/2./XK)*XH
      CUZ3=(D/XK**2+W/2./XK)*XH
      CUZ3U00=CUZ3*U00
      CUZ4=XK2*BETA*XH
      CUZ5=XH/TU1*U00
      CUZ6=XK4*BETA*XH
      CUXY1=(1./XH-2.*D/XK**2-(XK1+XK3)*BETA-1./TU2)*XH
C
      CVZ1=(1./XH-2.*DD/XK**2-(XK2+XK5)-1./TV1)*XH
      CVZ2=(DD/XK**2)*XH
      CVZ3=(DD/XK**2)*XH
      CVZ3V00=CVZ3*V00
      CVZ4=XK1*XH
      CVZ5=XH/TV1*V00
      CVZ6=XK6*XH
      CVXY1-(1./XH-2.*DD/XK**2-(XK2+XK5)-1./TV2)*XH

C     **********SIMULATION START BELOW**********

      NSEQ=1

5000  IF(NSEQ.EQ.NTOTAL+1) GO TO 7000
C
      GZ=GZ1
      CUVXYG=XH*GAMMA*GZ*XK
      CALL SOLUTION(M1,MTE)
C
```

```
      IF(NSEQ.NE.NTOTAL) GO TO 5500
C
      SUMU1=0.0
      SUMV1=0.0

      DO 35 J=ILEFT,IRIGHT
        SUMU1=SUMU1+ UVY(J,2)*XK
        SUMV1=SUMV1+ UVY(J,4)*XK
35    CONTINUE

      SIGNAL(MM)=1./GNOR2*(SUMU1+BETA*SUMV1)

5500  NSEQ=NSEQ+1
      GO TO 5000

7000      CONTINUE

      OPEN(4,FILE='G25b128k0.dat',STATUS='NEW')

      DO 60 I=1,NFLOW
        VFLOW = 0.0 + ( I - 1 ) * 0.1
        WRITE(4,120) VFLOW, DLOG( ABS( SIGNAL(I)/SIGNAL(1) ) )
60    CONTINUE

      WRITE(4,130)


120   FORMAT(F12.8,5x,F12.8)
130   FORMAT( '& V          LN( SV(G-25)/S0(G-25) ) ' )

      CLOSE(4)

      END

C     ********************************************
C
C         SUBROUTINE   SOLUTION
C
C     ********************************************
      SUBROUTINE SOLUTION(M,MTE)
      COMMON /COEFFICIENT/ UVX,UVY,UVZ,UMX,UMY,UMZ,
     &            SIGNAL,CUZ1,CUZ2,CUZ3,CUZ4,CUZ5,CUZ6,
     &            CVZ1,CVZ2,CVZ3,CVZ4,CVZ5,CVZ6,
     &            CUVXYG,CUXY1,CVXY1,CMZ1,CMZ2,CMZ3,CMZ4,
     &            CMXY1,N,N1,ILEFT,IRIGHT,XL,Z1,Z2,XH,XK,
     &            BETA,BETA1,MM,NSEQ,NTOTAL,BRATIO,GNOR,
     &            U00,V00,UM0

      DOUBLE PRECISION UVX(5000,7),UVY(5000,7),UVZ(5000,7),
     &            UMX(5000,7),UMY(5000,7),UMZ(5000,7),
     &            SIGNAL(100),CUZ1,CUZ2,CUZ3,CUZ4,CUZ5,CUZ6,
     &            CVZ1,CVZ2,CVZ3,CVZ4,CVZ5,CVZ6,CUVXYG,
     &            CUXY1,CVXY1,CMZ1,CMZ2,CMZ3,CMZ4,CMXY1


      IZ1=(XL+Z1)/XK
      IZ2=(XL+Z2)/XK

C     ****90 DEGREE PULSE FROM Z1 TO Z2 UNTIL LINE #25****

      DO 25 J=IZ1,IZ2

        UVY(J,2)=UVZ(J,2)
        UVY(J,4)=UVZ(J,4)
```

```
C
C       ************ANY DEGREE PULSE************
C          UVZ(J,2)= cosd(flip_angle)*U00
C       ****************************************
C
          UVZ(J,2)=0.
          UVZ(J,4)=0.
25      CONTINUE


        DO 10 I=1,M
          UVY(1,2)=UVY(2,2)
          UVY(1,4)=UVY(2,4)
          UVY(N+1,2)=UVY(N,2)
          UVY(N+1,4)=UVY(N,4)

          UVZ(1,2)=UVZ(2,2)
          UVZ(1,4)=UVZ(2,4)
          UVZ(N+1,2)=UVZ(N,2)
          UVZ(N+1,4)=UVZ(N,4)

          DO 14 J=1,N1
            UVY(J,1)=UVY(J,2)
            UVY(J,3)=UVY(J,4)
            UVZ(J,1)=UVZ(J,2)
            UVZ(J,3)=UVZ(J,4)
14        CONTINUE


C
          DO 30 J=2,N
        UVY(J,2)=CUXY1*UVY(J,1)+CUZ2*UVY(J+1,1)+CUZ3*UVY(J-1,1)
     &           +CUZ4*UVY(J,3)-CUVXYG*(J-N/2)*UVX(J,1)
     &           +CUZ6*UMY(J,1)

        UVY(J,4)=CVXY1*UVY(J,3)+CVZ2*UVY(J+1,3)+CVZ3*UVY(J-1,3)
     &           +CVZ4*UVY(J,1)-CUVXYG*(J-N/2)*UVX(J,3)
     &           +CVZ6*UMY(J,1)

        UVZ(J,2)=CUZ1*UVZ(J,1)+CUZ2*UVZ(J+1,1)+CUZ3*UVZ(J-1,1)
     &           +CUZ4*UVZ(J,3)+CUZ5+CUZ6*UMZ(J,1)

        UVZ(J,4)=CVZ1*UVZ(J,3)+CVZ2*UVZ(J+1,3)+CVZ3*UVZ(J-1,3)
     &           +CVZ4*UVZ(J,1)+CVZ5+CVZ6*UMZ(J,1)
30        CONTINUE


  IF(NSEQ.EQ.NTOTAL.AND.I.EQ.MTE) THEN
    GO TO 100
  ENDIF



10      CONTINUE

100     CONTINUE

        RETURN
        END
```

APPENDIX B

THE COMPUTER SIMULATION CODE FOR A THREE-COMPARTMENT MODEL

```
C     PROGRAM PERFUSION_3C
C!!!!!!!!!!!!!!!!!!!!!!!!!!!!!!!!!!!!!!!!!!!!!!!!!!!!!!!!!!!!!!!!!!!!!!!!
C     WRITTEN BY XIANGYANG MA                                          C
C     OCTOBER 25, 1991                                                 C
C     REVISED: NOVEMBER 16, 1994                                       C
C!!!!!!!!!!!!!!!!!!!!!!!!!!!!!!!!!!!!!!!!!!!!!!!!!!!!!!!!!!!!!!!!!!!!!!!!

        COMMON /COEFFICIENT/ UVX,UVY,UVZ,UMX,UMY,UMZ,
     &             SIGNAL,CUZ1,CUZ2,CUZ3,CUZ4,CUZ5,CUZ6,
     &             CVZ1,CVZ2,CVZ3,CVZ4,CVZ5,CVZ6,
     &             CUVXYG,CUXY1,CVXY1,CMZ1,CMZ2,CMZ3,CMZ4,
     &             CMXY1,N,N1,ILEFT,IRIGHT,XL,Z1,Z2,XH,XK,
     &             BETA,BETA1,MM,NSEQ,NTOTAL,BRATIO,GNOR,
     &             U00,V00,UM0

        DOUBLE PRECISION UVX(5000,7),UVY(5000,7),UVZ(5000,7),
     &             UMX(5000,7),UMY(5000,7),UMZ(5000,7),
     &             SIGNAL(100),CUZ1,CUZ2,CUZ3,CUZ4,CUZ5,CUZ6,
     &             CVZ1,CVZ2,CVZ3,CVZ4,CVZ5,CVZ6,CUVXYG,
     &             CUXY1,CVXY1,CMZ1,CMZ2,CMZ3,CMZ4,CMXY1


C
C        XH    - STEP SIZE IN TIME
C        XK    - STEP SIZE IN Z
C        D     - DIFFUSSION COEFFICIENT OF EXTRABEAD
C        DD    - DIFFUSSION COEFFICIENT OF INTRABEAD
C        TU1    - SPIN LATICE RELAXATION TIME OF BLOOD
C        TV1    - SPIN LATICE RELAXATION TIME OF TISSUE
C        TU2    - SPIN-SPIN RELAXATION TIME OF BLOOD
C        TV2    - SPIN-SPIN RELAXATION TIME OF TISSUE
C        TM1    - SPIN LATICE RELAXATION TIME OF BOUND WATER
C        TM2    - SPIN-SPIN RELAXATION TIME OF BOUND WATER
C        TR     - REPITITION TIME
C        TE     - ECHO TIME
C        XK1    - RATE COEFFICIENT - EXTRABEAD TO INTRABEAD
C        XK2    - RATE COEFFICIENT - INTRABEAD TO EXTRABEAD
C        XKM    - RATE COEFFICIENT - IN AND OUT BOUND WATER
C        BETA   - VOLUME RATIO OF INTRABEAD TO EXTRABEAD
C        BETA1  - VOLUME RATIO OF INTRABEAD TO BOUND WATER
C        W      - FLOW VELOCITY OF EXTRABEAD
C        WT     - FLOW VELOCITY OF INTRABEAD
C        U00    - EQUILIBRIUM MAGNETIZATION IN EXTRABEAD COMPARTMENT
C        V00    - EQUILIBRIUM MAGNETIZATION IN INTRABEAD COMPARTMENT
C        UM0    - EQUILIBRIUM MAGNETIZATION IN BOUND WATER COMPARTMENT


        GAMMA=2.68E4
        NFLOW=7
C       **********DIFFUSSION COEFFICIENTS**********

         D=1.0E-4
C         IN CM^2/SEC
         DD=2.5E-5
C         IN CM^2/SEC

C       ******PHYSICAL VOLUME RATIO******

         PHYSICAL_BETA= 2.5

         VEXTRA= 0.9/( PHYSICAL_BETA + 1 )

C       **********VOLUME RATIO***********
```

```
      BETA1= 6.1111
C       BETA*VEXTRA/( 0.9-VEXTRA*(1+BETA) )

      BETA= PHYSICAL_BETA*BETA1/(1.+BETA1)

C     ******EQUILIBRIUM MAGNETIZATION******

      U00=VEXTRA*1000.
      V00=BETA*VEXTRA*1000.
      UM0=V00/BETA1

C     ******RATE COEFFICIENTS***********

      XK1= 1.0
C       IN SEC**(-1)

      XK2= XK1*U00/V00
C       IN SEC**(-1)

      XK3= 0.8
C       IN SEC**(-1)

      XK4= XK3*U00/UM0
C       IN SEC**(-1)

      XK5= 0.8
C       IN SEC**(-1)

      XK6= XK5*V00/UM0
C       IN SEC**(-1)

C     ******SPIN LATICE RELAXATION*****

      T1TOTAL= 0.604
      TU1= 2.0
C       IN SEC
      TVM1= PHYSICAL_BETA*VEXTRA/(0.9/T1TOTAL-VEXTRA/TU1)
C       IN SEC
      TV1= 2.0
C       IN SEC
      TM1= 1./(1.+BETA1)/(1.0/TVM1-( BETA1/(1.+BETA1) )/TV1)
C       IN SEC
      T2TOTAL= 0.057
      TU2= 2.0
C       IN SEC
      TVM2= PHYSICAL_BETA*VEXTRA/(0.9/T2TOTAL-VEXTRA/TU2)
C       IN SEC
      TV2= 2.0
C       IN SEC
      TM2= 1./(1.+BETA1)/(1.0/TVM2-( BETA1/(1.+BETA1) )/TV2)
C       IN SEC

C     ***********TIME OF REPITITION*********

      TR=0.4
C       IN SEC

C     ***********TIME OF ECHO***********

      TE = 15.0E-3
       IN SEC

C     ***** MAGNITUDE OF GRADIENT *****
```

```
      GZ1= 0.0
      GZ2= 0.0

C     **************FLOW RATES*************

      DO 7000 MM=1,NFLOW
      W= 0.0 + 0.01*(MM - 1)
C       IN CM/SEC

C     ******STEP SIZE******************

      XH=1.0E-05
C       IN SEC
      XK=SQRT(6.*XH)/8.
C       IN CM

C     ***** TOTAL NO. OF PULSE ********

      NTOTAL=4

C     *******POSITIONS OF SLICE BOUNDARIES********

      Z1=-0.15
C       IN CM
      Z2=0.15
C       IN CM

C     **********TOTAL LENGTH OF REGION************

      XL=0.35
C       IN CM

C     ******************************************

      N=2.*XL/XK
      N1=N+1

      M1=(TR-T1ST)/XH
      MTE=TE/XH

      ILEFT=(XL+Z1)/XK
      IRIGHT=(XL+Z2)/XK
      BRATIO=BETA/BETA1
      GNOR=1+BETA+BRATIO
      GNOR2=1+BETA
      UVM0=1/GNOR*(U00+BETA*V00+BRATIO*UM0)
      SIGNAL0=UVM0*(Z2-Z1)

      DO 15 J=1,N
C       UVX(J,2)=0.0
C       UVX(J,4)=0.0
        UVY(J,2)=0.0
        UVY(J,4)=0.0
        UVZ(J,2)=U00
        UVZ(J,4)=V00
C       UMX(J,2)=0.0
        UMY(J,2)=0.0
        UMZ(J,2)=UM0
15    CONTINUE


      CUZ1=(1./XH-2.*D/XK**2-(XK1+XK3)*BETA-1./TU1)*XH
      CUZ2=(D/XK**2-W/2./XK)*XH
      CUZ3=(D/XK**2+W/2./XK)*XH
      CUZ3U00=CUZ3*U00
```

```
      CUZ4=XK2*BETA*XH
      CUZ5=XH/TU1*U00
      CUZ6=XK4*BETA*XH
      CUXY1=(1./XH-2.*D/XK**2-(XK1+XK3)*BETA-1./TU2)*XH

      CVZ1=(1./XH-2.*DD/XK**2-(XK2+XK5)-1./TV1)*XH
      CVZ2=(DD/XK**2)*XH
      CVZ3=(DD/XK**2)*XH
      CVZ3V00=CVZ3*V00
      CVZ4=XK1*XH
      CVZ5=XH/TV1*V00
      CVZ6=XK6*XH
      CVXY1=(1./XH-2.*DD/XK**2-(XK2+XK5)-1./TV2)*XH

      CMZ1=(1./XH-(XK4+XK6)*BETA1-1./TM1)*XH
      CMZ2=XK3*BETA1*XH
      CMZ3=XK5*BETA1*XH
      CMZ4=XH/TM1*UM0
      CMXY1=(1./XH-(XK3+XK4)*BETA1-1./TM2)*XH

C     ***********SIMULATION STARTS BELOW************


      NSEQ=1

5000  IF(NSEQ.EQ.NTOTAL+1) GO TO 7000

      GZ=GZ1
      CUVXYG=XH*GAMMA*GZ*XK
      CALL SOLUTION(M1,MTE)

      IF(NSEQ.NE.NTOTAL) GO TO 5500

      SUMU1=0.0
      SUMV1=0.0
      SUMM1=0.0

      DO 35 J=ILEFT,IRIGHT
        SUMU1=SUMU1+ UVY(J,2)*XK
        SUMV1=SUMV1+ UVY(J,4)*XK
        SUMM1=SUMM1+ UMY(J,2)*XK
35    CONTINUE

      SIGNAL(MM)=1./GNOR*(SUMU1+BETA*SUMV1+BRATIO*SUMM1)

5500  NSEQ=NSEQ+1
      GO TO 5000

7000      CONTINUE

      OPEN(4,FILE='G25pb25k1.dat',STATUS='NEW')

      DO 60 I=1,NFLOW
        VFLOW = 0.0 + ( I - 1 ) * 0.1
        WRITE(4,120) VFLOW, DLOG( ABS( SIGNAL(I)/SIGNAL(1) ) )
60    CONTINUE

      WRITE(4,130)


120   FORMAT(F12.8,5x,F12.8)
130   FORMAT( '& V          LN( SV(G-25)/S0(G-25) ) ' )

      CLOSE(4)
```

```
      END

C     ******************************************
C
C          SUBROUTINE   SOLUTION
C
C     ******************************************
      SUBROUTINE SOLUTION(M,MTE)
      COMMON /COEFFICIENT/ UVX,UVY,UVZ,UMX,UMY,UMZ,
     &             SIGNAL,CUZ1,CUZ2,CUZ3,CUZ4,CUZ5,CUZ6,
     &             CVZ1,CVZ2,CVZ3,CVZ4,CVZ5,CVZ6,
     &             CUVXYG,CUXY1,CVXY1,CMZ1,CMZ2,CMZ3,CMZ4,
     &             CMXY1,N,N1,ILEFT,IRIGHT,XL,Z1,Z2,XH,XK,
     &             BETA,BETA1,MM,NSEQ,NTOTAL,BRATIO,GNOR,
     &             U00,V00,UM0

      DOUBLE PRECISION UVX(5000,7),UVY(5000,7),UVZ(5000,7),
     &             UMX(5000,7),UMY(5000,7),UMZ(5000,7),
     &             SIGNAL(100),CUZ1,CUZ2,CUZ3,CUZ4,CUZ5,CUZ6,
     &             CVZ1,CVZ2,CVZ3,CVZ4,CVZ5,CVZ6,CUVXYG,
     &             CUXY1,CVXY1,CMZ1,CMZ2,CMZ3,CMZ4,CMXY1


      IZ1=(XL+Z1)/XK
      IZ2=(XL+Z2)/XK

C      IFRONT1=(XL+3*Z1)/XK
C      IFRONT2=(XL+2*Z1)/XK

C     ***90 DEGREE PULSE FROM Z1 TO Z2 UNTIL LINE #25***

      DO 25 J=IZ1,IZ2
        UVY(J,2)=UVZ(J,2)
        UVY(J,4)=UVZ(J,4)
        UMY(J,2)=UMZ(J,2)

C     ********ANY DEGREE PULSE************
C        UVZ(J,2)= cosd(FLIP_ANGLE)*U00
C     ************************************
        UVZ(J,2)=0.
        UVZ(J,4)=0.
        UMZ(J,2)=0.
25    CONTINUE


      DO 10 I=1,M
C        UVX(1,2)=UVX(2,2)
C        UVX(1,4)=UVX(2,4)
C        UVX(N+1,2)=UVX(N,2)
C        UVX(N+1,4)=UVX(N,4)

        UVY(1,2)=UVY(2,2)
        UVY(1,4)=UVY(2,4)
        UVY(N+1,2)=UVY(N,2)
        UVY(N+1,4)=UVY(N,4)

        UVZ(1,2)=UVZ(2,2)
        UVZ(1,4)=UVZ(2,4)
        UVZ(N+1,2)=UVZ(N,2)
        UVZ(N+1,4)=UVZ(N,4)

C         UMX(1,2)=UMX(2,2)
C         UMX(N+1,2)=UMX(N,2)
        UMY(1,2)=UMY(2,2)
        UMY(N+1,2)=UMY(N,2)
```

```
            UMZ(1,2)=UMZ(2,2)
            UMZ(N+1,2)=UMZ(N,2)

            DO 14 J=1,N1
C              UVX(J,1)=UVX(J,2)
C              UVX(J,3)=UVX(J,4)
              UVY(J,1)=UVY(J,2)
              UVY(J,3)=UVY(J,4)
              UVZ(J,1)=UVZ(J,2)
              UVZ(J,3)=UVZ(J,4)

C              UMX(J,1)=UMX(J,2)
              UMY(J,1)=UMY(J,2)
              UMZ(J,1)=UMZ(J,2)
14          CONTINUE


            DO 30 J=2,N
C           UVX(J,2)=CUXY1*UVX(J,1)+CUZ2*UVX(J+1,1)+CUZ3*UVX(J-1,1)
C     &              +CUZ4*UVX(J,3)+CUVXYG*(J-N/2)*UVY(J,1)
C     &              +CUZ6*UMX(J,1)

C           UVX(J,4)=CVXY1*UVX(J,3)+CVZ2*UVX(J+1,3)+CVZ3*UVX(J-1,3)
C     &              +CVZ4*UVX(J,1)+CUVXYG*(J-N/2)*UVY(J,3)
C     &              +CVZ6*UMX(J,1)

          UVY(J,2)=CUXY1*UVY(J,1)+CUZ2*UVY(J+1,1)+CUZ3*UVY(J-1,1)
     &             +CUZ4*UVY(J,3)-CUVXYG*(J-N/2)*UVX(J,1)
     &             +CUZ6*UMY(J,1)

          UVY(J,4)=CVXY1*UVY(J,3)+CVZ2*UVY(J+1,3)+CVZ3*UVY(J-1,3)
     &             +CVZ4*UVY(J,1)-CUVXYG*(J-N/2)*UVX(J,3)
     &             +CVZ6*UMY(J,1)

          UVZ(J,2)=CUZ1*UVZ(J,1)+CUZ2*UVZ(J+1,1)+CUZ3*UVZ(J-1,1)
     &             +CUZ4*UVZ(J,3)+CUZ5+CUZ6*UMZ(J,1)

          UVZ(J,4)=CVZ1*UVZ(J,3)+CVZ2*UVZ(J+1,3)+CVZ3*UVZ(J-1,3)
     &             +CVZ4*UVZ(J,1)+CVZ5+CVZ6*UMZ(J,1)

C           UMX(J,2)=CMXY1*UMX(J,1)+CMZ2*UVX(J,1)+CMZ3*UVX(J,3)
C     &              +CUVXYG*(J-N/2)*UMY(J,1)

          UMY(J,2)=CMXY1*UMY(J,1)+CMZ2*UVY(J,1)+CMZ3*UVY(J,3)
     &             -CUVXYG*(J-N/2)*UMX(J,1)

          UMZ(J,2)=CMZ1*UMZ(J,1)+CMZ2*UVZ(J,1)+CMZ3*UVZ(J,3)
     &             +CMZ4
30          CONTINUE



          IF(NSEQ.EQ.NTOTAL.AND.I.EQ.MTE) THEN
            GO TO 100
          ENDIF

10        CONTINUE

100       CONTINUE


          RETURN
          END
```

REFERENCES

1. Schwemmle, K.; Aigner, K. Vascular Perfusion in Cancer Therapy, Springer-Verlag Berlin Heidelberg New york Tokyo, 1983.

2. Davies, D.G.; Barnes, C.D. Regulation of Ventilation and Gas Exchange, Academic Press, 1978.

3. Shapiro, B.A.; Kacmaree, R.M.; Cane, R.D.; Peruzzi, W.T.; Hauptman, D. Clinical Application of Respiratory Care, 4th ed. Mosby Year Book, 1991.

4. Bayon, A.; Drucker-Colin, R. *In Vivo* Perfusion and Release of Neuroactive Substances, Academic Press, 1985.

5. Ritchie, H.D.; Hardcastle, J.D. Isolated Organ Perfusion, University Park Press, 1973.

6. Lassen, N.A.; Perl W. Tracer Kinetic Methods in Medical Physiology, Raven Press, 1979.

7. Baron, J.C.; Frackowiak, R.S.J.; Herholz, K.; Jones, T.; Lammertsma, A.A.; Wienhard, K. Use of PET methods for measurement of cerebral energy metabolism and hemodynamics in cerebrovascular disease. *J. Cereb. Blood Flow Metab.* 9:723-742; 1989.

8. Yonas, H.; Good, W.F.; Gur, D.; Wolfson, Jr., S.K.; Latchaw, R.E.; Good, B.C.; Leanza, R.; Miller, S.L. Mapping cerebral blood flow by xenon-enhanced computed tomography: clinical experience. *Radiology* 152:435-442; 1984.

9. Detre, J.A.; Eskey, C.J.; Koretsky, A.P. Measurement of cerebral blood flow in rat brain by ^{19}F-NMR detection of trifluoromethane washout. *Magn. Reson. Med.* 15:45-47; 1990.

10. Belliveau, J.W.; Rosen, B.R.; Kantor, H.L.; Rzedzian, R.R.; Kennedy, D.N.; Mckinstry, R.C.; Vevea, J.M.; Cohen, M.S.; Pykett, I.L.; Brady, T.J. Perfusion imaging with NMR contrast agents. *Magn. Reson. Med.* 14(2):538; 1990.

11. Jones, S.C.; Greenberg, J.H.; Reivich, M. Error analysis for the determination of cerebral blood flow with the continuous inhalation of ^{15}O-labeled carbon dioxide and positron emission tomography. *J. Comp. Assist. Tomogr.* 6:116; 1982.

12. Lammertsma, A.A.; Jones, T. Correction for the presence of intravascular oxygen-15 in the steady-state technique for measuring regional oxygen extraction ratio in the brain: 1. Description of the method. *J. Cereb. Blood Flow Metab.* 3(4):416-424; 1983.

13. Von Schulthess, G.K.; Fisher, M.R.; Higgins, C.B. Pathologic blood flow in pulmonary disease as shownn by gated magnetic resonance imaging. *Ann. Intern. Med.* 103(3):317-323; 1985.

14. Taylor, D.G.; Bushell, M.C. *Society of Magnetic Resonance in Medicine*, Annual Meeting Absract Book, 1985; p. 612.

15. Budinger, T.F.; Knittel, B.L.; Brunner, P.; Harrison, C. *Society of Magnetic Resonance in Medicine*, Annual Meeting Absract Book, 1985; p. 577.

16. Le Bihan, D.; Breton, E.; Lallemand, D.; Grenier, P.; Cabanis, E.; Laval-Jeantet, M. MR imaging of intravoxel incoherent motions: Application to diffusion and perfusion in neurologic disorders. *Radiology* 161:401-407; 1986.

17. Parker, D.L.; Yuan, C.; Blatter, D.D. MR angiography by multiple thin slab #D acquisition. *Magn. Reson. Med.* 17434-451; 1991.

18. Carr, H.Y.; Purcell, E.M. Effects of diffusion on free precession in nuclear magnetic resonance experiments. *Phys. Rev.* 94:630-638; 1954.

19. Stejskal, E.O.; Tanner, J.E. Spin diffusion measurements: spin echoes in the presence of a time-dependent field gradient. *J. Chem. Phys.* 42:288-292; 1965.

20. Weiss, H.R.; Buchweitz, E.; Murtha, T.J.; Auletta, M. Quantitative regional determination of morphometric indices of the total and perfused capillary network in the rat brain. *Circ. Res.* 51:494-503; 1982.

21. Pavlik, G.; Rackl, A.; Bing R.J. Quantitative capillary topography and blood flow in the cerebral cortex of cats: an in-vivo microscopic study. *Brain Res.* 208:35-58; 1981.

22. Taylor, D.G.; Bushell, M.C. The spatial mapping of translational diffusion coefficients by the NMR imaging technique. *Phys. Med. Biol.* 30:345-349; 1985.

23. Harpen, M.D. Indicator dilution approach to NMR signal-flow curves. *Phys. Med. Biol.* 30:687-693; 1985.

24. Harpen, M.D.; Allison, R.C. Nuclear magnetic resonance of perfused tissue. *Phys. Med. Biol.* 31:417-423; 1986.

25. Ahn, C.B.; Lee, S.Y.; Nalcioglu, O.; Cho, Z.H. An improved nuclear magnetic resonance diffusion coefficient imaging method using an optimized pulse sequence. *Med. Phys.* 13:789-793; 1986.

26. Patz, S.; Hawkes, R.C. The application of steady-state free precession to the study of very slow fluid flow. *Magn. Reson. in Med.* 3:140-145; 1986.

27. Ahn, C.B.; Lee, S.Y.; Nalcioglu, O.; Cho, Z.H. The effects of random directional distributed flow in nuclear magnetic resonance imaging. *Med. Phys.* 14:43-48; 1987.

28. Harpen, M.D. Comments on The effects of random directional distributed flow in nuclear magnetic resonance imaging. *Med. Phys.* 14:1092-1093; 1987.

29. Gullberg, G.T.; Ghosh Roy, D.N. An MRI perfusion model incorporating nonequilibrium kinetics. *Society of Magnetic Resonance in Medicine, Vol. 2*, San Francisco, August, 1988; p. 887.

30. Le Bihan, D.; Breton, E.; Lallemand, D.; Aubin, M.; Vignaud, J; Laval-Jeantet, M. Separation of diffusion and perfusion in intravoxel incoherent motion MR imaging. *Radiology* 168:497-505; 1988.

31. Le Bihan, D. Intravoxel incoherent motion imaging using steady-state free precession. *Mag. Reson. in Med.* 7:346-351; 1988.

32. Le Bihan, D.; Turner, R.; Macfall, J.R. Effects of intravoxel incoherent motions (IVIM) in steady-state free precession (SSFP) imaging: Application to molecular diffusion imaging. *Mag. Reson. in Med.* 10:324-337; 1989.

33. Feinberg, D.T.; Jakab, P.D. Perfusion imaging by 3D FT echo planar utilizing separate pulse sequences for low velocity and diffusion encoding. *Society of Magnetic Resonance in Medicine*, Amsterdam: 140; 1989.

34. Axel, L. Blood flow effects in magnetic resonance imaging. *Am. J. Roentgenology* 143:1157-1166; 1984.

35. Gullberg, G.T.; Wehrli, F.W.; Shimakawa, A.; Simons, M.A. MR vascular imaging with a fast gradient refocusing pulse sequence and reformatted images from transaxial sections. *Radiology* 165:241-246; 1987.

36. Gullberg, G.T.; Simons, M.A.; Wehrli, F.W. A mathematical model for signal from spins flowing during the application of spin echo pulse sequences. *Magn. Reson. Imaging* 6:437-461; 1988.

37. Hahn, E.L. Spin Echoes. *Phys Rev.* 80:580-594; 1950.

38. Torrey, H.C. Bloch equations with diffusion terms. *Phys. Rev.* 104:563-565; 1956.

39. Stejskal, E.O. Use of spin echoes in a pulsed magnetic-field gradient to study anisotropic, restricted diffusion and flow. *J. Chem. Phys.* 43:3597-3603; 1965.

40. Tanner, J.E.; Stejskal, E.O. Restricted self-diffusion of protons in colloidal systems by the pulsed-gradient, spin-echo method. *J. Chem. Phys.* 49:1768-1777; 1968.

41. Packer, K.J. The study of slow coherent molecular motion by pulsed nuclear magnetic resonance. *Mol. Phys.* 17:355-366; 1969.

42. Cooper, R.L.; Chang, D.B.; Young, A.C.; Martin, C.J.; Johnson, B. Restricted diffusion in biophysical systems. *Biophys. J.* 14:161-177; 1974.

43. Carr, H.Y. Steady-state free precession in nuclear magnetic resonance. *Phys. Rev.* 112:1693-1701; 1958.

44. Bassingthwaighte, J.B. A concurrent flow model for extraction during transcapillary passage. *Cir. Res.* 35:483-503; 1974.

45. Rose, C.P.; Goresky, C.A.; Bach, G.G. The capillary and sarcolemmal barriers in the heart. *Cir. Res.* 41:515-533; 1977.

46. Phelps, M.E.; Mazziotta, J.C.; Schelbert, H.R. Positron Emission Tomography and Autoradiography: Principles and Applications for the Brain and Heart. New York: Raven Press; 1986.

47. Budinger, T.F.; Huesman, R.H.; Knittel, B.; Friedland, R.P.; Derenzo, S.E. Physiological modeling of dynamic measurements of metabolism using positron emission tomography. In: Greitz, T. et. al. (eds); The Metabolism of the Human Brain Studied With Positron Emission Tomography. New York: Raven Press; 1985.

48. Lassen, N.A.; Henriksen, L.; Paulson, O. Regional cerebral blood flow in stroke by ^{133}Xenon inhalation and emission tomography. *Stroke* 12:284-288; 1981.

49. Stokely, E.M.; Sveinsdottir, E.; Lassen, N.A.; Rommer, P. A single photon dynamic computer assisted tomography (DCAT) for imaging brain function in multiple cross sections. *J. Comput. Assist. Tomogr.* 4:230-240; 1980.

50. Belton, P.S.; Ratcliffe, R.G. NMR and compartmentation in biological tissues. *Progress in NMR Spectroscopy* 17:241-279; 1985.

51. McConnell, H.M. Reaction rates by nuclear magnetic resonance. *J. Chem. Phys.* 28:430-431; 1958

52. Woessner, D.E. Nuclear transfer effects in nuclear magnetic resonance pulse experiments. *J. Chem. Phys.* 35:41-48; 1961.

53. Allerhand, A.; Gutowsky, H.S. Spin-echo NMR studies of chemical exchange. I. Some general aspects. *J. Chem. Phys.* 41:2115-2126; 1964.

54. Brownstein, K.R.; Tarr, C.E. Spin-lattice relaxation in a system governed by diffusion. *J. Magn. Reson.* 26:17-24; 1977.

55. Weaver, D.L. Diffusion and the "fast-exchange" model. *J. Magn. Reson.* 37:543-546; 1980.

56. Halle, B. Theory of intramolecular spin relaxation by translational diffusion in locally ordered fluids I. continuum diffusion versus discrete-state exchange in systems with planar interfaces. *Mol. Phys.* 53:1427-1461; 1984.

57. Wennerstrom, H. Nuclear magnetic relaxation induced by chemical exchange. *Mol. Phys.* 24:69-80; 1972.

58. Carver, J.P.; Richards, R.E. A general two-site solution for the chemical exchange produced dependence of T_2 upon the Carr-Purcell pulse separation. *J. Magn. Reson.* 6:89-105; 1972.

59. Allerhand, A.; Gutowsky, H.S. Spin-Echo studies of chemical exchange. II. Closed formulas for two sites. *J. Chem. Phys.* 42:1587-1599; 1965.

60. Lapidus, L.; Pinder, G.F. Numerical Analysis, 3rd ed. Boston, Prindle, Weber, and Schmidt: Chapt. 4; 1985.

61. Report of the Task Group on Reference Man, ICRP Publication 23, Pergamon Press, Oxford, 1975, p. 176.

62. Gullberg, G.T.; Ma, X.; Parker, D.L.; Ghosh Roy, D.N. An MRI perfusion model incorporating nonequilibrium exchange between vascular and extravascular compartments. *Magn. Reson. Imag.* 9:39-52; 1991.

63. Phelps, M.E.; Huang, S.C.; Hoffman, E.J.; Selin, C.J.; Sokoloff, L.; Kuhl, D.E. Tomographic measurement of local cerebral glucose metabolic rate in humans with F-18-2-fluoro-2-deoxyglucose: validation of method. *Ann Neurol* 6:371-388; 1979.

64. Smith, A.M.; Gullberg, G.T.; Christian, P.E.; Datz, F. L. Kinetic modeling of teboroxime using dynamic SPECT imaging of a canine model. *J. Nucl. Med.* 35:484-495; 1994.

65. Wolff, S.D.; Balaban, R.S. Magnetization transfer contrast (MTC) and tissue water proton relaxation *in vivo*. *Magn. Reson. Med.* 10:135-144; 1989.

66. Gore, J.C.; Brown, M.S.; Zhong, J.; Mueller, K.F.; Good, W. NMR relaxation of water in hydrogel polymers: A model for tissue. *Magn. Reson. Med.* 9:325-332; 1989.

67. Howe, F.A.; Griffiths, J.R. A two-compartment phosphate-doped gel phantom for localized spectroscopy. *Magn. Reson. Imag.* 10:119-126; 1992.

68. De Luca, F.; Maraviglia, B.; Mercurio, A. Biological tissue simulation and standard testing material for MRI. *Magn. Reson. Med.* 4:189-192; 1987.

69. Mitchell, M.D.; Kundel, H.L.; Joseph, P.M. Agarose as a tissue equivalent phantom material for NMR imaging. *Magn. Reson. Imag.* 4:263-266; 1986.

70. Howe, F.A. Relaxation times in paramagnetically doped agarose gels as a function of temperature and ion concentration. *Magn. Reson. Imag.* 6:263-270; 1988.

71. Walker, P.; Lerski, R.A.; Mathur De Vré, R.; Binet, J.; Yane, F. Preparation of agarose gels as reference substances for NMR relaxation time measurement. *Magn. Reson. Imag.* 6:215-222; 1988.

72. Fischer, L. Gel Filtration Chromatography, 2nd Edition, Elsevier/North-Holland Biomedical Press, 1980.

73. Determann, H. Gel Chromatography, Berlin, Heideberg, New York, Springer, 1969.

74. Gullberg, G.T.; Simons, M.A.; Welhrli, F.W. A mathematical model for signal from spins flowing during the application of spin echo pulse sequence. *Magn. Reson. Imag.* 6:437-461; 1988.

75. Parker, D.L.; Gullberg, G.T. Signal-to-noise efficiency in magnetic resonance imaging. *Med. Phys.* 17:250-257; 1990.

76. Proceedings of the First International Meeting on Recent Advances in NMR Applications to Porous Media. Bologna, Italy, November 14-16, *Magn. Reson. Imag.* 9; 1991.

77. Schwartz, L.M.; Wilkinson, D.J.; Kostek, S.; Johnson, D.L.; Banavar; J.R. Nuclear magnetism and transport in porous media. *Magn. Reson. Imag.* 9:657-662; 1991.

78. Detre, J.A.; Leigh, J.S.; Williams, D.S.; Koretsky, A.P. Perfusion Imaging. *Magn. Reson. Med.* 23:37-45; 1992.

79. Zhang, W.; Williams, D.S.; Detre, J.A.; Koretsky, A.P. Measurement of brain perfusion by volume-localized NMR spectroscopy using inversion of arterial water spins: Accounting for transit time and cross-relaxation. *Magn. Reson. Med.* 25:362-371; 1992.

80. Ma, X.; Gullberg, G.T.; Parker, D.L. The effect of flow rate of externally tagged endogenous protons on the MRI signal intensity. *Society of Magnetic Resonance in Medicine*, New York, August 14-20, 1993; p. 616.

81. Edzes, H.T.; Samulski, E.T. Cross relaxation and spin diffusion in the proton NMR of hydrated collagen. *Nature (London)* 265:521; 1977.

82. Edzes, H.T.; Samulski, E.T. The measurement of cross-relaxation effects in the proton NMR spin-lattice relaxation of water in biological systems: hydrated collagen and muscle. *J. Magn. Reson.* 31:207-229; 1978.

83. Sobol, W.T.; Cameron, I.G.; Inch, W.R.; Pintar, M.M. Modeling of proton spin relaxation in muscle tissue using nuclear magnetic resonance spin grouping and exchange analysis. *Biophys. J.* 50(1):181-191; 1986.

84. Koenig, S.H.; *in* "Water in Polymers" (S. P. Rowand, Ed.), P. 157, American Chemical Society, Washington, DC, 1980.

85. Koenig, S.H.; *in* "NMR Spectroscopy of Cells and Organism" (R.K. Gupta, Ed.), Vol. 2, p.75, CRC Press, Boca Raton, FL, 1987.

86. Henkelman, R.M.; Huang, X.; Xiang, Q.; Stanisz, G.J.; Swanson, S.D.; Bronskill, M.J. Quantitative interpretation of magnetization transfer. *Magn. Reson. Med.* 29:759-766; 1993.

87. Forsen, S.; Hoffman, R.A. Study of moderately rapid chemical exchange reactions by means of nuclear double resonance. *J. Chem. Phys.* 39:2892-2901; 1963.

88. Zhang, W.; Williams, D.S.; Koretsky, A.P. Measurement of rat brain perfusion by NMR using spin labeling of arterial water: *in vivo* determination of the degree of spin labeling. *Magn. Reson. Med.* 29:416-421; 1993.

89. Kwong, K.K.; Chesler, D.A.; Weisskoff, R.M.; Rosen, B.R. Perfusion MR imaging. *Society of Magnetic Resonance in Medicine*, Annual Meeting Absract Book, 1994; p. 1005.

90. Roberts, D.A.; bergey, P.; Leigh, Jr., J.S. Perfusion imaging using arterial spin-tagging: Measurement of the degree of arterial labeling in humans. *Society of Magnetic Resonance in Medicine*, Annual Meeting Absract Book, 1984; p. 1031.

91. Zhang, W.; Silva, A.C.; Williams, D.S.; Koretsky, A.P. NMR Measurement of perfusion using arterial spin labeling without saturation of macromolecular spins. *Magn. Reson. Med.* 33:370-376; 1995.